Engineering Spatiotemporal Cues for Directed Cartilage Formation

Josephine Y. Wu

Submitted in partial fulfillment of the
requirements for the degree of
Doctor of Philosophy
under the Executive Committee
of the Graduate School of Arts and Sciences

COLUMBIA UNIVERSITY

2022

Abstract

Engineering Spatiotemporal Cues for Directed Cartilage Formation

Josephine Y. Wu

Joint disease is detrimental to basic quality of life. Articular cartilage is responsible for reducing friction and distributing loads in joints as they undergo large, repetitive load cycles each day, but damaged tissue has very limited intrinsic regenerative ability. Osteoarthritis (OA), the most common joint disease, affects over 500 million people worldwide, contributes more than $27 billion dollars in annual healthcare expenditures, and has increased in prevalence by nearly 50% since 1990 with our aging population. In spite of all this, OA remains a chronic degenerative condition lacking in effective treatment strategies. For cartilage repair in late-stage disease, synthetic joint replacements carry risk of altered loading and metal hypersensitivity, while clinically approved autografts or autologous chondrocyte implantation procedures suffer from lack of donor tissue and donor site morbidities. Prior to surgical intervention, OA management is focused on analgesia rather than preventing or slowing early-stage disease. Disease-modifying OA drugs are yet to successfully complete clinical trials, in part due to the widespread use of animal models for therapeutic discovery rather than high-fidelity human models.

Alleviating the burden of cartilage damage will require improvements in both early-stage therapeutic interventions and late-stage repair. Tissue engineering has the potential to offer more biologically faithful cartilage derived with minimal invasiveness, but the resulting cartilage currently lacks the organization or maturity of native tissue. Thus, the central concept of my thesis work was to introduce biologically inspired spatiotemporal cues to

guide engineered cartilage formation, establishing novel methods for cartilage tissue engineering that would provide (i) cartilage-bone grafts for regenerative implantation and (ii) advanced *in vitro* models for studying osteochondral disease. United by the central theme of cartilage, this dissertation spanned three complementary and interacting areas of tissue engineering: regenerative medicine in **Aim 1,** tools and technological development in **Aim 2,** and organs on a chip in **Aim 3.**

In **Aim 1,** we created patient-specific cartilage-bone constructs with native-like features at a clinical scale, using decellularized bone matrix, autologous adipose-derived stem/stromal cells, and dual-chamber perfusion bioreactors to recapitulate the anatomy and zonal organization of the temporomandibular ramus-condyle unit with its fibrocartilage. We validated key tissue engineering strategies for achieving *in vivo* cartilage regeneration, with the cartilage-bone grafts serving as templates for remodeling and regeneration, rather than providing direct replacements for the native tissue. To enable precise *in vitro* manipulation of TGF-β signaling, a key pathway in cartilage development, in **Aim 2** we developed an optogenetic system in human induced pluripotent stem cells and used light-activated TGF-β signaling to direct differentiation into smooth muscle, tenogenic, and chondrogenic lineages. This optogenetic platform served as a versatile tool for selectively activating TGF-β signaling with precise spatiotemporal control. Using optogenetic recapitulation of physiological spatiotemporal gradients of TGF-β signaling in **Aim 3**, we formed stratified human cartilage integrated with subchondral bone substrate, towards *in vitro* engineering of native-like, zonally organized articular cartilage. Collectively, these studies established novel cartilage tissue engineering approaches which can be leveraged to alleviate the burden of joint disease.

Table of Contents

List of Figures

List of Tables

Acknowledgments

To my PhD advisor, Dr. Gordana Vunjak-Novakovic: thank you for your unwavering support, for giving me unparalleled freedom to explore new ideas, and for reminding me that the conventional way is not the only way. I respect you immensely, not only for your scientific accomplishments and wisdom, but also as one of the kindest, humblest, and most humorous individuals I have known. You are the very best mentor I could have hoped for and this has been the opportunity of a lifetime.

Thank you to my thesis committee, mentors, and collaborators – Drs. Clark Hung, Sidney Eisig, Helen Lu, Joanna Smeeton, Barbara Corneo, and David Kaplan, I am especially grateful for your feedback and support throughout my PhD. I owe many thanks to Keith Yeager, Max Summers, Dr. Kelsey Kennedy, and Dr. David Chen, all of whom enabled critical components of this work. I would also like to thank Michael Kissner and the flow cytometry core; the greater Columbia Stem Cell Initiative community; Dr. Theresa Swayne and the confocal microscopy core; Dr. Rajesh Soni and the proteomics core; Dr. Tingting Su and the histology core.

I am fortunate to be surrounded by so many more talented colleagues whom I can also count amongst my closest friends. Naveed Tavakol, it is hard to find words to properly express how much I appreciate you. Whether it was picking up the phone half asleep or picking me up from late nights in lab, supportive feels like an understatement and I am grateful to have had you in my corner as my confidant and sounding board. Drs. Sharon Fleischer, Manny Tamargo, and Pamela Graney, I absorbed so much of your wisdom from simply sharing offices with each of you over the years, but beyond that, thank you for your generosity and candor in advising me on all matters big or small. Andy Lee, thank you for

reminding me to always keep my head up, and for providing some much needed and memorable moments of comedic relief, whether intentional or accidental. Drs. Brittany Marshall and Meghan Pinezich, we have seen each other through so many seasons of life and I could not imagine making it to this point without the two of you by my side since day zero of this journey. Though we may never be as physically close as our earliest days living in Morningside Heights, our friendship will always remain near and dear to my heart.

To my first scientific mentors, who taught me so much more than how to pipette: Dr. Claire Robertson, you were the very first bioengineer I knew and you inspired me to embark on this path. Thank you for taking a chance on me and patiently cultivating my scientific competencies from scratch. Dr. Carsten Alt, thank you for challenging me with opportunities to develop as an independent scientist, and your continued support extending far beyond that first summer internship has been incredible. I continue to look for ways to pay forward the mentorship you both have shown me.

To my support system scattered far and wide from the many places I have lived, I would particularly like to thank Pearl Xu, Jason Liu, Drew Mendinueto, Beverly Fu, Stefano Flavoni, and Dr. Carla Huerta-Lopez: it is so precious and I am grateful that our friendships have stood the tests of space and time. Thank you for showing me that with the right people, you can feel a sense of home anywhere.

To my communities at the Cornerstone Pottery Studio, Greenwich Village Orchestra, and Park Avenue Chamber Symphony: thank you for being my artistic outlets through some of the most challenging years. These weekly respites from my scientific endeavors have been more invaluable than you may know.

To my family, who encouraged curiosity, learning, and education from a young age: thank you giving me a strong foundation on which I could start this PhD.

Finally, I would like to thank my funding sources – the National Science Foundation Graduate Research Fellowship (NSF GRFP), as well as the National Institutes of Health P41 Tissue Engineering Resource Center (NIH TERC) and F31 Ruth L. Kirschstein Individual Predoctoral Fellowship – all of which enabled me to pursue bold ideas with support and safety. Graphical figures were created with BioRender.com.

Chapter 1: Introduction

1.1 Alleviating the Burden of Cartilage Disease

Osteoarthritis (OA) is the most common joint disease affecting over 500 million people worldwide, contributing more than $27 billion in health care expenditures annually. Between 1990 and 2020, OA prevalence increased by nearly 50%, and is only further increasing with our aging population [1]. In spite of all this, OA remains a chronic degenerative condition with poorly understood etiology and pathology [2].

Most joints undergo large, repetitive load cycles each day, and articular cartilage is responsible for reducing friction and distributing loads [3]. Though healthy articular cartilage is highly durable, if damage occurs, there is very limited intrinsic regenerative ability due to its avascular nature [4]. Therefore, damage to cartilage can have a devastating effect on basic quality of life.

Treatment options for cartilage repair as well as early-stage interventions for OA are lacking. Setting aside synthetic joint replacements, which carry risk of altered loading and metal hypersensitivity and cannot grow with the patient, current clinical options such as autografts or autologous chondrocyte implantation suffer from lack of donor tissue and donor site morbidities. The development of bioengineered cartilage-bone grafts could provide biologically and anatomically matched living tissue replacements, derived in a minimally invasive manner. However, it remains challenging to incorporate bone or other surrounding tissues with cartilage into a cohesive graft. Of equal if not greater value are therapeutics which could prevent or slow down the progression of joint disease, but to date,

no disease-modifying OA drug has successfully completed clinical trials [5]. In part, the deficit of effective OA management strategies is due to the lack of high-fidelity models for establishing clinically consistent therapeutics. Essential to tissue homeostasis, disease pathogenesis, and therapeutic response are the stratified organization of cartilage and interactions with the underlying subchondral bone. Animal models, most commonly rodents, may capture some of these features, but there remains a need for high-fidelity models that meet all the above requirements in a human, patient-specific manner. *In vitro* bioengineered cartilage-bone tissue models could be developed to recapitulate physiological interactions with human cells and disease initiating factors, but currently lack the complexity offered by *in vivo* models [6].

Alleviating the burden of cartilage damage will require improvements in both late-stage cartilage repair as well as in early-stage therapeutic interventions. Tissue engineering has to potential to offer more biologically faithful cartilage derived with minimal invasiveness for either indication (regenerative grafts, *in vitro* models), but the resulting cartilage tissues currently lack the organization or maturity of native tissues [6,7].

To address these gaps, we propose to combine two critical advances: precise control of transforming growth factor (TGF)-β signaling and the incorporation of a bone substrate. We anticipate that the incorporation of spatiotemporal cues mimicking development via the cells, scaffold, and environment will enable engineered tissues to achieve native-like stratified cartilage organization with cartilage-bone interactions. In particular, gradients of TGF-β, a widely used factor for driving chondrogenesis and promoting tissue growth, are critical to the development of stratified native-like cartilage [8]. Importantly, engineered

cartilage tissues which fail to recapitulate the appropriate tissue anisotropy become unstable and undergo endochondral ossification once subjected to in vivo implantation [9,10]. Optogenetics can allow for the control of TGF-β signaling by light with high spatiotemporal resolution [11]. In addition, the inclusion of bone substrate has demonstrated utility for enhancing chondrogenesis, suggesting that cartilage-bone crosstalk is important to not only disease pathogenesis but also homeostasis of healthy tissues [12–14]. Thus, we propose to engineer zonally organized human cartilage by applying the appropriate spatiotemporal gradients of TGF-β signaling, while concurrently including a subchondral bone substrate for enhanced osteochondral interactions.

My thesis work was motivated by the need to establish novel methods for cartilage tissue engineering that would provide (i) cartilage-bone grafts for regenerative implantation and (ii) advanced *in vitro* models for studying osteochondral disease. We expect that the precise regulation of TGF-β signaling and the inclusion of a subchondral bone substrate will lead to generation of native-like human articular cartilage. These platforms would ultimately allow for patient-specific treatment of joint disease.

1.2 Central Hypothesis

The precise regulation of TGF-β signaling and the inclusion of a subchondral bone substrate will enable generation of native-like human articular cartilage with zonal organization and cartilage-bone interactions.

1.3 Specific Aims

The central concept of my dissertation was to alleviate the burden of joint disease by leveraging tissue engineering approaches which recapitulate the biology of cartilage development and regeneration. We aim to target joint disease by incorporating complementary facets of tissue engineering, spanning regenerative grafts to *in vitro* models. To this end, we developed the following aims **(Figure 1.1)** in this dissertation:

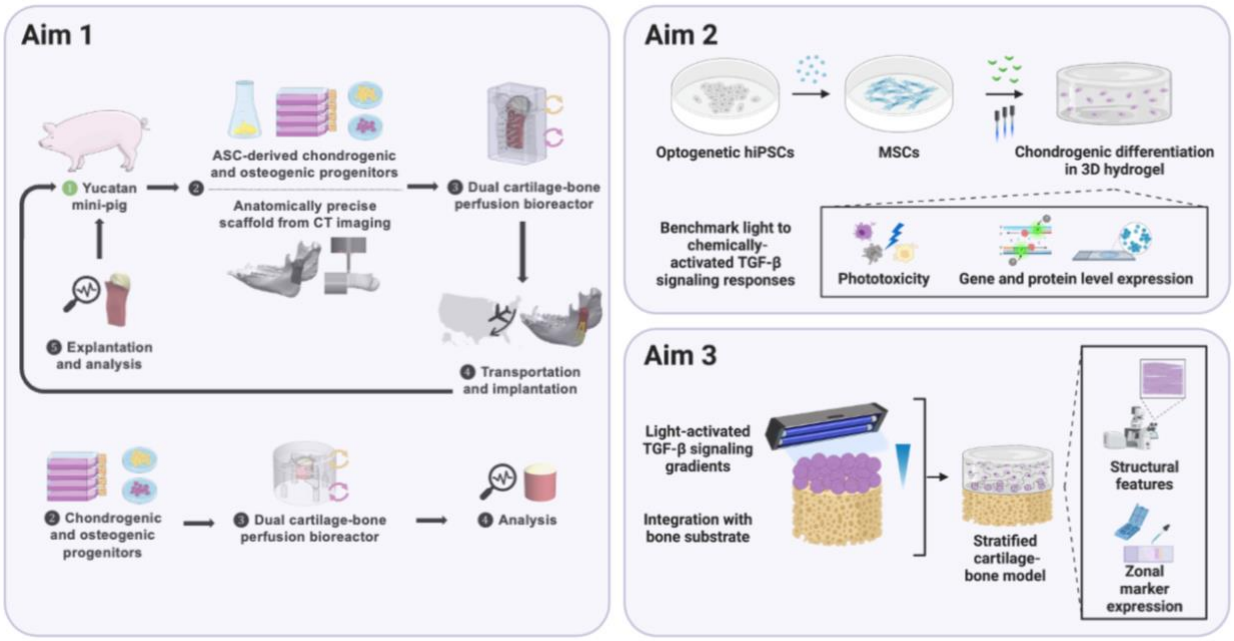

Figure 1.1. Graphical overview of dissertation aims

Aim 1: Validate tissue engineering strategies for achieving *in vivo* cartilage regeneration in a dual-tissue, cartilage-bone temporomandibular joint defect **(Chapter 3).** Aim 1.1: Engineer autologous, living, anatomically correct cartilage-bone craniofacial grafts for implantation in a minipig model. Aim 1.2: Assess the capacity of engineered cartilage-bone grafts to regenerate native-like tissues. Aim 1.3: Investigate the contributions of engineered grafts to tissue regeneration.

Aim 2: Develop an optogenetic human iPSC-based system for TGF-β mediated 3D chondrogenic differentiation **(Chapter 4).** Aim 2.1: Generate human iPSC-derived mesenchymal stem cells with optogenetic control of TGF-β signaling. Aim 2.2: Benchmark light-activated TGF-β signaling responses in 3D chondrogenic differentiation from human iPSCs.

Aim 3: Engineer native-like human articular cartilage by optogenetic control of TGF-β signaling and interfacing with bone substrate **(Chapter 5).** Aim 3.1: Recapitulate physiological spatiotemporal gradients of TGF-β signaling via optogenetic stimulation. Aim 3.2: Integrate bone substrate with cartilage compatible for optogenetic stimulation.

1.4 Publications Resulting from the Dissertation

Wu JY, Yeager K, Soni RK, Tavakol DN, Hung CT, Vunjak-Novakovic G. Directed differentiation of human iPSCs into mesenchymal lineages by optogenetic control of TGF-β signaling. Manuscript in review.

Wu JY, Vunjak-Novakovic G. Bioengineering human cartilage-bone tissues for modeling of osteoarthritis. Stem Cells Dev. 2022 Mar 14. doi: 10.1089/scd.2021.0317.

Wu JY*, Chen D*, Kennedy KM, Yeager K, Bernhard JC, Ng JJ, Zimmerman BK, Robinson S, Durney KM, Shaeffer C, Vila OF, Takawira C, Gimble JM, Guo XE, Ateshian GA, Lopez MJ, Eisig SB, Vunjak-Novakovic G. Tissue engineered autologous cartilage-bone grafts for temporomandibular joint regeneration. Sci Transl Med. 2020 Oct 14;12(565):eabb6683. *Equally contributing authors.

1.5 Conference Proceedings Resulting from the Dissertation

Wu JY, Vunjak-Novakovic G. Directed differentiation of human iPSCs into mesenchymal lineages by optogenetic control of TGF-β signaling. Tissue Engineering and Regenerative Medicine International Society – Americas (TERMIS-AM) Meeting. 2022 Jul; Toronto, ON. Poster.

Wu JY, Vunjak-Novakovic G. Directed differentiation of human iPSCs into mesenchymal lineages by optogenetic control of TGF-β signaling. International Society for Stem Cell Research (ISSCR) Annual Meeting. 2022 Jun; San Francisco, CA. Poster with Abstract Merit Award.

Wu JY, Vunjak-Novakovic G. Directed differentiation of human iPSCs into mesenchymal lineages by optogenetic control of TGF-β signaling. 2nd Optogenetic Technologies & Applications Conference, American Institute of Chemical Engineers (AIChE). 2021 Dec; virtual meeting. Podium with National Science Foundation travel award.

Wu JY, Vunjak-Novakovic G. Optogenetic TGF-β signaling for multilineage mesenchymal differentiation of human iPSCs. Orthopaedic Research Society (ORS) Annual Meeting. 2022 Feb; Tampa, FL. Poster.

Wu JY, Vunjak-Novakovic G. Engineering spatiotemporal cues for directed cartilage formation. Columbia Stem Cell Initiative (CSCI) Work in Progress Seminar Series. 2021 Oct; New York, NY. Seminar.

Wu JY, Vunjak-Novakovic G. Directed differentiation of human iPSCs into mesenchymal lineages by optogenetic control of TGF-β signaling. New York Stem Cell Foundation (NYSCF) Conference. 2021 Oct; virtual meeting. Poster.

Wu JY, Vunjak-Novakovic G. Directed differentiation of human iPSCs into mesenchymal lineages by optogenetic control of TGF-β signaling. 6th Bioengineering & Translational Medicine Conference, American Institute of Chemical Engineers (AIChE). 2021 Oct; virtual meeting. Poster.

Wu JY, Vunjak-Novakovic G. Optogenetic TGF-β signaling for multilineage mesenchymal differentiation of human iPSCs. Biomedical Engineering Society (BMES) Annual Meeting. 2021 Oct; virtual meeting. Poster.

Wu JY, Chen D, Kennedy KM, Yeager K, Bernhard JC, Ng JJ, Zimmerman BK, Robinson S, Durney KM, Shaeffer C, Vila OF, Takawira C, Gimble JM, Guo XE, Ateshian GA, Lopez MJ, Eisig SB, Vunjak-Novakovic G. Tissue engineered autologous cartilage-bone grafts for temporomandibular joint regeneration. Orthopaedic Research Society (ORS) Annual Meeting. 2021 Feb; virtual meeting. Podium.

Wu JY, Chen D, Kennedy KM, Yeager K, Bernhard JC, Ng JJ, Zimmerman BK, Robinson S, Durney KM, Shaeffer C, Vila OF, Takawira C, Gimble JM, Guo XE, Ateshian GA, Lopez MJ, Eisig SB, Vunjak-Novakovic G. Tissue engineered autologous cartilage-bone grafts for temporomandibular joint regeneration. Virtual Seminars in Biomedical Science. 2020 Oct; virtual meeting. Invited talk.

Wu JY, Chen D, Kennedy KM, Yeager K, Vunjak-Novakovic G. Tissue engineered autologous osteochondral grafts for temporomandibular joint regeneration. Biomedical Engineering Society (BMES) Annual Meeting. 2019 Oct; Philadelphia, PA. Podium.

Wu JY, Chen D, Kennedy KM, Yeager K, Vunjak-Novakovic G. Functional tissue-engineered autologous osteochondral grafts for temporomandibular joint (TMJ) reconstruction. Cartilage Biology and Pathology, Gordon Research Conference (GRC). 2019 Mar; Galveston, TX. Poster.

1.6 Funding Sources During PhD Work

National Institutes of Health Ruth L. Kirschstein Individual Predoctoral Fellowship (NIH NRSA F31). "Advanced Tissue Engineered Models of Human Cartilage for Studying Joint Disease." 2021 May – Present. Grant AR078707.

National Science Foundation Graduate Research Fellowship (NSF GRFP). "Tissue Engineered Autologous Cartilage-Bone Grafts for Temporomandibular Joint Regeneration." 2017 Sept – 2020 Sept. Grant 1644869.

Chapter 2: Background

The contents of Chapter 2 are based on the following publications:

Wu JY*, Chen D*, Kennedy KM, Yeager K, Bernhard JC, Ng JJ, Zimmerman BK, Robinson S, Durney KM, Shaeffer C, Vila OF, Takawira C, Gimble JM, Guo XE, Ateshian GA, Lopez MJ, Eisig SB, Vunjak-Novakovic G. Tissue engineered autologous cartilage-bone grafts for temporomandibular joint regeneration. Sci Transl Med. 2020 Oct 14;12(565):eabb6683. *Equally contributing authors.

Wu JY, Vunjak-Novakovic G. Bioengineering human cartilage-bone tissues for modeling of osteoarthritis. Stem Cells Dev. 2022 Mar 14. doi: 10.1089/scd.2021.0317.

2.1 Joint Disease and Cartilage Damage

An estimated 20-25% of the adult population in the United States has been diagnosed with some form of arthritis, and the prevalence of joint disease is expected to increase with an aging population [15,16]. Looking at the temporomandibular joint (TMJ) alone, it is estimated that 10 million people in the United States suffer from TMJ dysfunction [17]. In severe cases, surgical reconstruction is the only option to treat pain and restore function. The need for reconstruction may result from congenital defects such as hemifacial microsomia, damage to the joint due to traumatic injuries or neoplasms, or resorption of the joint due to arthritis, juvenile inflammatory arthritis, or idiopathic condylar resorption [18]. Current surgical interventions suffer from lack of precision and comorbidities, and frequently involve multiple operations. Surgical interventions, such as condylectomy, that are most commonly used for condylar hyperplasia, produce varying results and do not fully restore TMJ function [19–21]. Patients who receive condylectomy tend to experience more TMJ problems and postoperative pain compared to untreated patients [22]. Autologous transplants such as costochondral grafts and fibular flaps, mostly used for large mandibular

defects, are limited by the geometry and volume of donor tissue and donor site morbidity [23,24]. Finally, synthetic options are not without problems. The Teflon-Proplast total joint replacement induced foreign-body giant cell reactions in most patients, with erosions of the glenoid fossa sometimes extending into the middle cranial fossa, and this prosthesis was pulled from the market more than thirty years ago [25,26]. The more recent Zimmer Biomet stock prosthesis and TMJ Concepts patient-matched device have shown early success, but future studies with larger cohorts are needed to assess long-term outcomes, in particular the effects of altered joint loading with alloplastic replacements [27,28]. More recently, metal hypersensitivity and nickel allergy have caused concern among surgeons using these systems, with up to 17% of individuals having metal allergies [29,30]. Metal hypersensitivity to an implanted joint prosthesis can manifest as localized dermatitis, swelling, pain, joint effusions, and prosthesis failure.

The TMJ and knee experience similar incidence of cartilage dysfunction, and clinical practice for both joints follow similar treatment pathways. However, driven by the catastrophic failure of the Teflon-Proplast TMJ prosthesis and subsequent reclassification of all TMJ devices into the highest risk group by the United States Food and Drug Administration (FDA), there are now considerably more clinical products and solutions available for the knee [31]. Short of total joint replacement for the most extreme cases, there are several other approved reconstructive strategies for focal lesions, each with limitations [32]. The gold standard procedure, microfracture, involves drilling through the subchondral bone to allow progenitor cells from the marrow to migrate into the defect. However, microfracture often results in fibrocartilage and osteophyte formation, which disrupts joint

biomechanics and typically leads to failure within 5 years [33–35]. Other options are autologous chondrocyte implantation (ACI) or matrix-induced ACI (MACI), in which an arthroscopic biopsy is harvested from a low weight bearing joint region, cells are expanded *in vitro*, and the resulting chondrocyte population is implanted under a protective membrane [7]. For both ACI and MACI, multiple operations are needed and immature tissues are implanted, leading to prolonged recovery time and high risk of failure. Osteochondral autografts (OATS) are similarly harvested from a low weight bearing region of the patient's joint, then directly plugged into the defect site. Though OATS requires only one surgery and introduces hyaline cartilage, its widespread success is limited by availability of appropriate donor tissue and donor site morbidities [36].

Overall, there is an unmet need for precise functional reconstruction of cartilage and bone tissues. Engineered tissue constructs offer bioinspired and patient-tailored approaches to the reconstruction of the structural and biological components of the graft. Taken together, these considerations make the development of a bioengineered cartilage-bone graft for joint replacement all the more compelling [37].

Non-surgical interventions also fall short of effectively managing early- to mid-stage joint disease. Though osteoarthritis (OA) is the most common joint disease affecting over 500 million people worldwide, it remains a chronic degenerative condition with poorly understood etiology and pathology. OA prevalence increased by nearly 50% between 1990 and 2020, and is further increasing in our aging population [1]. Before surgical intervention, OA management is generally focused on analgesia with paracetamol, non-steroidal anti-inflammatory drugs (NSAIDs), opioids, and intraarticular corticosteroids. Repurposing

disease-modifying anti-rheumatic drugs (DMARDs) from rheumatoid arthritis (RA) showed little success with OA, and none of the disease-modifying OA drugs (DMOADs) have successfully completed clinical trials [5].

The management of cartilage disease continues to be challenging. The deficit of effective OA management strategies is due – at least in part – to the lack of high-fidelity models that would help understand disease progression and test novel treatments [38]. Mouse models are often used to study OA, yet fail to recapitulate key aspects of human cartilage anatomy such as size, thickness, and zonal organization [39]. Although rat models possess thicker cartilage with more zonal structure, naturally occurring OA is uncommon in rats [40]. Animals ultimately cannot fully mimic human biology or serve as patient-specific models of disease, which leads to clinically inconsistent outcomes. These limitations motivate the need for bioengineered human tissue models which can capture the complexity of joint diseases, leading to improvements in the therapeutic discovery process.

Overall, tissue engineering can enable targeting of joint disease from the complementary angles of regenerative medicine and *in vitro* modeling, where each can be leveraged to drive advancements in the other. In this dissertation, we will take engineering approaches inspired by recapitulating the biology of cartilage development and regeneration to alleviate the burden of joint disease.

2.2 Cartilage Function, Structure, and Biology

As most joints undergo large, repetitive load cycles each day, articular cartilage is responsible for reducing friction and distributing said loads [3]. Therefore, damage to cartilage can have a devastating effect on basic quality of life.

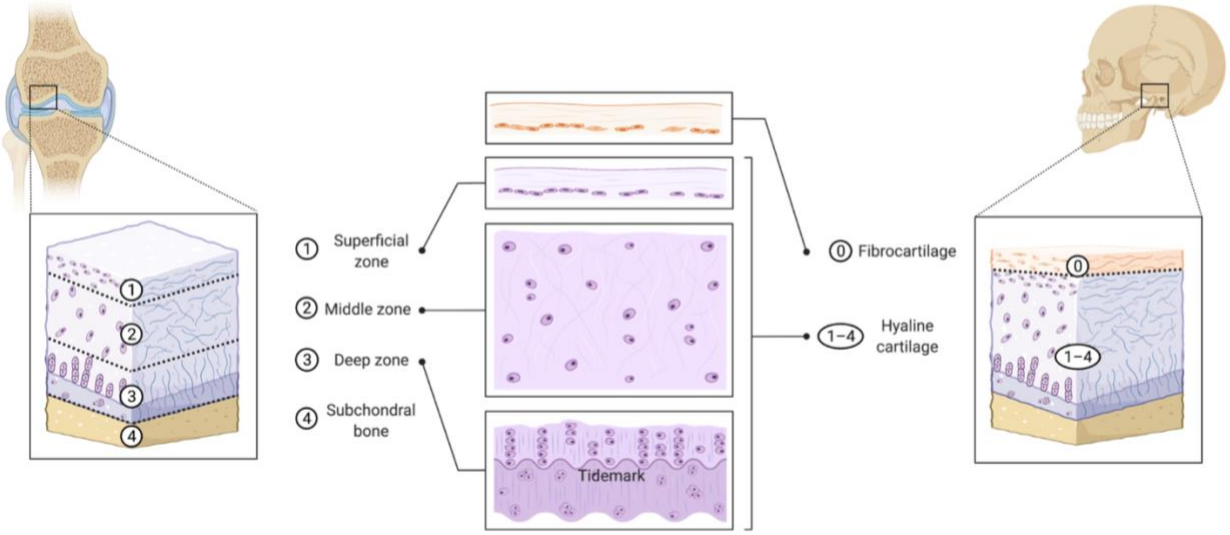

Figure 2.1. Cartilage stratification in the knee and temporomandibular joint

Healthy human articular cartilage has a specific stratification (superficial, middle, and deep zones), with each layer having distinct cell and matrix properties (chondrocyte phenotype, collagen alignment, proteoglycan to water ratio) that are essential to its function **(Figure 2.1).** Frictional and wear properties at the articular surface are enhanced by the compositional heterogeneity of cartilage [41], while the calcified deep zone features small chondrocytes in apatite-filled matrix which limits transport from the underlying bone [3]. While cartilage is devoid of vascularization, innervation, or lymphatics, limited biochemical and biomechanical interactions at the osteochondral junction between cartilage and the subchondral bone are important mediators of joint development, homeostasis, and disease [12,13,42,43]. Uniquely, the cartilage of the TMJ also has a distinct structure compared to the articular cartilage of the knee, with a superficial fibrous layer above hyaline cartilage [44].

In many joint diseases, cartilage degeneration progresses in a layer-dependent manner. OA typically starts with small lesions in the superficial layers and compensatory

matrix production from the deeper layers, until the calcified layers wear away to expose bone. In addition, pathogenesis is mediated by disruptions in tissue crosstalk at the osteochondral junction [45,46]. Healthy articular cartilage is highly durable, but if damage occurs, there is very limited intrinsic regenerative ability due to the lack of blood flow and cell migration [4]. Therefore, we turn to physiological processes of cartilage development and homeostasis for inspiration in our engineering approach.

During embryonic development, cartilage formation begins with a condensation of mesenchymal cells. The developing joint experiences varying levels and durations of signaling based on ligand, antagonist, and receptor expression. Spatiotemporal gradients, thresholds, and balance of transforming growth factor beta (TGF-β) and bone morphogenetic protein (BMP) signaling all work together to dictate cell fate in the joint [47]. From the mesenchymal condensation, chondroprogenitors differentiate, mature into chondrocytes, and eventually undergo hypertrophy and ossification. This full progression, termed endochondral ossification, allows bone to form from a perichondrium template of cartilage precursors. Chondroprogenitors maintain substantial lineage plasticity – in zebrafish, even cells expressing collagen II, a key marker of chondrogenesis, have the ability to repopulate osteoblasts and marrow adipocytes [48]. In developing cartilage, stratification of chondrocytes into proliferative, pre-hypertrophic, and hypertrophic zones allows for control over signaling pathways to prevent further maturation of proliferative chondrocytes of the superficial zone into hypertrophic chondrocytes of the deep zone. Careful regulation over TGF-β, BMP, and other key signaling pathways is necessary to achieve desired tissue

formation. We next consider tissue engineering strategies which have been used to recapitulate these physiological processes and cues towards cartilage regeneration.

2.3 Scientific Premise

It is a well-established paradigm that cells exhibit more native-like behavior when cultured under physical and biochemical conditions mimicking the *in vivo* microenvironment [49]. Chondrocytes in particular are known to dedifferentiate over time in monolayer cultures on stiff substrates and express more collagen I and III, and to "re-differentiate" when suspended in soft 3D hydrogels and recover their chondrogenic phenotype in terms of collagen II and proteoglycan expression [50].

First-generation tissue engineering was able to capture some of these differences by applying the classical paradigm of seeding cells within a 3D scaffolding biomaterial, then stimulating such constructs in an attempt to promote extracellular matrix (ECM) deposition. These bulk fabrication methods produced largely homogenous, isotropic constructs. However, spatiotemporal gradients of TGF-β, a widely used factor for driving chondrogenesis and promoting tissue growth, are critical to the development of stratified native-like cartilage [8]. Importantly, engineered cartilage tissues which fail to recapitulate the appropriate tissue anisotropy become unstable and undergo endochondral ossification once subjected to *in vivo* implantation [9,10]. Similarly, BMP-2 can promote chondrogenic differentiation, osteogenic differentiation, or endochondral ossification in the same system, but require careful regulation [51]. The inclusion of bone substrate has demonstrated utility for promoting chondrogenesis, suggesting that cartilage-bone crosstalk is important to not only disease pathogenesis but also homeostasis of healthy tissues [12–14].

In next-generation tissue engineering, we seek the means for introducing spatiotemporal patterning of cues to more closely mimic developmental processes and ultimately recapitulate the stratified organization of human cartilage with cartilage-bone interactions. There have been numerous efforts to introduce some degree of native-like tissue organization, targeting one or multiple of the fundamental pillars of tissue engineering – cells, scaffold, and environment.

2.4 Cell Sources for Cartilage Tissue Engineering

Early studies of cartilage tissue engineering made use of juvenile bovine chondrocytes due to the dearth of alternative cell sources at the time. However, their developmental state and species of origin limited translational potential, as findings were not necessarily applicable to human cartilage. For example, brief rather than sustained exposure to TGF-β is sufficient for robust cartilage tissue formation from juvenile bovine chondrocytes, but not from human bone marrow-derived mesenchymal stromal/stem cells (MSCs) [8,52–54]. Advances in stem cell biology and the identification of cell populations with chondrogenic potential have since enabled the use of more physiologically relevant cell sources in cartilage tissue engineering.

Common cell sources include primary chondrocytes from biopsy of nasal or articular cartilage [55,56], bone marrow- or adipose-derived MSCs [12,57], or some combination of the populations. Primary chondrocytes remain highly potent *in vitro*, and co-culture with MSCs enhances chondrogenic phenotype and matrix synthesis in both populations [58,59]. The use of either cell source is generally hindered by donor site morbidity, loss of function after extended *in vitro* expansion, and potentially inferior outcomes due to patient age or

disease [60], though nasal chondrocytes and adipose-derived MSCs have been able to overcome some of these limitations [56,61].

In comparison, human induced pluripotent stem cells (hiPSCs) can be an advantageous cell source, as they can be derived from small blood samples to minimize clinical invasiveness while capturing patient specificity. In contrast to primary chondrocytes or MSCs, hiPSCs can be expanded near indefinitely, allowing for sufficient cell numbers, multiple cell types generated from the same source, and genetic modification as needed.

Starting from hiPSCs and other pluripotent stem cells, approaches for differentiation into the relevant musculoskeletal lineages can be classified broadly into single-step, MSC based, and developmentally guided protocols. In choosing an approach for generating chondrocytes from hiPSCs, the fundamental issue is to determine how simple is complex enough – specifically in the context of differentiation, how much development needs to be recapitulated and how much cell heterogeneity can be tolerated in an engineered tissue. Additional related considerations include protocol robustness, reliance on serum or growth factors, throughput, and cost.

Single-step protocols, also called nonspecific differentiations, aim to go directly from pluripotent to differentiated cell types without intermediate lineage specification, starting from monolayers, embryoid bodies, spheroids, or co-culture systems with pluripotent stem cells. While some of these single-step protocols show promise in addition to the ease of use, they result in heterogeneous and inefficiently differentiated cell populations that require downstream sorting and isolation. These methods remain far less adopted than protocols with an intermediate fate specification step.

In musculoskeletal contexts, MSCs from bone marrow or adipose tissue were initially used as the predominant cell source and thus many widely used differentiation protocols rely on MSCs as the starting point. To reconcile with the use of hiPSCs, protocols and commercially validated kits for differentiation into MSC lineages are now available. These MSCs meet the three validation criteria set forth by the International Society for Cellular Therapy: (1) adherence to uncoated tissue culture plastic with elongated cell morphology; (2) high expression of mesenchymal surface markers CD73, CD90, and CD105, and low expression of lineage markers CD19, CD34, CD45, CD79α, and HLA-DR; (3) the ability to tri-differentiate into adipogenic, chondrogenic, and osteogenic lineages [62].

Recent studies have elucidated key differences between bone marrow- and hiPSC-derived MSCs (hiMSCs) using more extensive functional, phenotypic, and genetic characterization. The hiMSCs have gene expression profiles similar to vascular progenitor cells, which can also tri-differentiate along adipogenic, chondrogenic, and osteogenic pathways but under different conditions than bone marrow-MSCs [63]. Designing inductive conditions with hiMSCs in mind, these findings should not preclude the use of hiPSCs as the starting cell source.

Others have taken inspiration from development to design differentiation protocols more closely recapitulating *in vivo* processes. Of note, craniofacial skeletal tissues originate from the neural crest, while the remainder of the skeleton originates from mesoderm, with paraxial and lateral plate mesoderm giving rise to axial and appendicular skeletal tissues, respectively. Developmentally guided methods target multiple pathways in a coordinated and specific manner, resulting in distinct cell types from particular tissue regions [64]. Even

so, recent single cell transcriptomic analysis of chondrogenesis following developmentally guided differentiation from hiPSCs still indicated some off-target differentiation [65].

With the rise of hiPSC-derived chondrogenic progenitors, many groups have started to benchmark these cells against primary or bone marrow-MSC-derived cells [63,66]. Reporters for key chondrogenic markers such as collagen II have been used to assess and purify differentiated cells [67], while advances in single cell sequencing technologies resulted in more thorough evaluation of differentiation strategies [65]. Some groups have also begun to leverage these insights to genetically modify cell lines to modulate expression of favorable or unfavorable factors, for example by constitutively activating BMP-2 for increased chondrogenic capacity [68]. With the rise of CRISPR-Cas9 technologies, cells can be edited with high efficiency to study OA disease pathways. In human chondrocytes, knockout of matrix metallopeptidase (MMP)-13 expression enhanced accumulation of collagen II [69]. In chondrogenic spheroid cultures of murine iPSCs, targeted deletion of the gene encoding interleukin (IL)-1 receptor type I conferred some immunity against IL-1 mediated tissue degradation [70].

Beyond optimizing cell fate specification via temporal coordination of key signaling pathways in isolated cell cultures, we will next consider spatiotemporal regulation of relevant cues and tissue crosstalk in three-dimensional (3D) settings while continuing to draw inspiration from development.

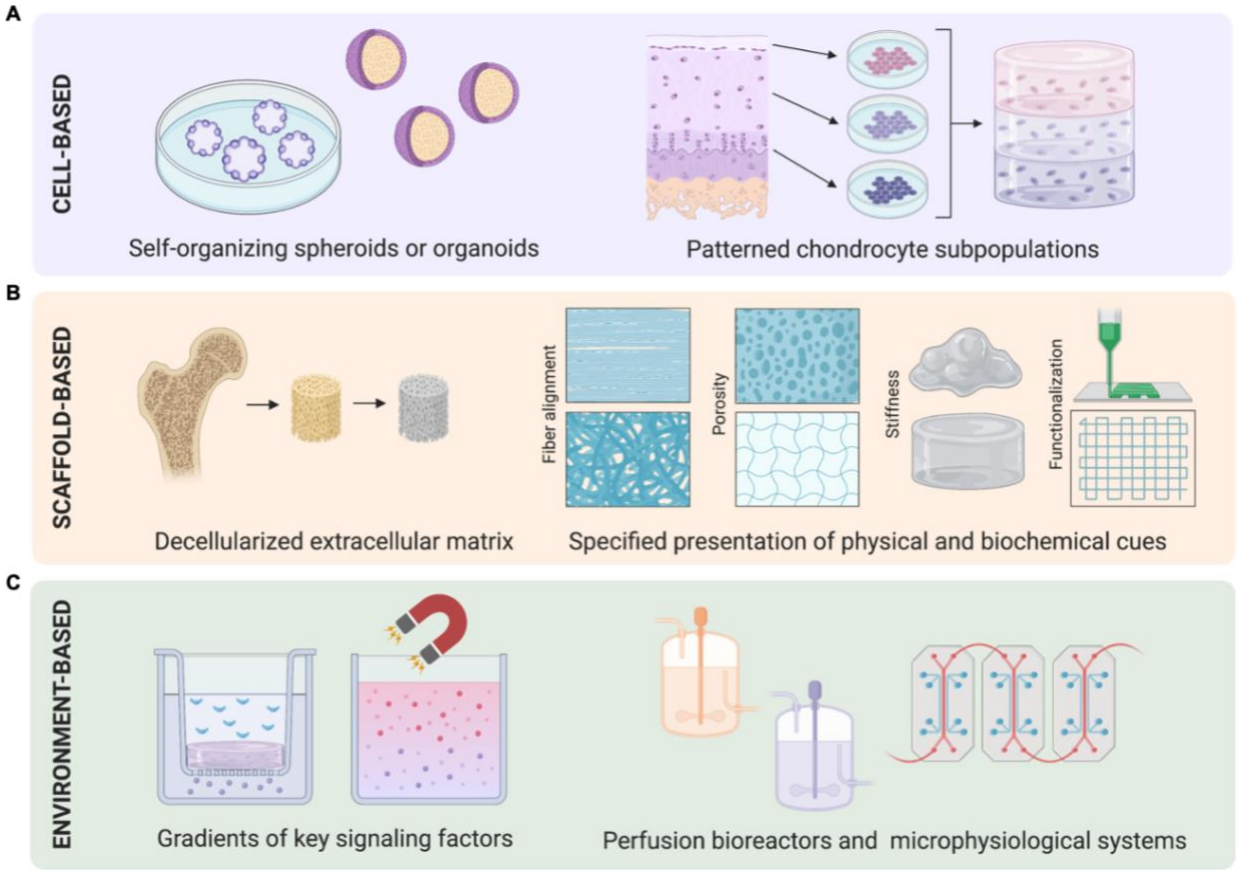

Figure 2.2. Strategies for directed cartilage formation using **(A)** cell-based, **(B)** scaffold-based, or **(C)** environment-based methods.

2.5 Cell-Based Patterning Approaches for Directed Cartilage Formation

Early on, some groups tried to pattern subpopulations of chondrocytes isolated from zonal slices of bovine articular cartilage and re-encapsulated in hydrogels [71,72] **(Figure 2.2A).** Others have since included porous hollow fiber materials for enhanced nutrient transport and MSCs in co-culture as support cells [59]. Even so, cell-based patterning methods in their current state suffer from limited cell numbers and lack of patient specificity.

Some attempts have been made to assemble hiPSC-derived chondrogenic spheroids into zonally organized cartilage, relying on pre-specification of cartilaginous or hypertrophic

spheroid fate over several weeks prior to assembly into regenerative implants [73]. Even following *in vivo* orthotopic implantation, fusion of spheroids into a cohesive tissue was limited. Critically, the boundary proteins of chondrogenic spheroids are known to set after a few days and inhibit fusion with neighboring bodies, greatly limiting the ability of spheroids differentiated in isolation over several weeks to ultimately form larger, cohesive tissue [13]. This approach was low throughput and formed millimeter-scale tissues whereas the proposed clinical applications would necessitate centimeter-scale lesion repair [74]. Moreover, physiological development involves substantial inter-tissue crosstalk, and tissues respond to spatiotemporal gradients of growth factors, motivating the need for an approach which can incorporate these changes in stimuli *in situ.*

Organoids have garnered much success as *in vitro* 3D tissue models with basic self-organization to study aspects of development, function, and disease for the kidney, lung, gut, brain, and retina, on top of a rapidly growing list [75]. Although chondrogenic spheroids have been used for some time, only recently have true osteochondral organoids – recapitulating organ-specific hallmarks in terms of multicellularity, function, and architecture – been formed *in vitro* from murine iPSCs by mirroring endochondral ossification bone development [76]. These organoids offer a scaffold- and bioreactor-free platform for studying crosstalk at the cartilage-bone interface with potential for patient and disease specificity, trading some features of model complexity for ease of use and throughput.

2.6 Scaffold-Based Approaches for Directed Cartilage Formation

Scaffolds are necessary for building more complex engineered tissues and can be used to provide both physical and biochemical cues **(Figure 2.2B).** Multi-layered scaffolds have

been fabricated to mimic depth-dependent heterogeneities in cartilage, for example by tuning the percentage of agarose in each layer to adjust stiffness [77]. Electrospun scaffolds with tri-zonal fiber organization demonstrated more native-like compressive properties than randomly aligned scaffolds [78]. Freeze-dried ECM derived from porcine articular cartilage and growth plate tissues and used in bi-layered cartilage-bone constructs could spatially direct the differentiation of seeded bone marrow-MSCs [79]. Several biofabrication strategies – electrospinning, spherical porogen leaching, directional freezing, and melt electrowriting – have also been combined to create scaffolds with stiffness and microstructure gradients matching native tissue [80]. With advances in 3D bioprinting, non-ECM-derived scaffolds can also be functionalized with biochemical cues to promote chondrogenesis or osteogenesis at precise locations. Cartilage- and bone-promoting peptides presented in different combinations and arrangements within one continuous construct worked synergistically to guide tissue formation in the absence of differentiation factors [81]. Growth factors can also be incorporated in specific scaffold locations with varying release profiles; this has been demonstrated with angiogenic vascular endothelial growth factor (VEGF) and osteogenic BMP-2 gradients to regulate bone healing [82]. Cartilage-bone interactions are also commonly introduced to the model via the scaffold. Our lab has demonstrated the technical feasibility and biological utility of interfacing decellularized bone matrix with engineered cartilage towards forming better stratified tissues [12,13]. Overall, scaffolds present a highly useful opportunity for spatially introducing both physical and biochemical cues, but with a general lack of control over temporal dynamics, especially once cells are added and remodel their surroundings.

2.7 Environment-Based Approaches for Directed Cartilage Formation

Targeting the environment external to the engineered tissue to deliver spatiotemporal cues has garnered more attention recently, with engineering advancements making these approaches technically feasible **(Figure 2.2C).** Work from our lab showed that recapitulation of physiological spatiotemporal TGF-β gradients in an *in vitro* transwell system resulted in enhanced zonal organization of engineered human cartilage with more phenotypic stability, presenting a promising strategy for stratified cartilage tissue engineering [54].

Dual-chamber microfluidic organ-on-a-chip bioreactors have also been used to establish tissue-specific microenvironments with distinct chondrogenic and osteogenic medium streams. Encapsulation of human bone marrow-MSCs or hiMSCs in gelatin with culture over 4 weeks resulted in an osteochondral tissue-on-a-chip with the formation of a nascently functional osteochondral junction [14,83]. Using the osteochondral tissue-on-a-chip models, the OA state in a human bone marrow-MSC based model was induced via a 7-day IL-1β challenge to the cartilage component alone or the bone component alone, and analyzed for tissue-specific markers and MMP expression [83]. Interestingly, IL-1β treatment of the bone component created a catabolic response in the cartilage component, stronger than after direct treatment of the cartilage component, demonstrating effective cartilage-bone crosstalk in the model and suggesting a more active role of osteoblasts in OA degeneration. In the follow-up study using the hiMSC based model, the authors recapitulated these findings and additionally tested drug responses [14]. Celecoxib, a commonly prescribed NSAID for OA, showed no adverse effect on healthy tissues and downregulated

catabolic and proinflammatory cytokines in pathologic tissues. OA tissues which only had a drug-treated cartilage component still showed some rescued phenotype in the bone component. Overall, these studies offer a strong case for the utility of engineered cartilage-bone tissues for elucidating some mechanisms behind OA progression and for screening candidate therapeutics.

Others have demonstrated methods to establish the osteochondral interface via BMP-2 gradients, creating distinct cartilage and bone regions with an interface resembling the native tidemark using buoyancy-driven gradients [84] or magnetic field alignment of BMP-2 conjugated superparamagnetic nanoparticles [85]. Magnetic alteration of a hydrogel scaffold, in lieu of tagging growth factors or cells of interest, can also be used to the same effect [86]. In the context of bone regeneration and using optogenetically modified LIM Homeobox 8 (LHX8) and BMP-2 genes, light-activated expression could selectively drive the proliferative or osteogenic differentiation potential of rat BM-MSCs [87]. The use of external force fields for patterning in tissue engineering has been extensively described [88]. These newer strategies trend towards overcoming the limitations of traditional environmental patterning methods which rely on maintenance of a chemical gradient and have an inherent lack of fast and specific spatiotemporal control, making them difficult to translate to complex settings such as multi-tissue platforms or loading bioreactors.

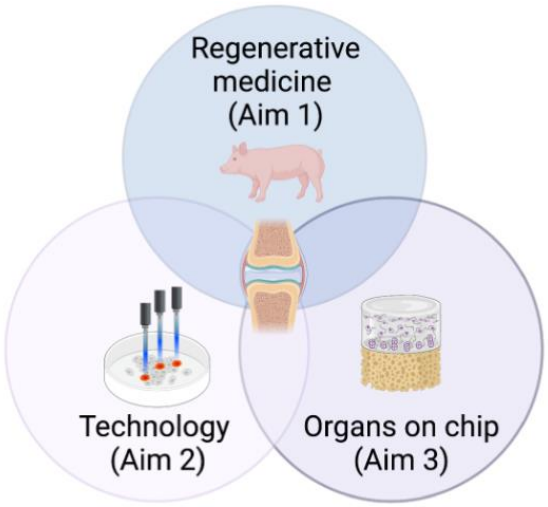

Figure 2.3. Overall scope of the dissertation

2.8 Overall Approach

Alleviating the burden of cartilage damage will require improvements in joint replacements as well as early-stage disease management strategies **(Figure 2.3).** Engineered tissue grafts can offer biologically and anatomically matched living tissue replacements; however, current strategies use cells insufficiently primed for cartilage regeneration, or fail to incorporate bone or other means of facilitating integration with native tissues [7]. Engineered *in vitro* models can be more biologically faithful as they can incorporate human cells; however, such models generally lack the complexity offered by *in vivo* systems, including the effects of tissue architecture and interactions with other tissues [6]. Despite decades of research on engineering cartilage, existing strategies are unable to produce structurally complex tissues with biomimetic collagen architectures, mechanical properties, and physiological function, dramatically limiting their utility. Radical new approaches are required if the tissue engineering field is to successfully address this

problem. To address these gaps, we sought to establish a novel approach for cartilage tissue engineering by combining two critical advances: precise control of TGF-β signaling and the incorporation of cartilage-bone signaling.

In stem cell-based cartilage tissue engineering, TGF-β has been one of the most widely used mediators to drive chondrogenesis and promote tissue growth [8]. Spatiotemporal gradients of TGF-β signaling are critical to the development of stratified native-like cartilage. Importantly, engineered tissues which fail to recapitulate the appropriate tissue anisotropy become unstable and undergo endochondral ossification once implanted *in vivo* [9,10]. Recent work from our lab showed that recapitulation of physiological spatiotemporal TGF-β gradients in an *in vitro* transwell system resulted in engineered human cartilage which was zonally organized and phenotypically stable, presenting a promising new strategy for cartilage tissue engineering [54]. Other tools such as synthetically activated chimeric receptors [89] or nanofiber scaffolds for localized ligand release [90] have been developed to more precisely manipulate TGF-β signaling, but methods which rely on maintenance of a chemical gradient have an inherent lack of fast and specific spatiotemporal control, making them difficult to translate to complex settings, for example to diffusion-limited cultures which require perfusion. Optogenetics is a tool to induce cell behaviors by light stimulation, offering unprecedented precision and dynamic control of cell signaling in space and time. Optogenetics has been used to interrogate molecular mechanisms in single-cell or monolayer cultures [11,91] but has not been applied as a spatiotemporal control strategy for tissue engineering.

Though biochemical and biomechanical interactions at the osteochondral junction are important mediators of joint health and disease, most engineered tissues fail to incorporate both cartilage and bone components in a single construct [12,13,43]. Previous work from our lab demonstrated the utility of bone-like substrates in supporting cartilage formation [12,13], and modeling the joint also requires physical proximity of tissues to study interactions between cartilage, bone, synovium, and other connective tissues [45,46]. The maintenance of precise chemical TGF-β gradients for establishing zonally organized cartilage would be especially challenge in complex multi-tissue settings, however, the proposed light-based spatiotemporal method could be implemented with greater ease.

Thus, we seek to engineer zonally organized human cartilage by applying the appropriate spatiotemporal gradients of TGF-β signaling, while concurrently including a subchondral bone substrate for enhanced osteochondral interactions. The central hypothesis is that the precise regulation of TGF-β signaling and the inclusion of a subchondral bone substrate can generate native-like human articular cartilage with zonal organization and cartilage-bone interactions.

Chapter 3: Aim 1

Validation tissue engineering strategies for achieving *in vivo* cartilage regeneration in a dual-tissue, cartilage-bone temporomandibular defect

The contents of Chapter 3 are based on the following publication:

Wu JY*, Chen D*, Kennedy KM, Yeager K, Bernhard JC, Ng JJ, Zimmerman BK, Robinson S, Durney KM, Shaeffer C, Vila OF, Takawira C, Gimble JM, Guo XE, Ateshian GA, Lopez MJ, Eisig SB, Vunjak-Novakovic G. Tissue engineered autologous cartilage-bone grafts for temporomandibular joint regeneration. Sci Transl Med. 2020 Oct 14;12(565):eabb6683. *Equally contributing authors.

Joint disorders can be detrimental to quality of life. There is an unmet need for precise functional reconstruction of native-like cartilage and bone tissues in the craniofacial space and in particular for the temporomandibular joint (TMJ). Current surgical methods suffer from lack of precision and comorbidities, and frequently involve multiple operations. Studies have sought to improve craniofacial bone grafts without addressing cartilage, which is essential to TMJ function**.** For the human-sized TMJ in the Yucatan minipig model, we engineered autologous, biologically and anatomically matched cartilage-bone grafts for repairing the ramus-condyle unit (RCU), a geometrically intricate structure subjected to complex loading forces. Using image-guided micromilling, anatomically precise scaffolds were created from decellularized bone matrix and infused with autologous adipose-derived chondrogenic and osteogenic progenitor cells. The resulting constructs were cultured in a dual-perfusion bioreactor for 5 weeks before implantation. Six months after implantation,

the bioengineered RCUs maintained their predefined anatomical structure and regenerated full-thickness, stratified, and mechanically robust cartilage over the underlying bone, to a greater extent than either autologous bone-only engineered grafts or acellular scaffolds. Tracking of implanted cells and parallel bioreactor studies enabled additional insights into the progression of cartilage and bone regeneration. This study demonstrates the feasibility of TMJ regeneration using anatomically precise, autologous, living cartilage-bone grafts for functional, personalized total joint replacement. Inclusion of the adjacent tissues such as soft connective tissues and the TMJ disc could further extend the functional integration of engineered RCUs with the host.

3.1 Introduction

There is an unmet need for precise functional reconstruction of native-like cartilage and bone tissues in the craniofacial space and particularly for the TMJ, a complex and highly loaded joint implicated in craniofacial diseases and disorders affecting over 10 million people in the United States alone [17]. Current surgical interventions suffer from lack of precision and comorbidities, and frequently involve multiple operations [19–24]. Some synthetic prostheses have shown early success, but outstanding concerns among surgeons with using alloplastic joint replacements include altered joint loading, metal hypersensitivity, and nickel allergy [27–30]. Taken together, these considerations make the development of an autologous, bioengineered mandibular condyle joint replacement all the more compelling [37].

Engineered tissue constructs offer bioinspired and patient-tailored approaches to the reconstruction of the structural and biological components of the graft. Initial efforts have

focused on tissue engineered bone for the mandible. One recent study proposed an "*in vivo* bioreactor" strategy for repair of a large mandibular defect in a sheep model, allowing the engineered bone to develop against the rib periosteum prior to reconstruction of the defect [92]. Another study in an ovine model developed precise customized synthetic grafts loaded with hydroxyapatite for replacement of the orbital floor, resulting in neovascularization and bone morphogenesis [93]. Our group previously reported a translational study in Yucatan minipigs, in which we engineered anatomically correct autologous bone grafts for reconstructing the RCU. Engineered bone showed regenerative advantage over acellular scaffolds, suggesting that the autologous stromal/stem cells incorporated in the grafts contributed to successful integration and tissue regeneration. Consistently, the rates of bone resorption and replacement appeared more balanced in cellular than acellular engineered grafts [94,95].

Few studies have focused on reconstruction strategies that incorporate a cartilage layer over the underlying bone. The condylar cartilage of the TMJ is essential to its mechanical function, providing resistance to compressive loading and frictionless articulation. In therapeutic approaches to TMJ repair, cartilage regeneration is often the central goal, as cartilage is the tissue being degraded in conditions of arthritis or idiopathic condylar resorption. However, many studies have demonstrated repair of defects more distal from the condylar head, due to the lack of techniques to engineer both cartilage and bone together in one construct to enable total joint repair. In our previous work, implanting engineered bone-only RCU grafts in pigs resulted in the formation of a thin layer of cartilaginous tissue on the condylar head, but this tissue lacked the zonal organization,

biochemical composition, and low friction coefficient of native TMJ condylar cartilage [94]. Several studies have demonstrated repair of small, localized cartilage defects, but do not offer scalability for *in vivo* regeneration of the whole condylar head [96–98]. Importantly, the structure of TMJ cartilage is distinct from hyaline cartilage, with a superficial fibrous layer above proliferative and hypertrophic zones.

Our goal was to overcome the common limitation of previous studies – the lack of mature, stratified cartilage layers that can restore TMJ function in large defects and total joint replacement procedures. To this end, we established the engineering and implantation of autologous, anatomically correct RCUs with stratified cartilage interfacing underlying bioengineered living bone to achieve TMJ regeneration. The performance of cartilage-bone RCUs for TMJ replacement was demonstrated in the Yucatan minipig, an animal model with human-sized TMJ and adequate jaw anatomy, loading, and remodeling [99–101]. We compared the performance of anatomically precise cartilage-bone grafts to that of bone-only grafts and acellular scaffolds, hypothesizing that inclusion of a cartilage precursor leads to improved graft quality. We advanced the design and capabilities of our previously established bioreactors for cultivation of anatomically shaped bone [94,102] into a dual-perfusion bioreactor for cultivation of an anatomically correct RCU comprised of cartilage and bone regions formed from the same autologous population of adipose-derived stromal/stem cells (ASCs). This complex tissue graft was evaluated against contralateral native tissues, bone-only grafts without a cartilage region, and acellular scaffolds over 6 months of orthotopic implantation in a clinically sized animal model. We also investigated

the roles of implanted cells in the progression of cartilage and bone regeneration via cell tracking *in vivo* and parallel bioreactor studies.

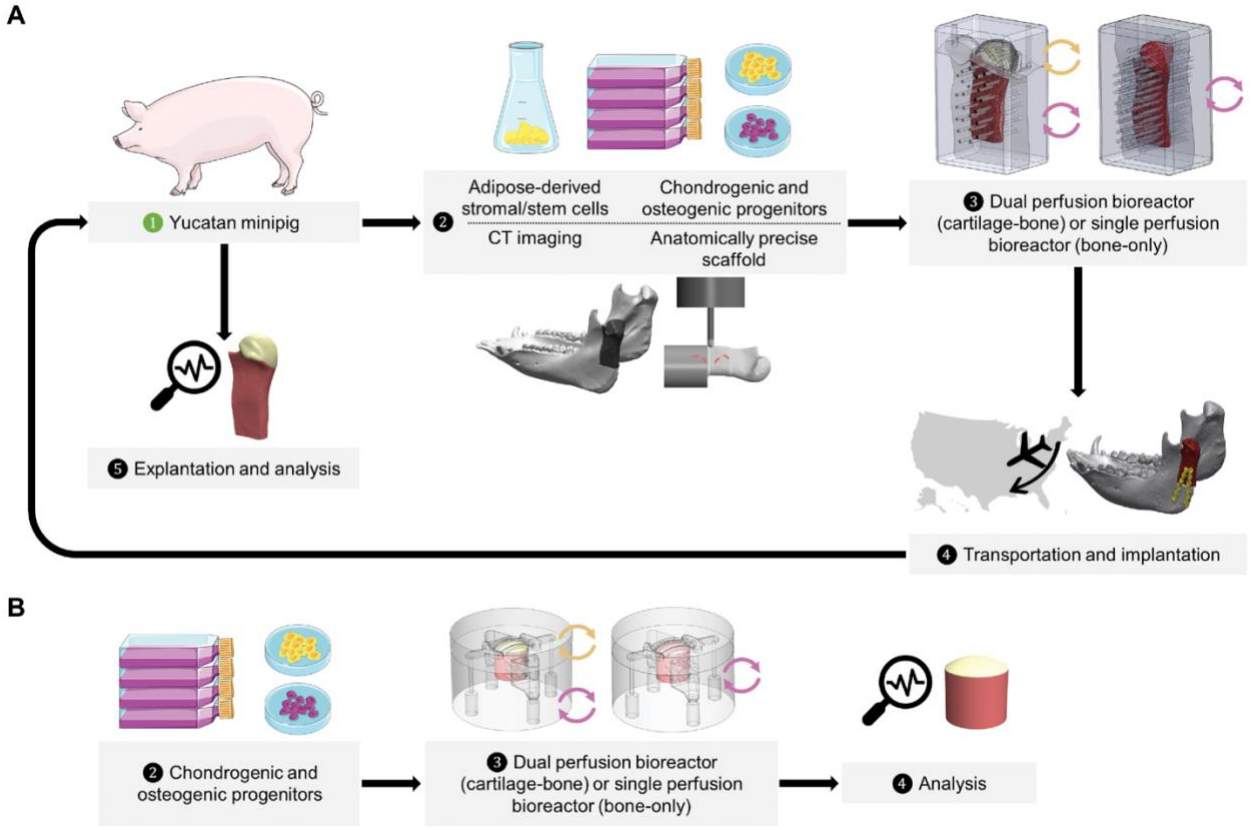

Figure 3.1. Graphical overview of Aim 1. (A) Twenty Yucatan minipigs were housed in Baton Rouge, LA and allowed to reach skeletal maturity. CT imaging of the skull enabled the creation of anatomically precise scaffolds and bioreactor culture chambers. Autologous adipose-derived stromal/stem cells (ASCs) were expanded and differentiated into chondrogenic and osteogenic progenitors. Each decellularized bovine scaffold (~3 cm in width by 6 cm in length by 7 to 25 mm in thickness) was seeded with cells from the corresponding animal and cultured in a dual perfusion bioreactor to form a graft. Experimental groups were cartilage-bone (seeded with ~200 million chondrogenic progenitors and ~120 million osteogenic progenitors), bone-only (seeded with osteogenic progenitors only), and acellular (decellularized scaffold only) ramus-condyle units (RCUs). RCUs were transported from New York, NY to Baton Rouge, LA and orthotopically implanted. After 6 months, the RCUs and the native contralateral tissues were excised and analyzed. **(B)** Smaller-scale cylindrical constructs (~9 mm in diameter and height) were engineered to correspond to a core taken from the center of the RCU condyle to be used for time point analyses. Cell and scaffold sources were the same as in **(A).**

3.2 Results

3.2.1 Dual Perfusion Bioreactors Enable Development of Cartilage-Bone RCUs

Our objective was to engineer autologous cartilage-bone RCUs with patient-specific geometry at a clinically translatable scale. To this end, we used anatomically matched decellularized bone matrix scaffolds, autologous ASCs, and dual perfusion bioreactors with separate compartments and culture media for bone and cartilage cultivation **(Figure 3.1A).** We used a similar process to engineer bone-only RCUs in a single perfusion bioreactor, as previously described [103].

Scaffolds were derived from the trabecular bone of bovine distal femurs, completely decellularized, and milled into anatomically precise replicas of each animal's RCU based on computed tomography (CT)-guided reconstructions, with each RCU measuring about 3 cm in width by 6 cm in length and 0.7 cm in thickness at the base and 2.5 cm in thickness at the condylar head.

For each animal, we isolated ASCs from a small (100 mL) subcutaneous adipose biopsy and expanded the cells to sufficient numbers. No bone morphogenic proteins nor any other growth factors were used for osteogenic culture. For cartilage formation, condensed mesenchymal bodies were formed from the ASCs and seeded onto the RCUs as previously described [12]. The only growth factor used for chondrogenic culture was TGF-β, which is known to be critical for chondrogenic induction. ASCs from each animal were added to the corresponding scaffold, except for the scaffolds that served as acellular controls.

Dual perfusion bioreactors were fabricated to match the graft geometry of each animal **(Figure 3.2).** The bioreactors supported the cultivation of cartilage-bone RCUs by

enabling sufficient transport of nutrients, oxygen, and metabolites while also providing specific physical cues and culture media for each tissue type, because the cartilage and bone require different culture conditions. Low hydrodynamic shear yields better cartilaginous tissue [13,104] while higher hydrodynamic shears induced by interstitial velocities in the bone favor osteogenic maturation [103,105]. Using computational flow simulation, the number, placement, and diameter of bioreactor channels were designed to provide interstitial velocities ranging from 400 to 1200 μm/s, depending on the graft thickness at each channel. Thorough and rapid perfusion of the scaffold without leaks was confirmed experimentally by flowing medium through the bone in the bioreactor before adding cells. A 1 μm porous polycarbonate membrane between the condylar surface and perfusion channels was placed to shield the neocartilage and reduce shear forces to negligible rates while allowing for medium exchange. To provide tissue-specific chemical cues, chondrogenic or osteogenic culture media were distributed to the appropriate regions of the RCU via separate fluid flow loops. Single perfusion bioreactors for the bone-only RCUs were similarly fabricated and validated computationally and experimentally to promote osteogenic maturation.

After 5 weeks of culture, the RCU bioreactors were shipped from Columbia University in New York, NY, where the grafts were grown, to Louisiana State University in Baton Rouge, LA, where the animals were housed. During transport between these geographically distant sites, perfusion was discontinued for up to 10 hours. Previous computational modeling from our group of oxygen transport and consumption in RCUs of comparable dimensions indicated that the oxygen concentration after 10 hours within the RCUs was still sufficient

for cell survival [103]. The large RCUs were then implanted into recipient animals. The cellularity after transportation was not notably different from the cellularity before transportation in large grafts [103]. The RCUs remained implanted for 6 months and were subsequently analyzed by histological staining, biochemical assays, and mechanical testing.

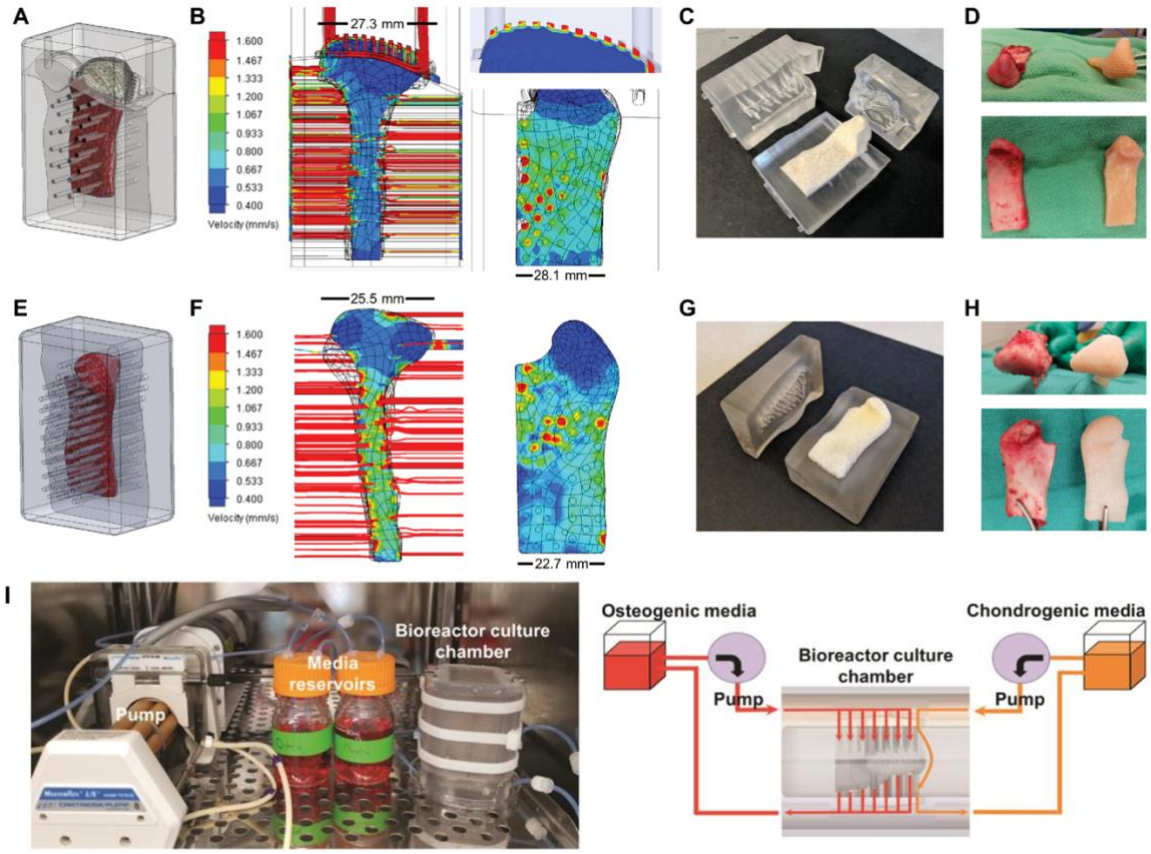

Figure 3.2. Bioreactor cultivation of engineered grafts. Left to right: Schematics showing engineered grafts in bioreactor culture chambers with perfusion channels; simulated equilibrium flow rates in cartilage and bone components; preculture photographs demonstrating the precise fit of scaffolds within elastomer blocks, which form the inner bioreactor culture chamber; and post-culture photographs of engineered RCUs and the corresponding excised native RCU at time of surgery or the small cylindrical constructs. **(A to D)** Dual perfusion bioreactor design and modeling for anatomical cartilage-bone RCUs (~3 cm in width by 6 cm in length by 7 to 25 mm in thickness). **(E to H)** Single perfusion bioreactor design and modeling for anatomical bone-only RCUs. **(I)** Photograph (left) and schematic (right) of the setup for anatomical cartilage-bone dual perfusion bioreactors, including the pump, chondrogenic and osteogenic media reservoirs, corresponding tubing, and culture chamber.

3.2.2 Engineered Cartilage in RCUs Recapitulates Key Features of Native TMJ Cartilage

After 6 months *in vivo*, the macroscopic quality of the cartilage in each engineered RCU was compared immediately after dissection to the same animal's native RCU on the contralateral side. The appearance of the cartilage and the shape of the joint were best recapitulated in the cartilage-bone group and were the least native-like in the acellular control group **(Figure 3.3A).** The 6-month post-implantation engineered cartilage-bone RCUs closely recapitulated the native samples with respect to overall cartilage thickness and the presence of distinct and typical cartilage zones. Moving from the superficial surface to the subchondral bone, the fibrous, proliferative, hypertrophic, and calcified zones were established. Unlike the hyaline cartilage on other joints, the porcine TMJ cartilage is known to have a fibrous superficial layer dominated by collagen I [106]. These stratified layers are important for recapitulating the functional responses of the cartilage under compressive and shear loading. In contrast, the bone-only RCUs and acellular samples were mostly dominated by a fibrous layer and lacked the requisite proliferative and hypertrophic zones. The relative layer thicknesses of the native samples were more closely matched in the cartilage-bone group (all zones, not significant) than in the bone-only and acellular groups (all zones, $P < 0.05$) **(Figure 3.3B).** The inclusion of chondrogenic precursors during RCU cultivation *in vitro* ultimately resulted in better cartilage regeneration after 6 months of orthotopic implantation. The acellular controls exhibited worse morphology and cartilage could not be reliably sampled, and therefore, subsequent cartilage analyses focused on elucidating the differences among the cellularized grafts and native tissue.

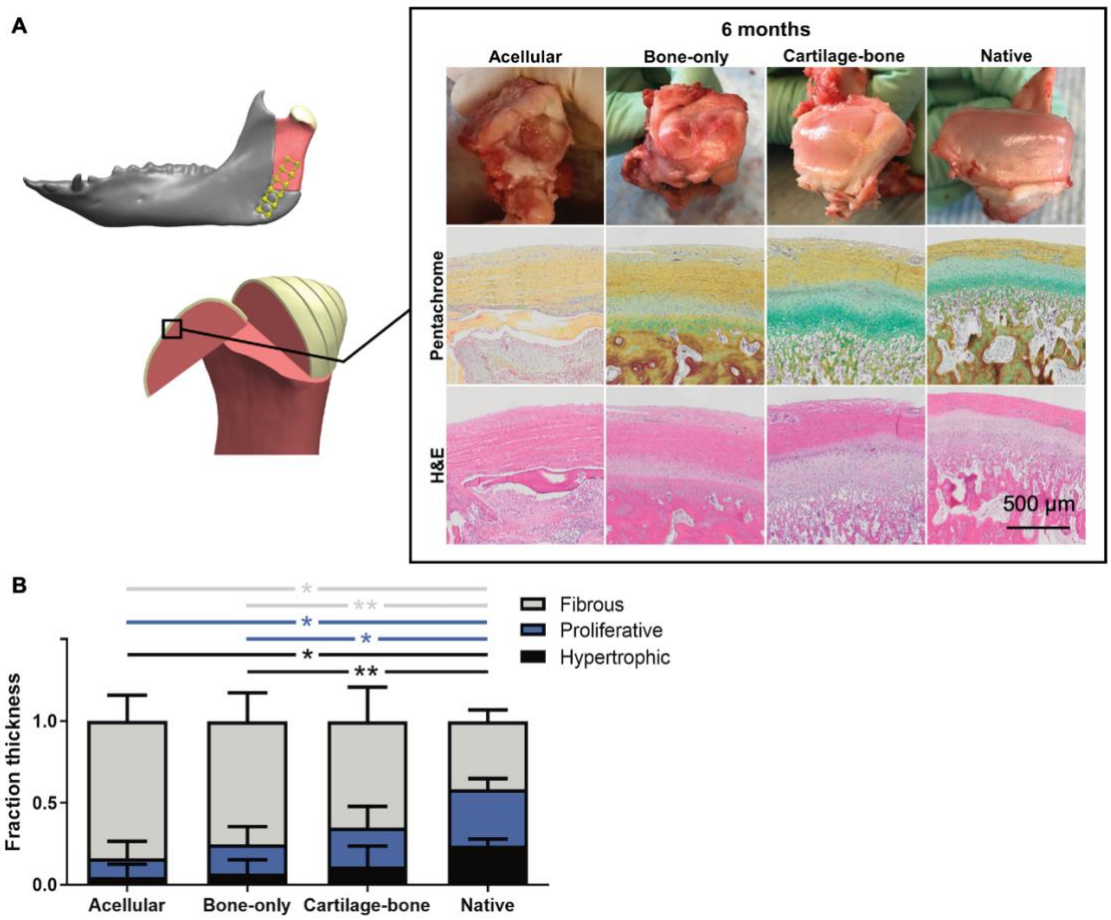

Figure 3.3. Histological properties of engineered cartilage. (A) Schematic and representative photographs, Movat's pentachrome, and hematoxylin and eosin (H&E) stains of implanted and native RCUs from sagittal condylar cross sections. **(B)** Zonal distribution relative to total cartilage thickness. Data are means ± SD [n = 3 acellular, 8 bone-only (BO), 5 cartilage-bone (CB), and 19 native]. *P* values were determined by Kruskal-Wallis with Dunn's multiple comparison post hoc test.

In terms of biochemical composition, glycosaminoglycan (GAG) content per unit of wet weight was significantly higher in native tissue (11.2 ± 2.6 μg/mg) than in cartilage-bone explants (8.8 ± 3.2 μg/mg; $P < 0.05$) or bone-only explants (7.9 ± 3.3 μg/mg; $P < 0.01$) 6 months after implantation **(Figure 3.4C)**. DNA and hydroxyproline (OHP) expression showed no significant difference across experimental groups **(Figure 3.4B, 3.4D).** Although

the OHP assay found no difference in total collagen content between groups, stains for collagen I, the dominant component of the fibrous cartilage, appeared to be most prominent in the bone-only group, but relatively less present in the cartilage-bone and native groups, as determined from qualitative analysis **(Figure 3.4A).** Stains for collagen II, the predominant solid component of the hyaline cartilage and the deeper zone mandibular condylar cartilage, were comparably strong in condylar sagittal cross sections from the cartilage-bone and native groups but noticeably weaker in the bone-only group.

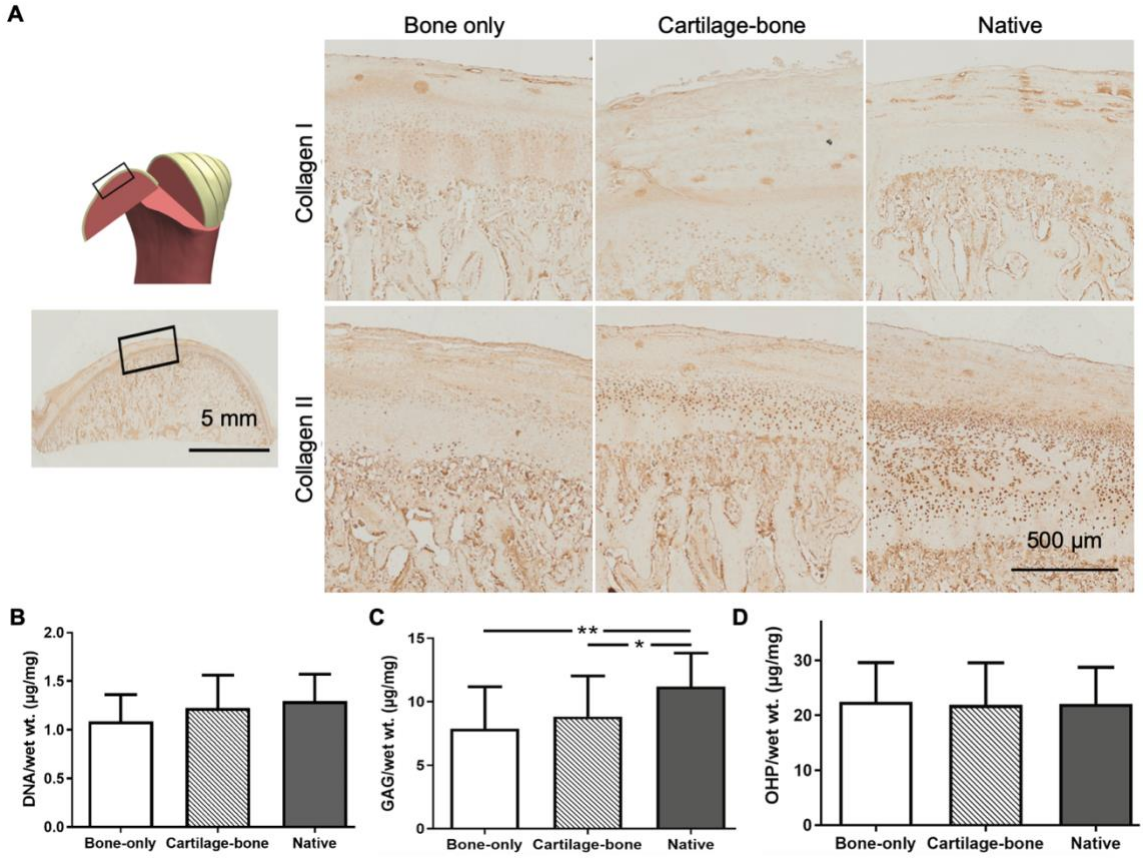

Figure 3.4. Histological and biochemical properties of engineered cartilage. (A) Representative immunohistochemistry of collagen I and II from sagittal condylar cross sections. Images taken from the indicated area on a low magnification image of a native sample. **(B to D)** DNA, GAG, and total collagen (OHP) content normalized to wet weight (wt.). Data are means ± SD (n = 13 BO, 11 CB, and 48 native). P values were determined by one-way ANOVA with Tukey-Kramer's multiple comparison post hoc test. *$P < 0.05$ and **$P < 0.01$.

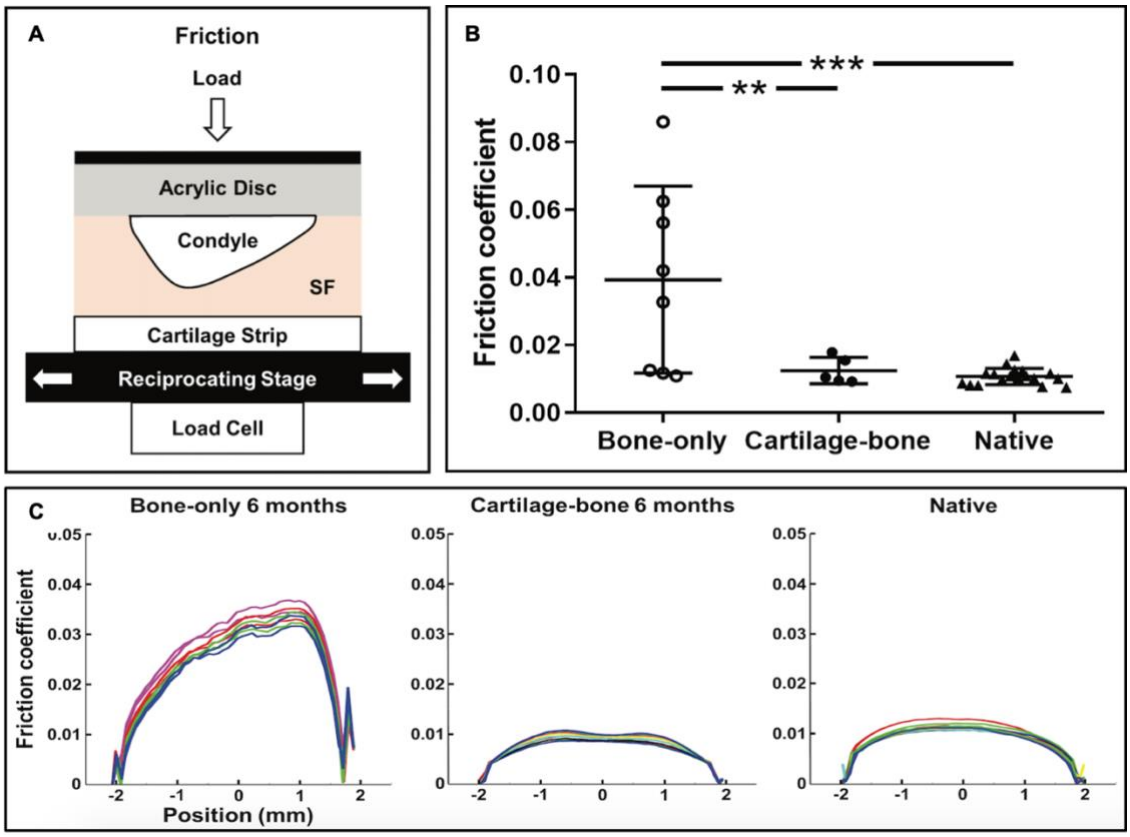

Figure 3.5. Tribological properties of the engineered cartilage. Cartilage-bone RCUs achieved native-like mechanical and tribological properties after 6 months *in vivo.* **(A)** Schematic of friction testing setup. Mean friction coefficient was calculated for a 20-min oscillating test with a 4.45 N sliding load at 1 mm/s on the intact condyle against a cartilage counterface in synovial fluid (SF). **(B)** Friction coefficients of RCU condyles in CB, BO, and native cartilage samples. Data are means ± SD (RCUs: n = 8 BO, 5 CB, and 18 native). P values were determined by one-way ANOVA with Tukey-Kramer's multiple comparison post hoc test. **P < 0.01 and ***P < 0.001. (C) Representative friction cycle curves. Implanted ramus-condyle units (RCUs) had values of 0.01–0.05.

The friction coefficient of each condylar surface was determined under a 4.45N sliding load moving at 1 mm/s for 20 min against a flat cartilage counterface in a synovial fluid bath **(Figure 3.5A)**. The entire condylar surface was measured in intact state, representing more physiologically faithful conditions compared to conventional testing of punch biopsy samples. The cartilage-bone RCUs achieved physiological friction coefficients

with no significant difference between the engineered cartilage (0.012 ± 0.004) and native TMJ cartilage (0.011 ± 0.002) **(Figure 3.5B, 3.5C).** In comparison, the bone-only RCUs (0.039 ± 0.028) had significantly higher friction coefficients than either the cartilage-bone ($P < 0.01$) or native ($P < 0.001$) groups.

3.2.3 Engineered Bone Exhibits Comparable Features in Cartilage-Bone and Bone-Only RCUs but not in Acellular Controls

Previous work demonstrated that the *in vitro* formation of cartilage is markedly facilitated by the underlying decellularized bone matrix [12]. Clinically, it is known that the subchondral bone plays a role in the initiation and progression of cartilage damage [45,46]. We were interested in the effects of the cartilage layer on the formation of the subchondral bone. Masson's trichrome staining of the subchondral bone showed a positive progression from osteoid-heavy, immature bone tissue in the acellular implants, to more mature bone matrix in the cartilage-bone RCUs after 6 months *in vivo* **(Figure 3.6A).** Stains for known osteogenic markers in the RCUs further confirmed the native-like morphology of engineered subchondral bone. Compared to native samples, stains from the cartilage-bone and bone-only groups were similarly positive in osteocalcin (OCN) and osteopontin (OPN). For bone sialoprotein (BSP), cartilage-bone and native samples appeared to stain similarly, whereas bone-only samples stained weaker **(Figure 3.6B).**

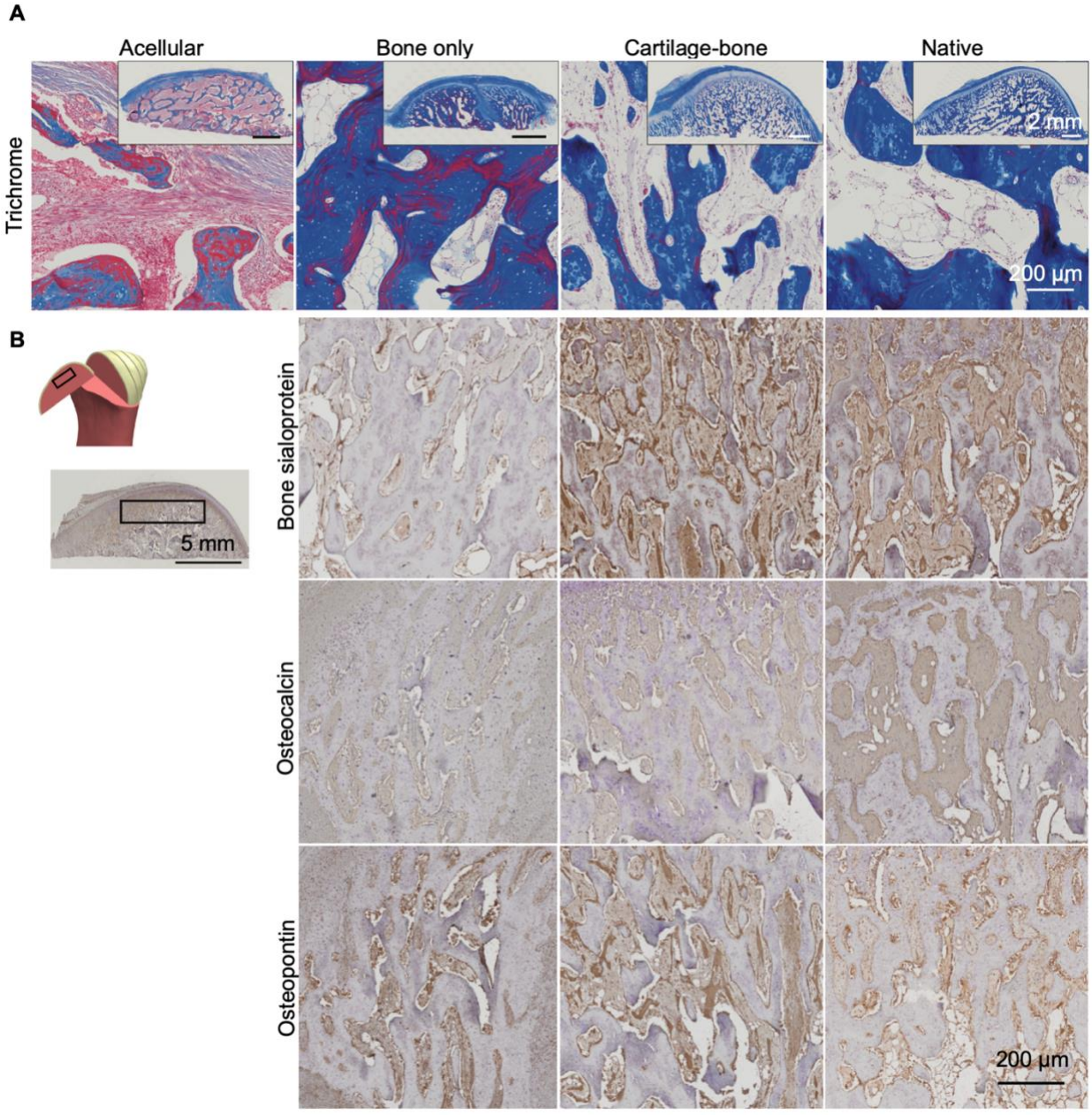

Figure 3.6. Histological properties of engineered bone. (A) Representative Masson's trichrome staining in sagittal subchondral cross sections of acellular, bone-only (BO), cartilage-bone (CB), and native samples. **(B)** Schematic and representative immunohistochemistry staining for common bone markers bone sialoprotein, osteocalcin, and osteopontin.

3.2.4 Engineered Cartilage-Bone Grafts Served as Templates for Tissue Regeneration

To investigate the role of the implanted ASCs in the regenerative process, groups of RCUs contained green fluorescent protein (GFP)-tagged chondrogenic progenitors or GFP-tagged osteogenic progenitors. It was difficult to directly visualize cell fluorescence within the excised tissues; however, we located labeled cells via positive anti-GFP immunohistochemical staining in both cartilage-bone and bone-only groups after 6 months *in vivo* **(Figure 3.7)**. GFP-tagged chondrogenic progenitors were found throughout the condylar region of the RCU, both within the cartilage surface where they were first seeded and extending into the subchondral bone. GFP-tagged osteogenic progenitors were found throughout the ramus where they were initially seeded in the RCU but also further up into the remodeled subchondral bone, suggesting that these cells and their progeny played a role in the regeneration process, at least near the condyle. GFP-tagged cells were seen across the graft volume but not in the native bone surrounding the implanted RCU, indicating that these cells did not migrate out of the graft into the surrounding bone.

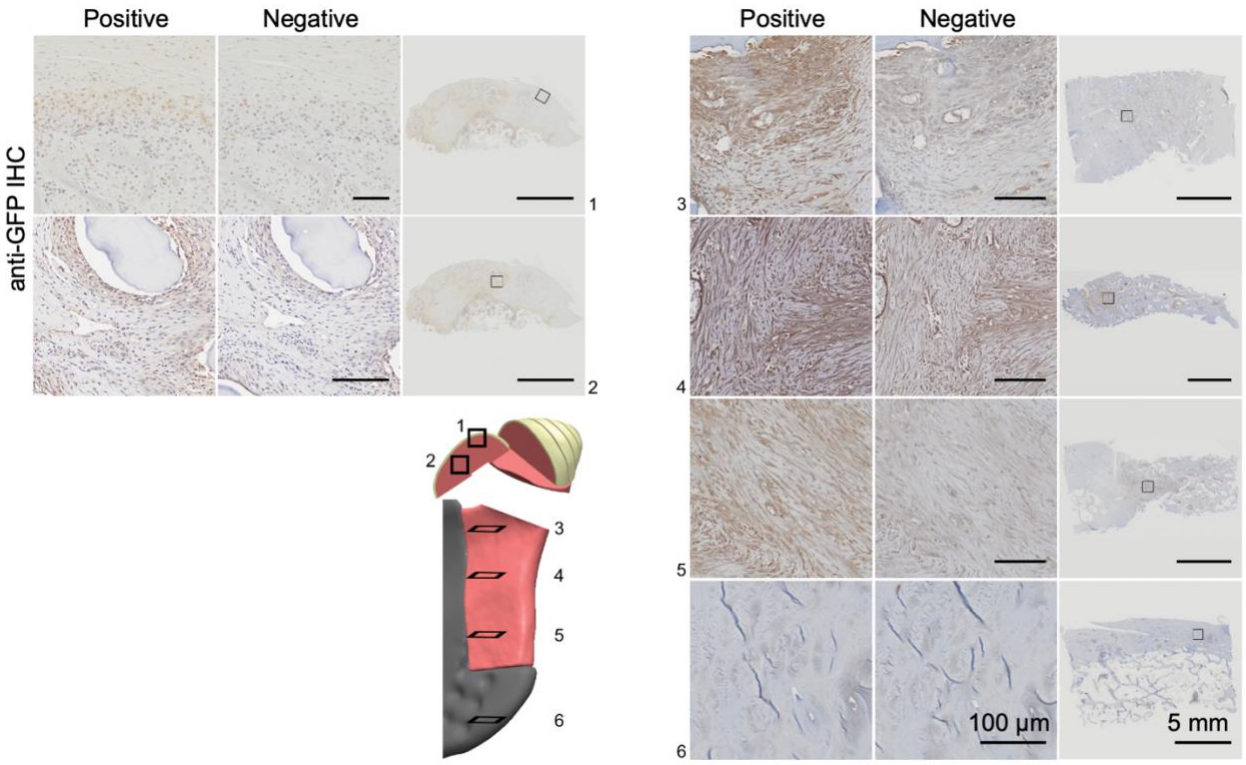

Figure 3.7. Visualization of ramus-condyle regeneration by fluorescent tags. Anti-GFP immunohistochemistry (IHC) staining of sagittal condyle cross sections (left) and transverse ramus cross sections (right). GFP-tagged chondrogenic and osteogenic progenitors were present throughout the graft after 6 months in vivo. GFP-tagged progenitors were not located in native tissue surrounding the graft. Negative IHC is shown to account for nonspecific background staining, with darker brown staining in positive IHC panels indicating GFP-positive cells.

To better understand the processes contributing to tissue development, we engineered additional small cylindrical constructs with representative curvature of the articulating surface and investigated these constructs in bioreactor studies, in parallel with the clinically sized cartilage-bone and bone-only RCUs **(Figure 3.1B)**, and cultured in the dual-tissue perfusion bioreactors for 5 weeks. For the smaller constructs, scaffold dimensions (9 mm diameter and 9 mm height) and surface curvature were chosen such that they would be representative of a core taken from the center of the condylar head of the RCU.

Scaffolds for the small constructs were seeded at the same densities as their larger counterparts, using a heterogeneous population of ASCs from several animals (n = 7) to normalize for biological differences between experimental groups. Additional dual and single perfusion bioreactors were designed for the small constructs (cartilage-bone and bone-only) such that each tissue type experienced the optimal range of hydrodynamic shear, corresponding to that in the bioreactors for the larger RCUs **(Figure 3.8A-3.8C)**. We created an additional perfusion bioreactor prototype with glass surfaces to allow for *in situ* imaging of a condylar section **(Figure 3.8E).**

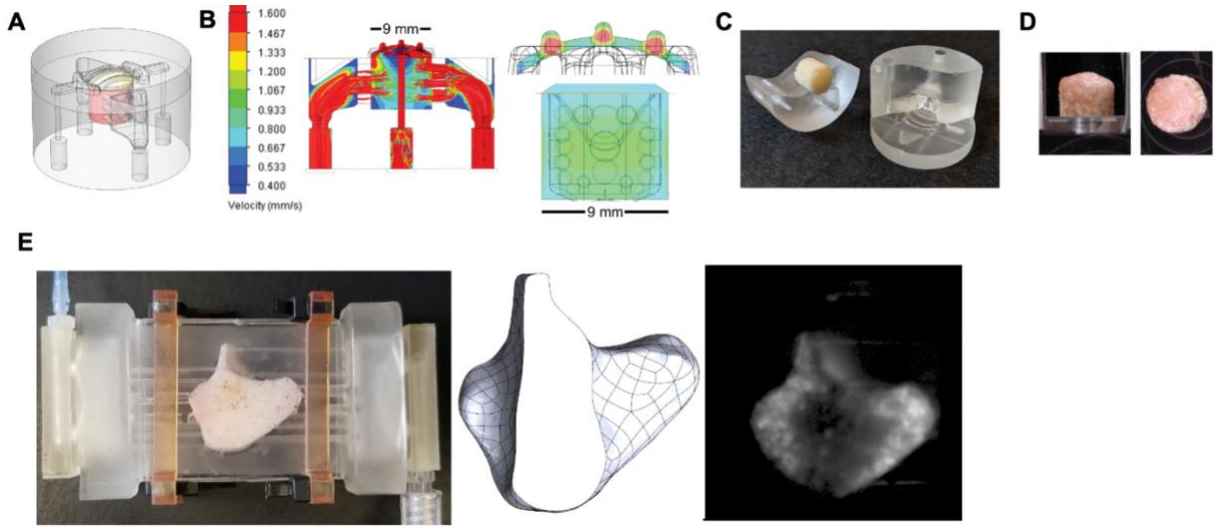

Figure 3.8. Bioreactor cultivation of engineered *in vitro* constructs. (A to D) Scaled-down cartilage-bone bioreactor for small cylindrical constructs, about 9 mm in diameter. Left to right: Schematics showing engineered constructs in bioreactor culture chambers with perfusion channels; simulated equilibrium flow rates in cartilage and bone components; preculture photographs demonstrating the precise fit of scaffolds within elastomer blocks, which form the inner bioreactor culture chamber; and postculture photographs of the small cylindrical constructs. **(E)** Glass surface perfusion bioreactor with bioluminescent imaging capability designed for cultivation of anatomical condylar bone section.

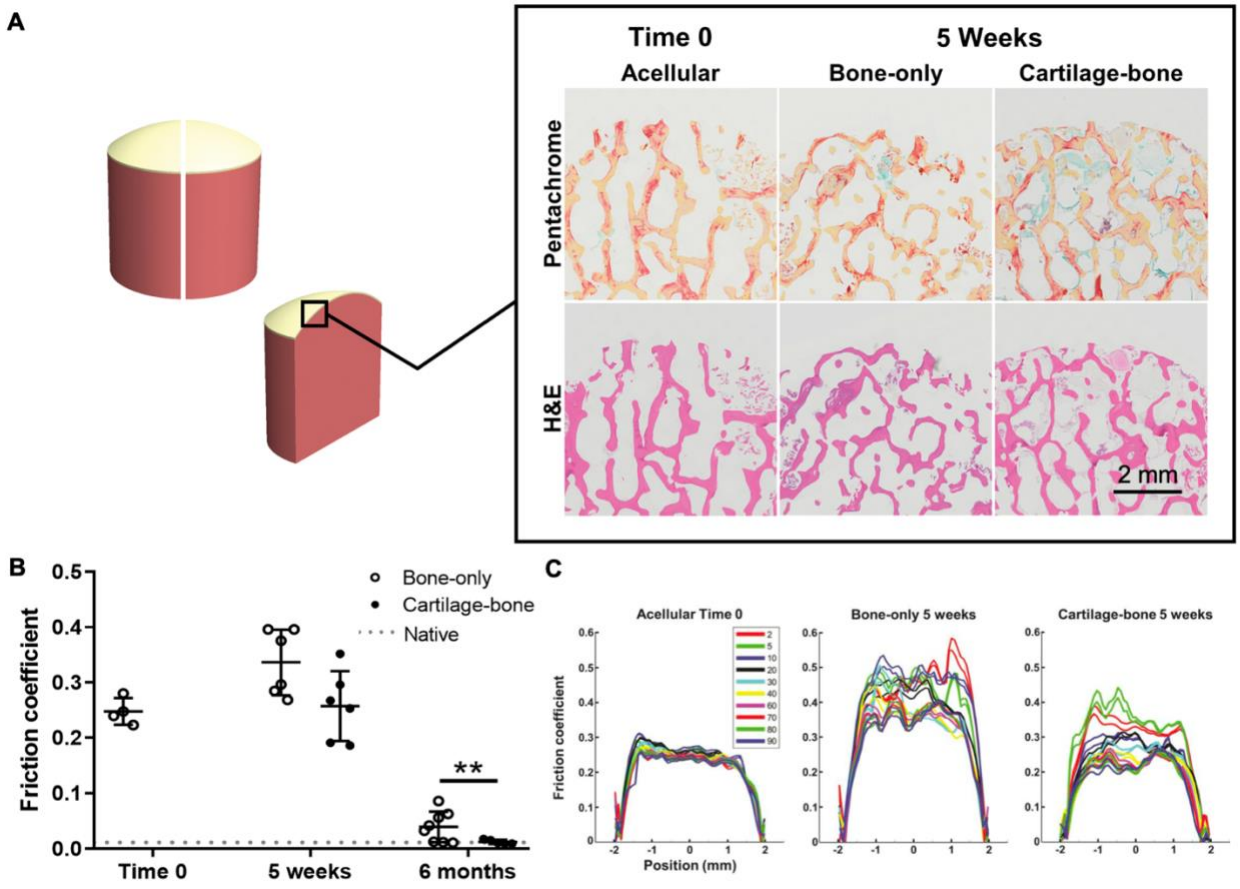

Figure 3.9. Histological and tribological properties of engineered small *in vitro* constructs. (A) Schematic and representative Movat's pentachrome and H&E staining of small constructs. **(B)** Friction coefficients for CB, BO, and native RCU condyles at different time points after implantation. Data are means ± SD (RCUs: n = 8 BO, 5 CB, and 18 native; small constructs: n = 4 acellular, 6 BO, and 6 CB). P values were determined by one-way ANOVA with Tukey-Kramer's multiple comparison post hoc test. **P < 0.01. **(C)** Representative friction cycle curves. Small in vitro constructs had friction coefficients of 0.3–0.5.

We hypothesized that our cartilage-bone RCU would serve as a template for remodeling and regeneration, rather than a direct replacement of the native tissue. To this end, we compared tissue properties before implantation (after 5 weeks of bioreactor culture) and after 6 months *in vivo*. The small difference in cartilage friction coefficients between the cartilage-bone group and bone group at the end of *in vitro* culture markedly

increased by 6 months of implantation, with cartilage-bone group reaching the frictionless behavior of native tissue samples **(Figure 3.9B, 3.9C).** These results are consistent with the thin cartilage layers on the small constructs that were observed macroscopically and histologically **(Figure 3.8D, 3.9A).**

3.3 Discussion

We engineered human-sized, anatomically precise cartilage-bone grafts representing an entire ramus-condyle unit (RCU) for repairing the lower jaw, by bioreactor culture of autologous ASCs in decellularized bone scaffolds. In a human-size animal model (Yucatan minipig), we demonstrated the utility of these grafts for the functional repair of the ramus-condyle region in healthy animals. Using CT scans of each animal (to fabricate the scaffold and the matching bioreactor chamber) and a minimally invasive adipose tissue harvest (to generate therapeutic cells), each graft was prepared in an animal-specific manner.

To mimic the envisioned centralized production of the grafts and their distribution to hospitals, the grafts were cultured at one location (New York, NY) and implanted at another, distant location (Baton Rouge, LA). For further clinical reference, the implantations were conducted by an expert maxillofacial surgeon, using standard clinical protocols and tools for TMJ surgery.

The advantages of implanting the RCU containing a cartilage layer integrated with the underlying condyle bone as compared to the bone-only and acellular grafts were evidenced by the superior appearance, morphology, biochemical content, and mechanical properties of the cartilage-bone grafts following 6 months of implantation. This achieved native-like cartilage formation in the reconstruction of a large, load-bearing craniofacial defect.

Towards the treatment of large cartilage-bone defects using tissue engineering approaches, early work focused on establishing the optimal environment to support regeneration. The use of the *in vivo* environment as a bioreactor helped inspire designs of more advanced *in vitro* bioreactors [107–109]. For craniofacial tissue engineering in particular, initial efforts targeted the repair of small bone-only defects in non-load bearing-regions of the skull [110–113]. More recent work addressed large defects in load-bearing regions of the mandible, but primarily emphasized bone formation and integration [92,94]. Some studies have attempted to incorporate cartilage with bone, but have primarily done so *in vitro* with decellularized bone matrix [96,97]. Functional repair of ramus-condyle defects relies on the presence of both tissue types – cartilage and bone. Our study bridges this gap by incorporating a cartilage layer on top of a large living bone graft, thereby taking an important step towards clinical translation of engineered grafts. After 6 months *in vivo*, the resulting cartilage-bone RCUs recapitulated key native-like features within the regenerated cartilage. Using the bone-only RCUs and native contralateral tissues as benchmarks, the cartilage-bone RCUs produced cartilage with better gross appearance, zonal distribution, and expression of key markers. In particular, the cartilage of the cartilage-bone and native samples contained mostly collagen II, whereas the bone-only samples predominantly featured collagen I. This corroborates the more fibrocartilaginous profile of the cartilage in the bone-only RCUs and could explain why the total measured collagen was similar amongst the groups. Though biochemical analyses of small local biopsies indicated no significant difference in GAG content between cartilage-bone and bone-only RCUs, comprehensive pentachrome staining revealed the spatial distribution of GAGs throughout the entire sagittal

condylar plane with more native-like zonal organization in the cartilage-bone group. Future studies should perform additional quantitative enzyme-linked immunosorbent assay (ELISA) analyses for collagen and GAG subtypes.

The cartilage-bone RCUs successfully restored functionality of the jaw, as indicated by the native-like mechanical properties of the cartilage layer 6 months post-implantation. Non-destructive mechanical tests were conducted on the entire fresh condylar head, to mimic physiological loading conditions as closely as possible. Because measured values can be affected by the testing setup and parameters, we benchmarked our values using the native contralateral side in addition to the literature data on native porcine TMJ. This approach allowed rigorous mechanical and tribological testing of large tissue-engineered condyles.

Cartilage-bone RCUs had low, native-like friction coefficients unlike their bone-only counterparts. The 6-month post-implantation cartilage-bone RCUs achieved an average friction coefficient (0.012) that closely matched that of native cartilage (0.011), with both values being significantly lower than the coefficients achieved by the bone-only RCUs (0.039). Compared to bulk measurements of cartilage properties such as Young's modulus, the friction coefficient may be a more realistic indicator of the properties of the cartilage layer, as it is largely determined by the superficial layer of cartilage. Bite force measurements, imaging of mastication patterns, and analyses of synovial fluid and TMJ disc could provide additional insights into the quality and function of the regenerated cartilage.

Previous work demonstrated that the *in vitro* formation of cartilage is markedly facilitated by the underlying decellularized bone matrix [96]. Clinically, it is known that subchondral bone plays a role in the initiation and progression of cartilage damage [114–

116]. We were interested in the effects of the cartilage layer on the formation of subchondral bone. Indeed, the subchondral bone in the 6-month post-implantation cartilage-bone RCUs recapitulated the mature bone matrix and trabecular distribution of the native tissue, in contrast to the more variable and osteoid-heavy immature bone matrix of the bone-only and acellular RCUs. The key marker BSP appeared more highly expressed in the subchondral bone of cartilage-bone RCUs compared to bone-only RCUs, whereas OCN and OPN were similarly stained.

In addition to demonstrating safe and effective repair of the large defects in the lower jaw using engineered RCUs, our objective was to investigate the progression of the regenerative processes and the respective contributions of the living cartilage and bone regions. We hypothesized that the engineered cartilage-bone RCU would serve as a template for remodeling and regeneration, rather than a direct replacement of the native tissue. To this end, we compared tissue properties pre-implantation (after 5 weeks of bioreactor culture) and after 6 months *in vivo*. The inclusion of a cartilage precursor positively contributed to tissue regeneration *in vivo,* as seen by the more native-like phenotype of cartilage in the cartilage-bone RCUs compared to the bone-only RCUs. Consistently, the small difference in cartilage friction coefficients between the cartilage-bone group and bone group at the end of *in vitro* culture markedly increased by 6 months of implantation, with cartilage-bone group reaching the frictionless behavior of native tissue samples. The GFP-positive cartilage or bone precursor cells initially seeded in grafts that we were able to locate after 6 months of implantation indicated that the implanted cells had lasting contributions to regeneration. Another fluorescent tag, oxytetracycline, allowed us to identify the areas of

calcium deposition within implanted RCUs in both the subchondral and ramus regions of the bone and indicated that further remodeling took place after the 3-month mark. Taken together, these data provided two important insights: (i) the majority of tissue remodeling and regeneration occurred *in vivo*, and (ii) the progression and outcomes of tissue regeneration depended on the properties of the engineered graft. The cartilage-bone RCUs served as the most effective regeneration templates, resulting in the best structural and functional tissue properties.

A limitation of this study is the lack of histomorphological and biomechanical analyses at additional timepoints to better understand the regenerative processes which occur *in vivo*. Studies over longer periods of time would lead to more detailed understanding of the remodeling of engineered RCUs. Future studies should not only focus on temporal analyses, but also make use of alternative labeling methods for longitudinal cell and extracellular matrix tracking [117]**.** In addition, it has been shown in many tissue types that mechanical conditioning can help create more mature tissues *in vitro* [118–120]. Because healthy bone remodeling depends on appropriate mechanical stimuli [121], a more advanced bioreactor should have both loading and perfusion capabilities.

The engineered bone in this study was comprised of decellularized bovine bone matrix and osteogenic porcine cells. We hypothesized that the inclusion of additional cell types such as osteoclasts, endothelial and stromal cells would further improve the integrity of our engineered bone. From a disease modeling perspective, it would also be advantageous to develop a model incorporating more cell types. Particularly in the TMJ, vascularization and chondrocyte-osteoblast transdifferentiation were recently reported to play a role in

osteoarthritis and other pathologies [122]. Our study was conducted in healthy animals, and future studies are needed to evaluate the graft performance in more challenging diseased joint environments. Though age was randomly distributed between experimental groups, the animals in our study were relatively young overall, between 13 to 23 months at the time of graft implantation, and all animals were male. Future studies are needed to understand the potential contributions of ASC donor and engineered graft recipient ages to regenerative outcomes, and to investigate any sex-based differences. Finally, inclusion of the adjacent tissues such as soft connective tissues and the TMJ disc [123,124] could further extend the functional integration of engineered RCUs with the host.

The animals in this study were immediately allowed to return to a solid diet, and the positive performance of our implanted grafts may suggest limiting the duration of jaw immobilization in patients after an analogous procedure. The 11-week preparation and *in vitro* culture period is compatible with the timeline of two-stage maxillofacial reconstruction, which is widely used for many clinical indications, from cancer surgery to traumatic injury. The time between the first operation (damaged tissue resection, space maintainer placement) and the second operation (graft reconstruction) usually spans several months, allowing ample time to prepare and culture patient-tailored living autologous grafts [125,126]. The time limiting step in our current protocol is the expansion of cells to usable numbers. We chose to conduct this initial study using autologous cells for rigor of experimental design. Notably, mesenchymal stromal/stem cells have substantial immune privilege and can be transplanted between HLA-incompatible patients without adverse response [127], an option that needs to be validated, as it would lead to an off-the-

shelf therapy. Overall, this study resulted in a promising approach to large-scale joint reconstruction using viable tissues and opened several avenues of investigation.

3.4 Conclusion

This study demonstrated the feasibility of TMJ regeneration using anatomically precise, autologous, living cartilage-bone grafts for functional, personalized total joint replacement. After 6 months *in vivo*, the engineered cartilage-bone grafts recapitulated key native-like features: zonally organized cartilage which covered the articulating surface and had low friction coefficients, as well as mature bone matrix in the subchondral region. As indicated by histological and functional properties at 5 weeks post-bioreactor culture versus 6 months post-implantation, our cartilage-bone RCU served as a template for remodeling and regeneration, rather than a direct replacement of the native tissue. This motivated the work described in the subsequent chapters, in which we built on tissue engineering strategies developed in this study to investigate and promote the processes which contribute to the development of more native-like cartilage in an *in vitro* engineered model.

3.5 Materials and Methods

3.5.1 Study Design

Our objective was to engineer autologous, living, anatomically correct cartilage-bone craniofacial grafts for implantation using adipose-derived stromal/stem cells (ASCs), native bone matrix scaffolds, image-guided fabrication methods, and dual-perfusion bioreactors with the cartilage and bone regions independently supplied by their optimal media and regulatory signals. We hypothesized that immature cartilage and bone tissues formed *in vitro*

would serve as effective templates for functional tissue development, maturation, and integration *in vivo*. Bioengineered grafts were investigated for their capacity to regenerate the ramus-condyle unit (RCU) to a native-like state during a 6-month period of implantation in Yucatan minipigs. To recapitulate the envisioned clinical application of bioengineered grafts that will be prepared at centralized locations and shipped to hospitals for implantation, the grafts were cultured in our laboratory in New York City and implanted into animals residing in Baton Rouge, LA (a 10-hour distance door to door).

Three groups of bioengineered grafts were investigated: (i) cartilage-bone RCUs (the main experimental group), (ii) bone-only RCUs (to assess the regenerative ability of bone and any spontaneous generation of cartilage), and (iii) acellular scaffolds (to assess the role of exogenous cells in regeneration); data for the condylectomy (no treatment group) are available from our previous study in the same animal model [94]. Selection of animals into the experimental groups was randomized. The cells used to seed the scaffolds were derived from a small fat sample (100 mL) taken from each animal (autologous cells). The scaffold and bioreactor chamber for each animal were specifically made using image-guided fabrication to fit the exact geometry of that animal's defect. Tissue outcomes included histology, immunostaining, and mechanical testing.

To understand the regenerative processes driven by our grafts *in vivo*, we fluorescently tagged the chondrogenic and osteogenic progenitor cells in some of our grafts. To understand the maturation of our tissues during *in vitro* culture, we also studied miniaturized, cylindrical cartilage-bone constructs in the same experimental groups (cartilage-bone, bone, and acellular scaffold) and using the same methods as for the clinically

sized grafts. These smaller constructs had thicknesses corresponding to the critical distances for nutrient transport, cell migration and mechanotransduction in the larger anatomical grafts, and were designed to correspond to a core taken from the middle of the RCU condyle. To eliminate the potential biological differences in regenerative capacity of the cells, we pooled the ASCs sourced from n = 7 animals. The small constructs were grown in bioreactors using the same culture media and under the same local velocities as the anatomical grafts during perfusion culture. The assays for evaluating tissue outcomes were also the same as for the anatomical grafts.

The implantation studies were conducted using 20 skeletally mature male Yucatan minipigs between 13 and 23 months old. The sample size of $n \geq 5$ per group was determined using power analysis, with a standard deviation (SD) of 20% (based on the 10-20% SD observed in cartilage friction coefficients from our previous *in vitro* cartilage work) [96], power of 90%, difference to detect 50% of the mean average, and α of 0.05. The sample size of $n \geq 5$ per group for *in vitro* constructs was determined similarly. Specific information on sample size, data collection, and inclusion and exclusion criteria are provided for each experimental stage.

Out of the 20 animals, 19 underwent the procedure until the 6-month endpoint without apparent distress. One animal was euthanized early (1 month post-surgery) after implant displacement due to the snapping of the fixation plate. Another animal developed infection as determined from inspection by an expert maxillofacial surgeon. Although there was no frank purulence, the gross appearance of the tissue was necrotic and indicative of a chronic infection. One animal lacked the TMJ disc and synovial fluid. After exclusion of these

three animals, we analyzed the remaining 17 implanted RCUs (cartilage-bone: n = 6, bone-only: n = 8, and acellular controls: n = 3), along with the 19 native contralateral RCUs.

3.5.2 Perfusion Bioreactor Design and Operation

The perfusion bioreactors were developed starting from a previous bioreactor system that was used to generate anatomical pieces of tissue-engineered bone [94]. Additional fluidic routing conduits were designed to perfuse chondrogenic medium along the condylar surface, without mixing with the osteogenic medium introduced into the bone region, using a soft, disposable polydimethylsiloxane (PDMS; Dow Corning) manifold assembled around the graft in three sections. Two sections distributed the flow of osteogenic media throughout the graft, one at the inlet side, and one at the outlet side. These two sections were created with channels for bone perfusion whose size, placement, and number were designed to provide an optimal flow velocity (800 μm/s) throughout the graft [94,102]. The design objective was to provide adequate mass perfusion along the perfusion paths ranging from 5-7 mm (thickness of the ramus) to 25 mm (at the condylar head). The third section of the manifold transported the chondrogenic media, which was routed along flow channels from inlet to outlet on the surface of the condyle. The channels were about 0.75 mm tall, 1.0 mm wide, spaced 2.0 mm center-to-center, and were aligned in parallel to the sagittal plane. The chondrogenic cells at the surface of the graft were shielded from fluidic shear stress with a porous hydrophobic membrane (1 μm pores, Sterlitech Corp). The three PDMS manifolds were sealed against the graft by an external shell machined from polycarbonate. Peristaltic tubing from the inlet and outlet ports in each section of the bioreactor was connected to a pump and reservoir for recirculating flow.

3.5.3 Scaffold Fabrication

Large cancellous cylindrical bone cores, 4 cm in diameter and 7 cm long, were created from the distal aspect of adult bovine femurs (>2 years old animals) using a 44-mm diameter, 75-mm long hole saw (PipeMan Products, Inc.) attached to a hammer drill (Bosch). To fabricate scaffolds for the ramus-condyle unit, we segmented the anatomy of each animal from a CT scan image stack using Mimics software (Materialise, V16). This segmented volume was exported as an STL mesh and converted into Initial Graphics Exchange Specifications (IGES) format in RapidForm software (Inus, vXOR3). The IGES formatted file was then imported into Solidworks (Dassault Systems, v2017) for use in bioreactor design and scaffold fabrication. To machine the bone block, Mastercam-for-Solidworks software (CNC Software Inc, v2017) was used to generate G-code to control a 4-axis milling machine (Taig Tools). The cylindrical bone cores were milled using a 3/16 in diameter ball endmill into the custom geometry of the RCU for each animal. To fabricate the small scaffolds, the same bovine femurs were used, from which cylindrical scaffolds with a domed surface to mimic the condyle were milled. The cylindrical portion of the scaffolds were 9 mm diameter and 7.5 mm high, and the dome surface had a height of 1.5 mm with uniform curvature (based on a sphere of radius 7.5 mm).

The anatomical scaffolds and small plug scaffolds were subsequently stripped of all cellular material to leave behind the extracellular matrix with largely preserved composition, architecture, and mechanical properties using our previously established protocol [94] which removes all cellular material [128,129]. The bone was washed with high-velocity streams of water to remove the marrow from the pore spaces, and treated on an

orbital shaker in four steps to remove any remaining cellular material: (i) phosphate-buffered saline (PBS; Corning) with 0.1% EDTA (w/v) for 1 hour at room temperature; (ii) hypotonic buffer of 10 mM Tris (Sigma), 0.1% EDTA (w/v) in DI water) overnight at 4°C; (iii) detergent (10 mM Tris, 0.5% SDS (w/v; Sigma) in DI water) for 24 hours at room temperature; (iv) enzymatic solution (100 U/mL DNase, 1 U/mL RNase, 10 mM Tris in DI water; Sigma) for 6 hours at 37°C.

Decellularized bone blocks were freeze-dried, subjected to sonication treatment to remove any remaining debris, and stored in 70% ethanol (v/v) under ultraviolet light (UV) for sterilization. Prior to cell seeding, the scaffolds were washed and submerged in high-glucose Dulbecco's modified Eagle's medium (DMEM; Gibco) overnight.

3.5.4 Stromal/Stem Cell Preparation

Subcutaneous adipose tissue (about 100 mL) was harvested from the dorsal lumbar region of each animal (n = 20) under anesthesia (see the "Animal implantation" section) at the same time as the initial CT procedure, and the ASCs were isolated as previously described [130]. The cryovials containing passage 0 (P0) ASCs were verified for quality, sterility, and proliferative potential by LaCell LLC and shipped overnight on dry ice from LaCell LLC in New Orleans to Columbia University. The ASCs were expanded in high-glucose DMEM (Gibco), 10% fetal bovine serum (FBS; Corning), 1% penicillin/streptomycin (P/S; Gibco), and fibroblast growth factor (0.1 ng/mL; Peprotech) with media changes twice per week and passaged by trypsinization up to P5.

A subset of grafts (n = 10 of 20) contained ASCs that had been fluorescently tagged prior to cell expansion **(Table 3.1).** To visualize both chondrogenic and osteogenic

progenitors, we generated stably transduced ASCs at an early passage with GFP to facilitate cell tracking in the graft. The lentiviral vector plasmid pLenti CMV GFP Hygro (Addgene #17446) and auxiliary packaging plasmids pMD2.G (Addgene #12259) and pCMV-ΔR8.2 (Addgene #12263) were co-transfected into packaging HEK293T cells using polyethylenimine (PEI 25K, Polysciences). Viral supernatant was filtered 48 hours after transfection and either used immediately for transduction or stored at -80°C. For transduction, the filtered supernatant was mixed with 8 μg/mL of Polybrene and added to the ASCs. Successfully transduced ASCs were isolated by hygromycin selection (250 μg/mL).

Table 3.1. Experimental groups

Small constructs	Cartilage-bone	Bone-only	Acellular	Total
End total (5 weeks *in vitro*)	6	6	4	16
Ramus-condyle units	Cartilage-bone (GFP-tagged)	Bone-only (GFP-tagged)	Acellular	Total (GFP-tagged)
Start number	8 (4)	9 (6)	3	20 (10)
Early euthanasia		1 (1)		
Gross pathological issues	2 (1)			
End total (5 weeks *in vitro* + 6 months *in vivo*)	6 (3)	8 (5)	3	17 (8)

3.5.5 Cultivation of the Cartilage Layer

The cartilaginous layer was generated from condensed mesenchymal cell bodies (CMBs) using our previously established protocol [96]. Passage 5 ASCs were suspended in chondrogenic medium comprised of high-glucose DMEM (Gibco) supplemented with 10 ng/mL TGF-β3 (Peprotech), 100 nM dexamethasone (Sigma), 50 μg/mL ascorbic acid-2-phosphate (Sigma), 100 μg/mL sodium pyruvate (Corning), 40 μg/mL proline (Sigma), 1%

insulin, transferrin, sodium selenite (ITS+; Corning) mix, and 1% penicillin/streptomycin (P/S; Gibco). Each CMB was formed using 2.5×10^5 cells/mL based on previous experiments demonstrating the formation of compact spherical bodies measuring 1 mm in diameter [96]. Cell suspension was aliquoted into deep round-bottom 96-well plates at 1 ml per well and centrifuged at 250g for 5 minutes, and the CMBs were allowed to self-assemble over 3 days in the incubator at 37°C, 5% (v/v) CO_2 with daily media changes.

The cartilage region covering the articulating surface of the condyle was sized to 1 mm thick, corresponding to 800 CMBs per anatomical scaffold and 120 CMBs per small scaffold. The scaffold condylar surface areas determined by the SolidWorks software were 4-5 cm^2 for the anatomical scaffolds and 0.70 cm^2 for the small scaffolds. The CMBs were placed onto the polycarbonate membrane cut to match the condylar surface, in the void of the condylar PDMS block, and the decellularized scaffold was pressed onto the CMB layer.

The CMB layer was allowed 1 day to attach to the scaffold under static culture conditions, with the bioreactor oriented with the condylar end face-down. Chondrogenic media were perfused for 5 weeks over the condylar surface at a flow rate of 1 mL/min, separated from direct contact with the CMB layer by the PCTE membrane to reduce shear stress. Culture medium was changed twice per week. The total culture time was selected based on preliminary studies for the CMBs to form a cartilage layer integrated with the underlying scaffold. Osteogenic cells were introduced to the graft 2 weeks after the initial seeding of the CMB layer, by which time a compact cartilage layer has been formed.

3.5.6 Cultivation of the Bone Region

Passage-5 ASCs were suspended in osteogenic medium comprised of low-glucose DMEM (Gibco) supplemented with 10% fetal bovine serum (FBS; Corning), 1% P/S, 10 mM sodium beta-glycerophosphate (Sigma), 100 nM dexamethasone, and ascorbic acid 2-phosphate (50 μg/mL). The scaffold volumes as determined by the SolidWorks software were in the range of 9-15 cm^3 for the anatomical scaffolds and 0.53 cm^3 for the small scaffolds. Cell suspension (10^7 cells/cm^3) was infused into the bioreactor chamber, using 12 mL volume for the anatomical scaffold and 630 μL volume for the small scaffold. The cells were allowed 3 hours to attach to the scaffold under static culture conditions, and the bioreactor was flipped every 30 minutes to facilitate spatially uniform attachment throughout the scaffold volume. Osteogenic media was perfused through the construct for 3 days at 10% of the calculated optimal flow rate (80 μm/s), and for an additional 3 weeks at the set optimal flow rate (800 μm/s), with medium changes twice per week. The culture time was selected on the basis that ASCs highly express osteogenic markers after 3 weeks of *in vitro* differentiation.

3.5.7 Transportation of Engineered Grafts

The grafts were transported within their bioreactor culture chambers providing sterile containment from Columbia University (New York, NY, USA), where they were grown, to the animal facility at Louisiana State University (Baton Rouge, LA, USA), where they were implanted. Each bioreactor was aseptically disconnected from the pump and media reservoirs, and the tubing was assembled into a closed loop. The bioreactor was then packaged into a protective hard case, cushioned with foam and filled with ice packs. Upon

arrival at the animal facility, each bioreactor was aseptically reassembled by connecting the chamber to the reservoir, and maintained in a tissue culture incubator with medium perfusion until implantation (<48 hours). The total travel time was ~10 hours. In previous studies, we have shown by finite element modeling that under these conditions the minimum oxygen concentration reached was ≥0.14 mol/m^3 [94]. We verified that this oxygen concentration was sufficient for cell survival by live-dead assays before and after transportation.

3.5.8 Animal Implantation

The animal implantation study was conducted at the Louisiana State University School of Veterinary Medicine under an approved Institutional Animal Care and Use Committee protocol (14-077). A total of 20 skeletally mature Yucatan minipigs (Lonestar Laboratory Swine) were randomly assigned to three treatment groups: (i) acellular scaffold implantation (n = 3), (ii) engineered bone implantation (n = 9), and (iii) engineered cartilage and bone implantation (n = 8). Skull computed tomography scans (GE LightSpeed 16; 120 kilovolt peaks, 635-mm resolution) were performed on all animals at the time of adipose harvest, 2 to 3 months before facial surgery, to provide the scaffold fabrication data. Each animal was investigated in a longitudinal study with data collection up to 6 months after implantation.

For each animal, we used its reconstructed 3D CT images (described in the "Scaffold fabrication" section) to select the left TMJ RCU, measuring about 3 cm along the dorsal plane by 6 cm along the transverse plane, as the region for defect creation and reconstruction. Additionally, the Digital Imaging and Communications in Medicine (DICOM) data set

obtained from the preoperative CT scan was used to perform virtual surgical planning (3D Systems, Inc.). Through an online meeting between the maxillofacial surgeon and the 3D Systems, Inc engineer, the resection was mapped out on the reconstructed CT scan and surgical cutting guides were manufactured.

The grafts were grown in 3 separate experiments, with randomized division of animals into experimental groups. Grafts from the same experiment were implanted on consecutive days, with 2 to 3 surgeries performed per day. The surgical procedure was designed by an expert maxillofacial surgeon to closely mimic the current clinical procedure in human patients.

After 12 hours of fasting, animals were sedated with ketamine (3 mg/kg), tiletamine (2 mg/kg), and xylazine (3 mg/kg), administered intramuscularly. Anesthesia was then induced with 5% isoflurane (MWI) in 100% oxygen (1.5 L/min) via facial mask. The animals were intubated with a cuffed Murphy's endotracheal tube (7 to 9 mm internal diameter), and anesthesia was maintained at a vaporizer setting of 1.5% isoflurane and oxygen flow rate of 1-2 L/min in a closed circular system. The left side of the face was aseptically prepared with alternating chlorhexidine and isopropyl alcohol scrubs and draped to isolate the surgical field.

The planned retromandibular and submandibular incision was then marked about one to two centimeters below the inferior border of the mandible. After incising through skin and subcutaneous tissue, dissection continued to the inferior and posterior border of the mandible. The pterygoid-masseteric muscle sling was then sharply incised to expose the

entire lateral surface of the ramus and condyle. A retractor was placed in the sigmoid notch to reflect the flap superiorly. The medial pterygoid muscle was also elevated.

The surgical cutting guide was then placed and secured with two 1.7 mm screws of 8-10 mm length (Stryker, Inc). A reciprocating saw with saline irrigation was then used to create a vertical osteotomy from the sigmoid notch that was joined to a horizontal osteotomy. The ramus/condyle unit was then dissected free from its attachments and delivered.

The animal-specific graft was inserted and rigidly fixated with either a box plate (6 screws each side, 12 total) or two straight plates (7 screws each plate, 14 total) with 2.0 mm diameter screws (Stryker, Inc.). The incision was subsequently closed in layers using standard technique. A sterile dressing was applied and an immediate postoperative CT scan was performed prior to extubation. Animals were treated for post-op pain relief with 0.03 mg/kg buprenorphine intramuscularly every 6 hours for 24 hours after extubation, and 5 mg/kg phenylbutazone every 24 hours for 3 days.

3.5.9 Sample Harvest

Animals were sedated at least 15 min prior to euthanasia, which was conducted with an intracardiac injection of 200 mg/kg of sodium pentobarbital. Animal heads were shipped on ice to Columbia University and dissected within 24 hours of euthanasia. For each animal, the adipose and muscular tissue above the jaw on both sides was removed with a scalpel to expose the TMJ. The implanted left RCU and about 3 cm of native bone along the implant interface were removed with a reciprocating saw (Stryker, Inc). The equivalent contralateral right native ramus-condyle structure was removed similarly. 2 animals in the cartilage-bone

group were excluded after dissection revealed gross pathological issues, but the contralateral native structures were included in testing.

Macroscopic observations were recorded and the condylar head was washed and kept hydrated in PBS. The condyle was then carefully removed with a reciprocating saw along the widest plane of its base and kept in chondrogenic medium until mechanical testing. The remainder of the ramus was immediately fixed in 10% (v/v) formalin. End point analyses included histological and immunohistological evaluation and mechanical testing.

3.5.10 Histology and Immunohistochemistry

Small constructs (n = 4 acellular, 6 bone-only, 6 cartilage-bone) were analyzed at 1 day and after 5 weeks of bioreactor culture. RCUs (n = 3 acellular, 8 bone-only, 6 cartilage-bone, 19 native) were analyzed 6 months after implantation. Small constructs from bioreactor culture were fixed in 10% formalin (v/v) for 3 days, decalcified in Immunocal (StatLab) for 5 days, dehydrated in 70% ethanol (v/v), embedded in paraffin, and sliced 5 μm thick. The RCUs harvested from the animals were sectioned transversely using a reciprocating saw, where the first cut was made below the base of the condyle and subsequent ramus cuts were made approximately every 3 cm. The condyle was cut in half sagittally to expose the cartilage-subchondral bone interface. The pieces were fixed for 1 week and decalcified for 8-10 weeks. The samples were trimmed along the non-cutting faces by a scalpel to fit the embedding cassette (29 mm × 25 mm × 5 mm), dehydrated, embedded, and sliced as before. Sections at or near the articulating surface peak were chosen, and stained with H&E, Movat's pentachrome, and Masson's trichrome. Multiple sections (n = 3 bone-only, 3 cartilage-bone, 4 native samples) were stained at the same locations by

immunohistochemistry (VECTASTAIN Elite ABC Universal Kit, Peroxidase) using the following primary antibodies (Abcam) at a 1:500 dilution: for aggrecan (ab36861), BSP (ab52128), collagen I (ab34710), collagen II (ab34712), GFP (ab290), lubricin (ab28484), OPN (ab8448), OCN (ab93876), RUNX2 (ab192256), and SOX9 (ab26414). Primary rabbit antibody controls were performed to show the specificity of the antibody binding. Negative controls were stained in a similar fashion, without primary antibodies and on neighboring section slices. High magnification images (20x) were taken of entire slides using the Olympus BX61VS.

Cartilage layer thicknesses (total thickness acellular: 0.744 ± 0.255, bone-only: 0.579 ± 0.243, cartilage-bone: 0.622 ± 0.331, native: 0.422 ± 0.0799 mm; $P < 0.05$ acellular and native) were quantified based on Movat's pentachrome stain using the distance-between-lines ImageJ plugin (n = 8 bone-only, 5 cartilage-bone, 19 native). One cartilage-bone sample was excluded after a fibrous layer sheared off the condyle during friction testing. The field of view included the entire condylar cross section. Data had normal distributions across all groups for the proliferative and hypertrophic zones, while the data did not pass normality for the bone-only group in the hypertrophic zone.

3.5.11 Biochemical Assays

Cartilage biopsy punches were taken from the center of the condylar surface when possible (approximately 2 replicates per condyle 3-4mm in diameter, depending on sample surface area), and samples were blotted dry, weighed, snap frozen, and stored at -20°C. The samples were digested in 1.0 mL papain solution (≥16 U/mg, 15-30 mg/mL) at 60°C. dsDNA content was measured using the PicoGreen assay, and sulfated GAG content was measured

using the 1,9-dimethylmethylene blue dye colorimetric assay. The sample digests were then hydrolyzed at 110°C with 6 N HCl. Hydroxyproline content was determined from the hydrolysates. Content values were normalized to wet weight. GAG and OHP data passed the normality test (n = 13 bone-only, 11 cartilage-bone, 48 native), and were analyzed with one-way ANOVA test and post-hoc Tukey-Kramer's comparison test. DNA data did not pass the normality test for the bone-only and native groups; one native sample was excluded as an outlier by the method described in the "Statistical analysis" section, and analysis was carried out by nonparametric Kruskal-Wallis test and post-hoc Dunn's multiple comparison test (n = 13 bone-only, 11 cartilage-bone, 47 native).

3.5.12 Mechanical Testing

The entire fresh condylar head (as removed during explantation) was affixed at the base to an acrylic disc using cyanoacrylate. Frictional properties were determined by placing the condyle in contact against a cartilage counterface under 4.45 N load and prescribing sliding motion over a 5 mm wear track (1 mm/s, 120 cycles). Tangential and normal forces to the articular surface were recorded and used to determine the friction coefficient, which was then averaged and reported over each cycle. The sectioned condyles were stored in chondrogenic media at 4^0C when not being tested. After the mechanical tests, 3-4 mm biopsy punches were taken from the condylar surface for biochemical analysis, and the remainder of the condyle was fixed in 10% formalin.

Cartilage strips (about 10 mm by 30 mm) used as the opposing cartilage counter-face were harvested from the tibial plateaus of immature bovine knee joints (2-3 months old). Strips were placed articular surface down on the freezing stage of a sledge microtome

(Physitemp Instruments #BFS-30TC, Clifton, NJ; Leica Instruments #SM2400, Nusslock, Germany), fixed in a water-soluble embedding matrix (Thermo-Fisher Scientific #1310APD, Rockford, IL), then trimmed to remove bone and to expose a flat and even surface. Strips were rinsed in filtered PBS and either stored frozen in PBS supplemented with 0.04% isothiazolone-based biocide (Proclin 950, Sigma-Aldrich #46878-U, St. Louis, MO) and 0.1% protease inhibitor (0.05 M Ethylenediaminetetraacetic acid, EDTA) at -20 ˚C or immediately mounted for testing.

Frictional tests were performed using two identical custom testing devices [131]. Devices were controlled with custom LabVIEW software (National Instruments Corporation LabVIEW 2010, Austin, TX) and motion controllers (National Instruments Corporation #7354, Austin, TX), which provided continuous measurements of displacements, applied loads, and reaction loads. The two-axis loading devices provided translational motion which produced sliding between the engineered or native cartilage and cartilage strip counterface. Testing devices were each equipped with a six-axis load cell (JR3 Inc. #20E12A4, Woodland, CA) mounted on a horizontal translation stage (JMAR xy motorized linear stage) driven by a stepper motor (Oriental Motor, Vexta line #PK266-03B). Two linear encoders (RSF Electronics MSA 65x series, 5-10 μm resolution; Renishaw #T1031-30A) recorded the horizontal (U_x) and vertical displacements (U_y). Sliding motion was prescribed at 1 mm/s over a wear track of total length of U_x = 5 mm for a total testing duration of 20 minutes (120 cycles) under 4.45 N load. Loads were applied manually by placing known weights on the vertical translation stage.

Cartilage strip counter-faces were immersed in a bovine synovial fluid bath (Animal Technologies, Inc.) and mounted on top of the load cell and horizontal translation stage. Synovial fluid underwent centrifugation (1500 g, 10 minutes) prior to frictional testing to remove particulates and debris. The strip was aligned in the direction of translational motion. Condyles were mounted on the horizontal translation stage and brought into contact with the articular surface of the cartilage strip. The forces tangential (F_t) and normal (F_n) to the articular surface were recorded and used to calculate the pointwise friction coefficient at each position U_x by using $\mu = (F_{+t} - F_{-t})/(F_{+n} + F_{-n})$, where + and – refer to the force values at the forward and reverse strokes of each cycle. The friction coefficient was averaged over each cycle and the mean of all cycle-averaged values through the entire test duration was calculated.

For the small constructs (n = 4 acellular, 6 bone-only, 6 cartilage-bone), all data were normally distributed and used for analysis. For RCUs, one cartilage-bone sample had a fibrous layer on the condyle that sheared off and was therefore excluded from these results, and one native sample was found to be an outlier by the method described in the "Statistical analysis" section, and was excluded, leaving n = 8 bone-only, 5 cartilage-bone, and 18 native samples, all of which were normally distributed.

3.5.13 Statistical Analysis

Statistical analysis was conducted using GraphPad Prism 8 software (GraphPad Software Inc.). Data for cartilage thickness, biochemical content, and friction coefficient were checked for whether they fit Gaussian distributions using the Shapiro-Wilk normality test. When normality was confirmed, statistical analysis was carried out by one-way ANOVA test

and post-hoc Tukey-Kramer's comparison test to compare means between groups (biochemical content, friction coefficient). When normality was not confirmed, or when sample size was <4, statistical analysis was carried out by nonparametric Kruskal-Wallis test and post-hoc Dunn's multiple comparison test to compare the means between groups (cartilage thickness). Native data, which were expected to be normally distributed, were checked for outliers using the Robust regression and Outlier removal (ROUT) method and a Q coefficient of 1% to limit the false discovery rate [132]. Specific information on sample size, data collection, and inclusion and exclusion details are provided in the context of each experimental stage. Data were calculated as means ± SD. $P < 0.05$ was considered significant.

Chapter 4: Aim 2

Develop an optogenetic human iPSC-based system for TGF-β mediated 3D chondrogenic differentiation

The contents of Chapter 4 are based on the following publication:

Wu JY, Yeager K, Soni RK, Hung CT, Vunjak-Novakovic G. Directed differentiation of human iPSCs into mesenchymal lineages by optogenetic control of TGF-β signaling. Manuscript in review.

Transforming growth factor (TGF)-β signaling modulates key mesenchymal stem/stromal cell (MSC) functions including proliferation, immunomodulation, and multilineage differentiation. Despite abundant studies of the effects of TGF-β signaling in MSCs and their progeny, translational potential remains limited. In tissue development and homeostasis, TGF-β signaling is finely coordinated by latent forms and matrix sequestration, while in vitro studies are inherently imprecise due to the variability of both soluble regulatory factors and cell sources. Optogenetics can offer unprecedented precision and dynamic control of cell signaling with light. We report the development of an optogenetic human induced pluripotent stem cell (hiPSC) based system for TGF-β signaling and demonstrate its utility in directing TGF-β mediated mesenchymal differentiation into the smooth muscle and tenogenic lineages in monolayers, and the chondrogenic lineage in hydrogels. Across the three mesenchymal lineages studied, groups which received light-activated TGF-β signaling had expression levels of differentiation markers closer to the soluble factor treated conditions than to the untreated controls, with minimal phototoxicity

over multiple weeks of light stimulation. This system for optogenetic regulation of TGF-β signaling in hiPSCs can enable future versatile, patient-specific, and spatiotemporally precise studies of cellular decision making and fate.

4.1 Introduction

TGF-β signaling is critical to healthy development and homeostasis, while aberrant signaling has been implicated in pathological conditions such as Marfan syndrome, the related Loeys-Dietz syndrome, various cancers, and fibrosis [133]. TGF-β is known to direct nearly every aspect of MSC function, including proliferation, immunomodulation, and multilineage differentiation [134]. The regulation of TGF-β signaling is important for a number of organ systems, and as a result, the TGF-β family has been investigated for therapeutic targeting in stem cells and regenerative medicine.

In cell-based cartilage tissue engineering, TGF-β is one of the most widely used mediators to drive chondrogenesis and promote tissue growth [8]. In particular, spatiotemporal gradients of TGF-β signaling are critical to the development of stratified native-like cartilage. Cartilage tissue constructs formed from human bone marrow derived MSCs under spatiotemporal regulation of TGF-β signaling mimicking native gradients demonstrated improved *in vivo* stability compared to their isotropic control counterparts, resisting endochondral ossification and retaining physiologic stratified organization [54]. In juvenile bovine chondrocytes, brief rather than sustained exposure to TGF-β at lower concentrations than the typically applied supraphysiological dose of 10 ng/mL was sufficient for robust cartilage tissue formation [8,52,53]. Other studies that used integrated experimental and computational approaches have shown that TGF-β stimulation can induce

short-term graded responses (*Smad7* gene expression), which evolved into long-term switch-like responses (growth inhibition) [135].

Despite abundant studies of the effects of TGF-β signaling in MSCs and their progeny, most stem cell differentiation protocols continue to use a standardized regimen of 10 ng/mL soluble TGF-β with media changes every 3-4 days throughout the entire culture duration [54,136,137]. Translational potential also remains limited, in large part due to variability of both soluble regulatory factors (batch variability, culture stability, spatiotemporal imprecision) and cell sources (non-autologous, with a range of donor ages, tissue origins, and disease states).

In physiological studies *in vivo*, TGF-β signaling is elegantly coordinated by latent forms and matrix sequestration [52], while the maintenance of gradients of factors *in vitro* is inherently imprecise. This has been well-documented for recombinant basic fibroblast growth factor (bFGF or FGF2), a comparable regulatory protein which maintains the self-renewal and undifferentiated state of human pluripotent stem cells. Standard stem cell maintenance methods require daily culture medium replacement to replenish the growth factors. However, FGF2 concentration decreased to 40% of supplemented levels after only 4 hours, and to 10% after 24 hours [138]. Based on these findings, other investigators developed thermostable chimeric variants that enable every other day medium changes with sustained, rather than dramatically fluctuating, FGF concentration profiles [139,140].

Additional efforts were directed towards developing more precise tools for manipulating TGF-β signaling, such as chimeric receptors [89], synthetic ligand-presenting surfaces [141], infrared light-released ligands in carbon nanotubes [142], inhibitors of

receptor kinase activity [143], or ligand-binding inhibitors [144]. Unfortunately, chemical tools cannot exert the finer levels of spatiotemporal resolution necessary to better understand and mimic physiologic TGF-β signaling. In particular, maintenance of a chemically-based gradient becomes challenging and cumbersome in complex settings such as diffusion-limited tissue constructs or organs-on-chip systems with perfusion.

Optogenetics provides a means for inducing cell physiology by light stimulation, offering unprecedented precision and dynamic control of cell signaling in space and time [145]. The photoactivatable proteins driving light responsiveness show rapid reversibility, and spatial patterning by photomasks in optogenetic cell monolayers with resolution on the scale of 100 μm has been demonstrated [146]. To date, optogenetics has been used to interrogate major pathways such as FGF or Wnt/β-catenin, largely in monolayers of immortalized cell lines, and only more recently in pluripotent stem cells [147–149]. Human induced pluripotent stem cells (hiPSCs) can be derived in a minimally invasive and patient-specific manner and are enabling personalized studies of injury, diseases, and therapies.

Our goal was to develop hiPSC-derived MSCs capable of optogenetic TGF-β signaling (optohiMSCs), and to show that light can be used in lieu of soluble growth factor to drive TGF-β mediated multilineage mesenchymal differentiation, including chondrogenic differentiation in three-dimensional (3D) culture. We anticipate that the optogenetically edited cells can serve as a versatile tool for studying and exploiting TGF-β signaling in MSCs.

4.2 Results

4.2.1 Study Design

Our objective was to establish a hiPSC based system that would allow the use of light to control TGF-β signaling. We hypothesized that we can stably introduce optogenetic TGF-β receptors into hiPSCs without functional detriment, and that light can be used to recapitulate the role of soluble TGF-β in various mesenchymal differentiations **(Figure 4.1A).**

We started by generating clonal hiPSC populations with optogenetic receptors that could activate TGF-β signaling in response to blue light. Canonical TGF-β signaling is initiated at the cell surface when TGF-β binds the transmembrane TGF-β type I and type II receptors (TGFBR1, TGFBR2) **(Figure 4.1B)**. The resulting cascade of phosphorylation events leads to the nuclear localization of a Smad complex that regulates gene expression [150]. In the light-inducible system previously developed by Li et al. [11], signaling was mediated by the blue light activation of *Arabidopsis thaliana* protein interactions between the truncated N-terminal end of cryptochrome-interacting basic helix-loop-helix 1 (CIBN) and cryptochrome 2 (CRY2), with each protein being coupled to a receptor. The optogenetic TGFBR1 (optoTGFBR1) was comprised of a myristoylation signal peptide (Myr) tether to the plasma membrane, the intracellular region of native TGFBR1, and CIBN; the optogenetic TGFBR2 (optoTGFBR2) was comprised of the intracellular region of native TGFBR2, CRY2, and a tdTomato fluorescent tag **(Figure 4.1C)**.

The subsequent generation of optogenetic hiPSC-derived MSCs (optohiMSCs) served two main purposes. First, it provided functional validation that the introduction of the

optogenetic system into hiPSCs did not affect their ability to differentiate into other cell types. Second, the optohiMSCs were the starting point for downstream differentiations into smooth muscle, tenogenic, and chondrogenic lineages. TGF-β is known to be a potent regulator in differentiations of MSCs, and the transcription factors through which it acts have been identified [134].

MSC differentiations span a range of complexity, where the derivation of smooth muscle cells largely depends on TGF-β and stiff substrate [136], tenocytes require stepwise supplementation with additional growth factors beyond TGF-β [137], and chondrocytes need to be cultured in 3D settings [50]. For each differentiation, we compared groups which received no soluble or optogenetic TGF-β stimulation (-T), soluble TGF-β3 alone (+T), or optogenetic stimulation alone at two intensities of light (+L3 or +L6), keeping all other culture conditions the same. The effects of TGF-β signaling on these MSC differentiations, assessed by qRT-PCR, immunostaining, and global quantitative proteomics, were used to demonstrate that light-activated TGF-β signaling could drive biologically meaningful responses beyond the previous upstream characterization of optogenetic receptor behavior [11].

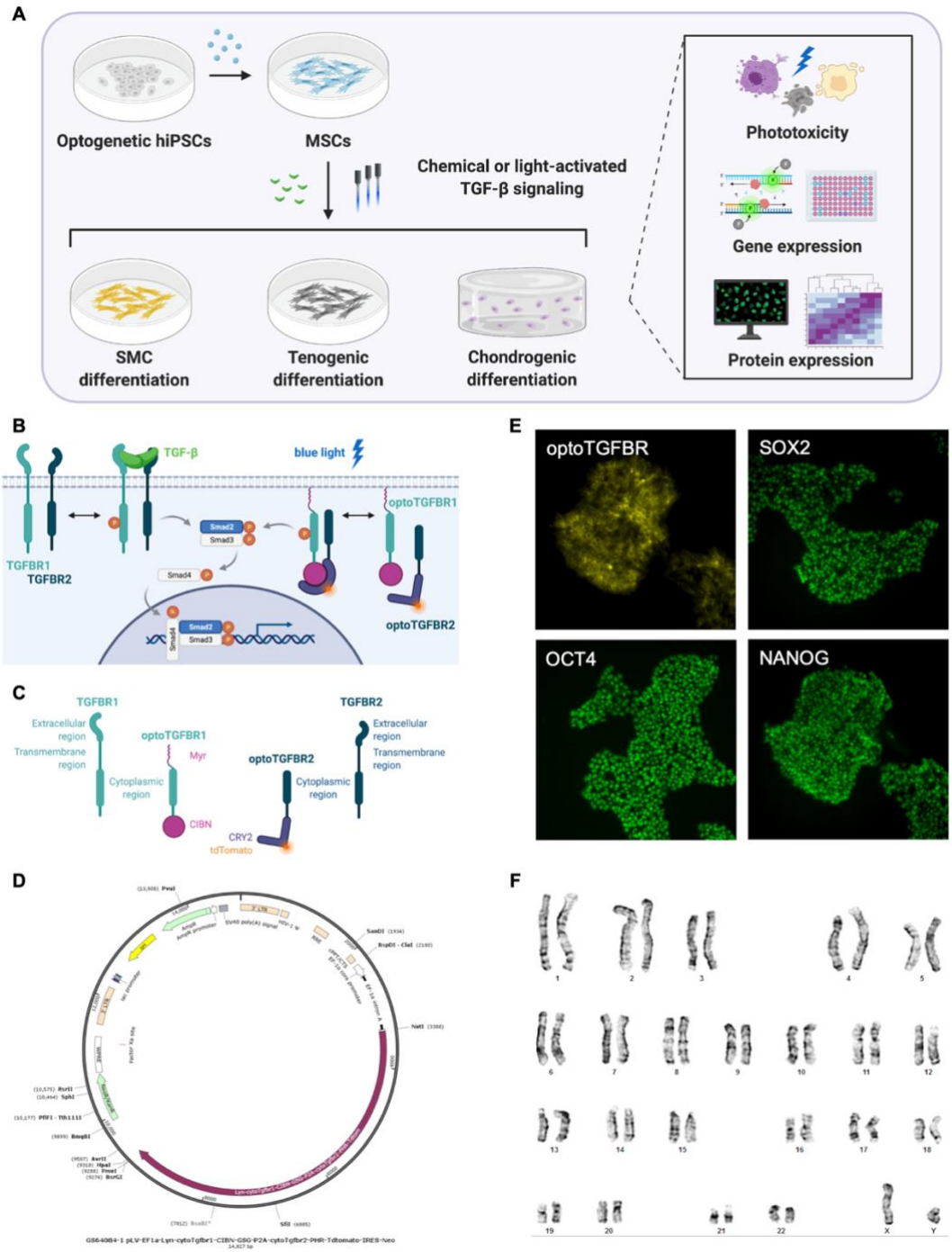

Figure 4.1. hiPSC-based system for optogenetic TGF-β signaling. (A) Study design. **(B)** Canonical TGF-β signaling pathway via soluble factor-activated endogenous TGF-β receptors (TGFBRs) or blue light-activated optogenetic (opto) TGFBRs. **(C)** Endogenous TGFBRs and optoTGFBRs share the same cytoplasmic regions. **(D)** Lentiviral vector containing optoTGFBRs. **(E)** tdTomato-tagged optoTGFBRs and immunofluorescently stained pluripotency markers in clonal population of optogenetic hiPSCs. **(F)** Karyotype of optogenetic hiPSCs.

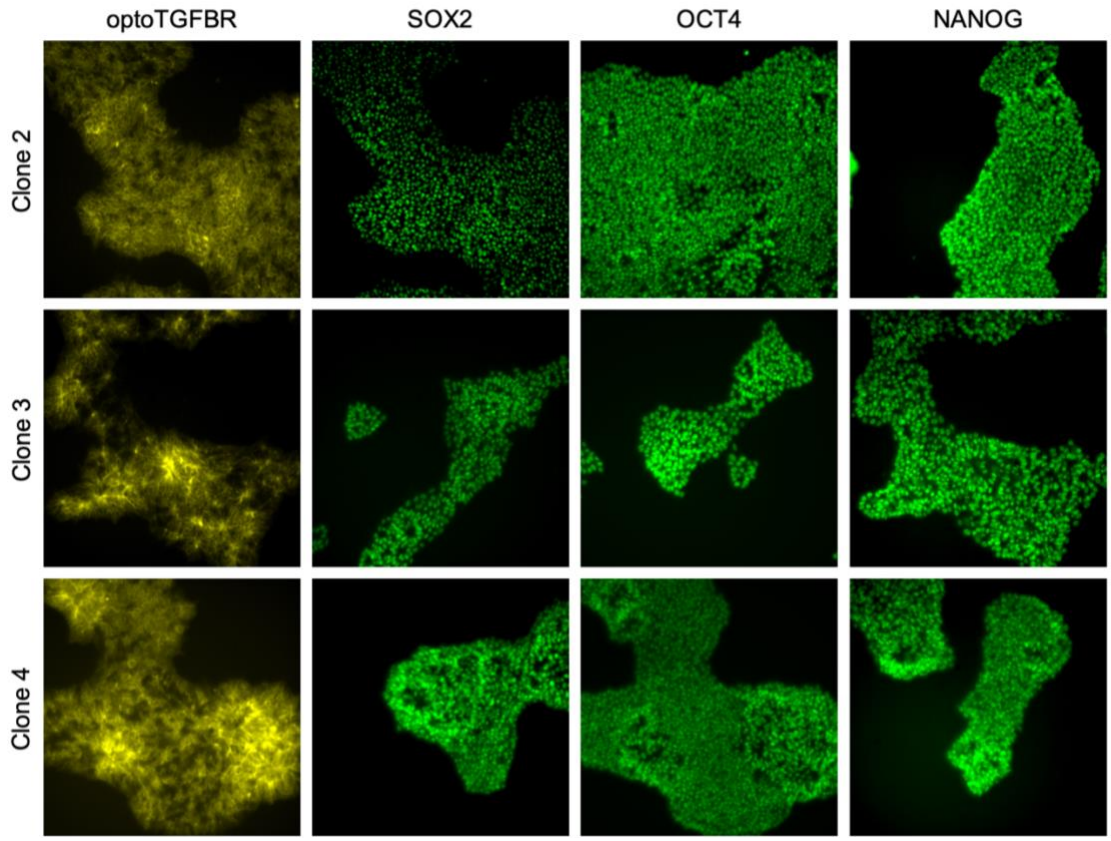

Figure 4.2. Additional characterization of clonally derived optohiPSCs. Expression of tdTomato-optoTGFBRs and immunofluorescently stained pluripotency markers.

4.2.2 Generation of hiPSC Lines Allowing Optogenetic Control of TGF-β Signaling

Prior reports had developed optogenetic TGF-β receptors and characterized light activated signaling in the immortalized and highly durable HeLa cell line [11]. Here we established the optogenetic system for use in hiPSCs via lentiviral transduction, suitable for both dividing and non-dividing cells without causing tumorigenic effects. To this end, we developed a single construct containing the two optoTGFBRs with the human elongation factor (EF)-1α promoter, in order to achieve the constitutive and long-term expression **(Figure 4.1D)** [151]. The resulting hiPSC lines were stable and had capability for light activation of TGF-β signaling (optohiPSCs). In clonally expanded populations, optohiPSCs

robustly expressed the tdTomato-tagged optogenetic system, maintained their pluripotency, and featured a normal karyotype **(Figure 4.1E, 4.1F, 4.2).**

4.2.3 MSCs Derived from optohiPSCs Maintain Phenotype and Light Responsiveness

Following mesenchymal differentiation, the optohiPSC-derived MSCs (optohiMSCs) adhered to uncoated standard tissue culture plastic with elongated morphology while maintaining high expression of optogenetic receptors, with over 70% tdTomato-positive cells as quantified by flow cytometry **(Figure 4.3A).** Further flow analysis showed high expression of mesenchymal markers CD73, CD90, and CD105 with low expression of lineage markers CD45, CD34, CD14, CD79a, HLA-DR, gated based on isotype controls **(Figure 4.3B).** Importantly, mesenchymal cell surface marker expression was similar between optogenetic and non-optogenetic hiMSCs. Both cell populations had a different CD105 profile than human bone-marrow derived MSCs **(Figure 4.4).**

Compared to wild type hiPSC-derived MSCs, optohiMSCs demonstrated similar capacity for tri-differentiation into adipogenic, osteogenic, and chondrogenic lineages, as evidenced by immunostaining for respective markers of fatty acid binding protein 4 (FABP4), alkaline phosphatase (ALP), and aggrecan **(Figure 4.3C).** These data satisfy the criteria for validating MSC phenotype [62]. Using an antibody recognizing the extracellular region of TGFBR1, a region which was not included in optoTGFBR1, Western blotting showed similar expression levels of the soluble factor-activated endogenous receptors in non-optogenetic and optogenetic hiMSCs **(Figure 4.5).**

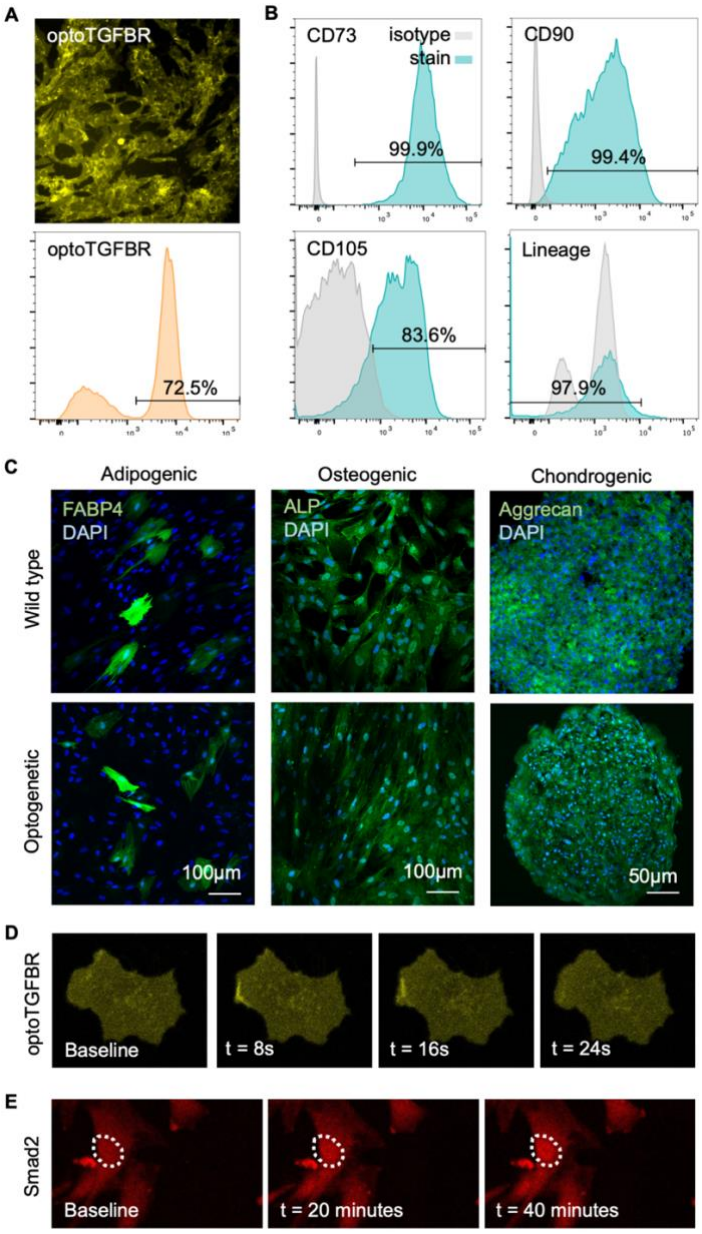

Figure 4.3. Characterization of optohiMSCs. (A) optohiMSC morphology on standard tissue culture plastic and tdTomato-optoTGFBR expression. **(B)** Flow analysis for mesenchymal CD73, CD90, CD105 and lineage markers (CD45, CD34, CD14, CD79a, HLA-DR). **(C)** Tri-differentiation of wild type hiMSCs and optohiMSCs into adipogenic, osteogenic, and chondrogenic lineages. **(D)** Plasma membrane localization of tdTomato-optoTGFBR2. *Left*: baseline, after 3 minutes of imaging without stimulation. *Middle left:* following a 1-second pulse of 488nm confocal laser, response after 8 seconds; *middle right:* 16 seconds; *right:* 24 seconds. **(E)** Nuclear localization of iRFP682-tagged Smad2. *Left*: baseline, after 3 minutes of imaging without stimulation. *Middle*: following repeated cycles of 488nm confocal laser stimulation (15 seconds) and imaging (30 seconds), response after 20 minutes; *right*: 40 minutes.

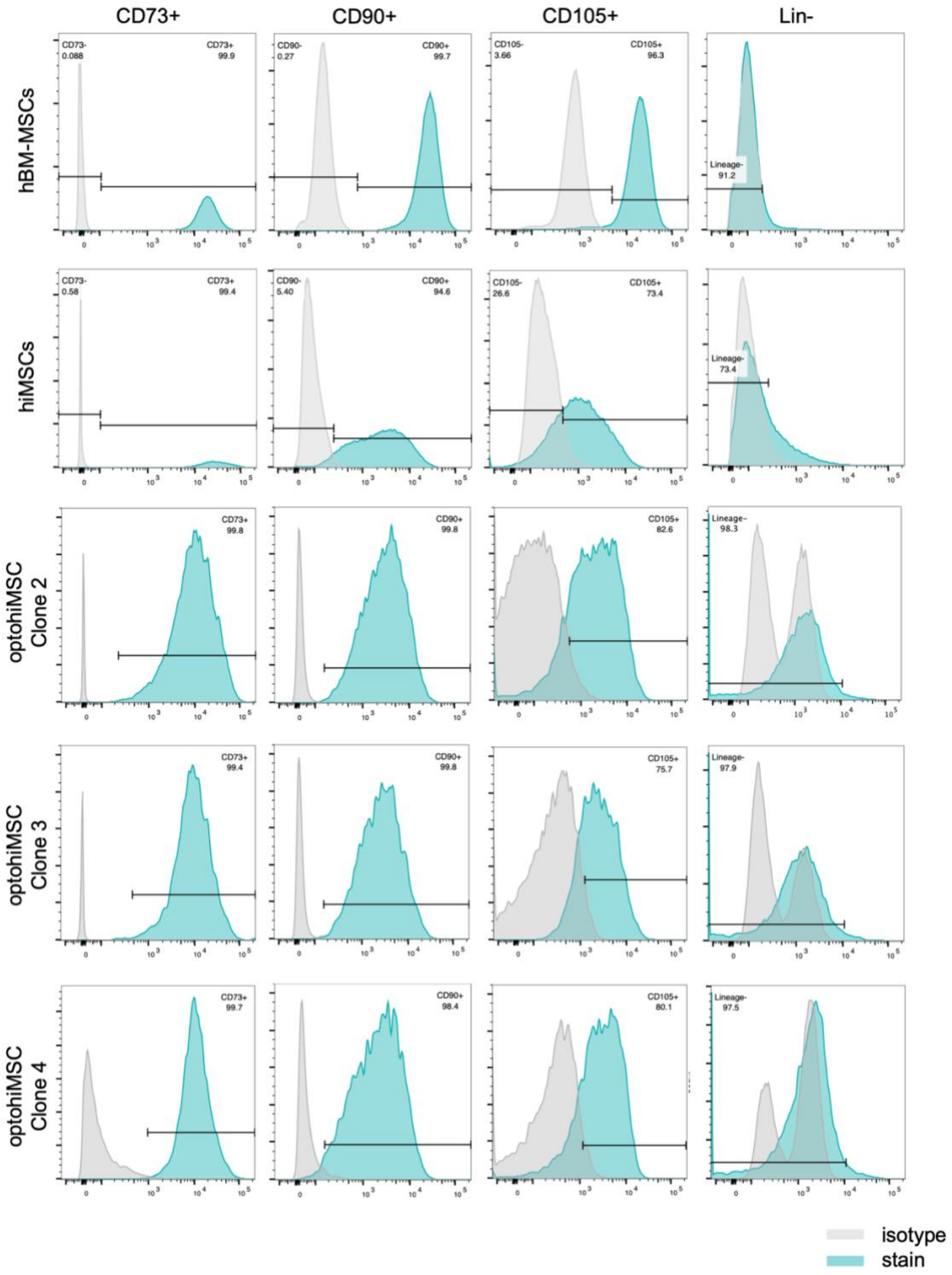

Figure 4.4. Additional characterization of clonally derived optohiMSCs. Flow analysis for mesenchymal CD73, CD90, CD105 and lineage markers (CD45, CD34, CD14, CD79a, HLA-DR).

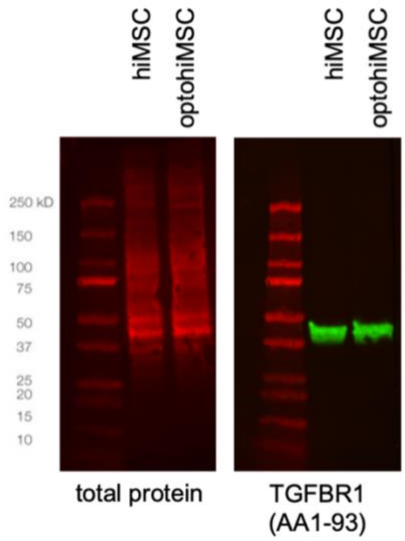

Figure 4.5. Endogenous TGFBR expression. Western blot targeting the extracellular region of TGFBR1 in hiMSCs and optohiMSCs.

Without light activation, optoTGFBR1 was tethered to the plasma membrane while optoTGFBR2, and thus the tdTomato fluorescent signal, was diffuse in the cytoplasm **(Figure 4.3D)**. Upon activation with blue light, the interaction between optoTGFBRs resulted in recruitment of optoTGFBR2 to the plasma membrane, with localized increase in tdTomato signal that was initially observed. The optoTGFBRs subsequently dissociated and tdTomato signal dissipated approximately 30 seconds after initial activation, similar to prior reports for an immortalized cancer cell line [11]. The downstream response of light-activated TGF-β signaling was expected to be the same as ligand-activated canonical signaling with respect to Smad phosphorylation and nuclear localization. In optohiMSCs transduced with iRFP682-tagged Smad2, nuclear translocation was observable about 20 minutes after light stimulation, with a stronger nuclear signal by 40 minutes **(Figure 4.3E).**

4.2.4 Derivation of the Smooth Muscle Lineage from optohiMSCs

To demonstrate that light could be used to drive cell differentiation beyond upstream TGF-β signaling pathway responses such as receptor clustering or Smad complex nuclear localization, we first used our optogenetic TGF-β system to recapitulate smooth muscle differentiation [136]. It is known that TGF-β/Smad2 signaling induces the differentiation of MSCs into smooth muscle cells *in vitro* [152].

Monolayers of optohiMSCs were allowed to reach 70-80% confluency in black-walled, cover glass-bottomed 24-well plates before they were switched to basal smooth muscle induction medium consisting of high glucose DMEM (hgDMEM), low fetal bovine serum (FBS, 5%), and penicillin-streptomycin (P/S, 1%), with no soluble TGF-β or optogenetic stimulation, with soluble TGF-β3 alone (10 ng/mL), or with 488nm optogenetic stimulation alone (3 or 6 μW/1.9 cm^2, 5-minute pulses every 2 hours) over 2 weeks total **(Figure 4.6A).** We verified with a HEK293 cell-based reporter assay that the serum did not contain detectable levels of TGF-β **(Figure 4.7)**.

Based on designs reported by Bugaj and Lim [153], we built a light stimulation device compatible with long-term incubator culture, readily adaptable for any well plate format, consisting of 192 individually programmable blue LEDs, with limited spillover between wells to allow for parallel experiments. The light stimulation regimen (intensity and timing) was selected to drive differentiations while minimizing potential phototoxic effects [11,147,148]. On the light stimulation device, the 3 μW/well group could be calibrated ±1 μW and the 6 μW/well group could be calibrated ±0.6 μW **(Figure 4.8).**

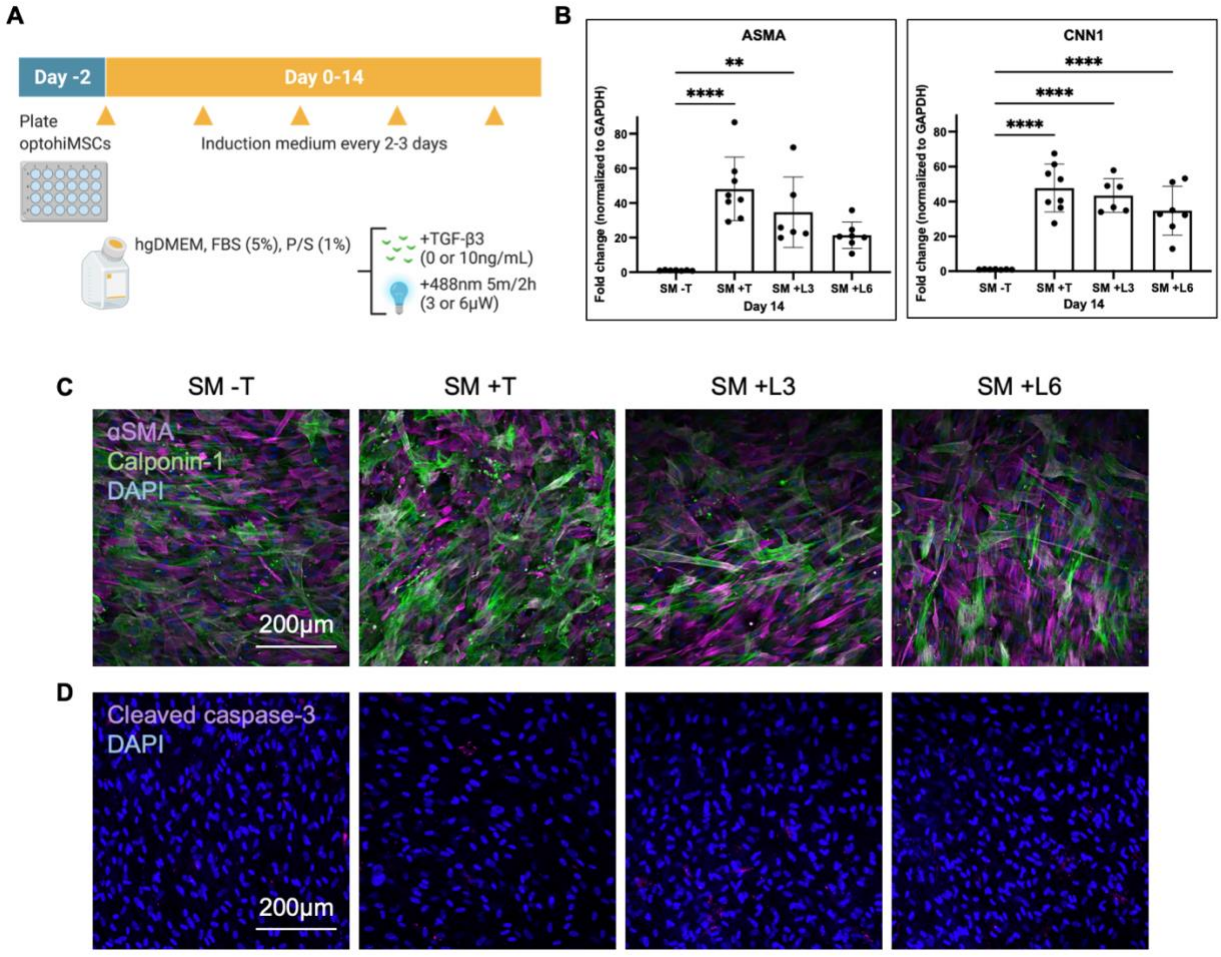

Figure 4.6. TGF-β mediated smooth muscle differentiation. (A) optohiMSCs were plated in monolayers on black-walled 24-well plates and allowed to reach 70-80% confluency over 2 days. They were then switched to basal smooth muscle medium (SM) with either no TGF-β (-T), 10ng/mL TGF-β3 (+T), 3 or 6 μW 488 nm light with 5 min pulses every 2 hours (+L3, +L6) for 14 days total. **(B)** qRT-PCR for α smooth muscle actin (ASMA) and calponin-1 (CNN1). Data are means ± SD ($n \geq 6$). **$P < 0.01$, ****$P < 0.0001$. **(C)** Immunofluorescent staining for α smooth muscle actin (purple), calponin-1 (green), and DAPI (blue). **(D)** Immunofluorescent staining for cleaved caspase-3 (purple) and DAPI (blue).

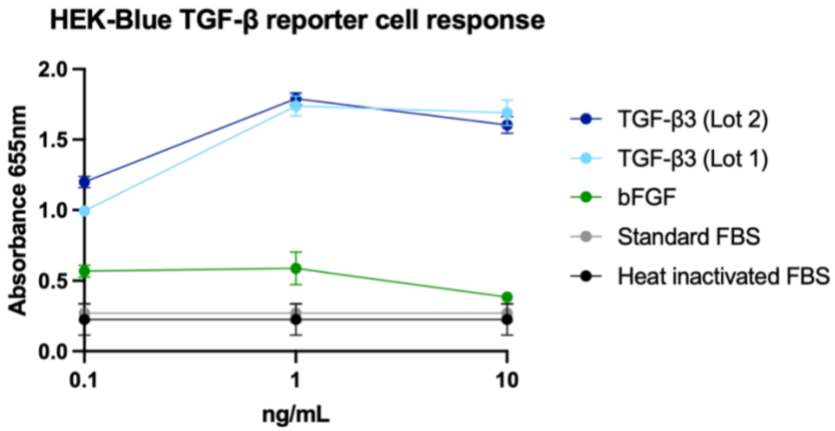

Figure 4.7. HEK-Blue TGF-β reporter assay. Secreted embryonic alkaline phosphatase (SEAP)-based assay for detecting levels of active TGF-β.

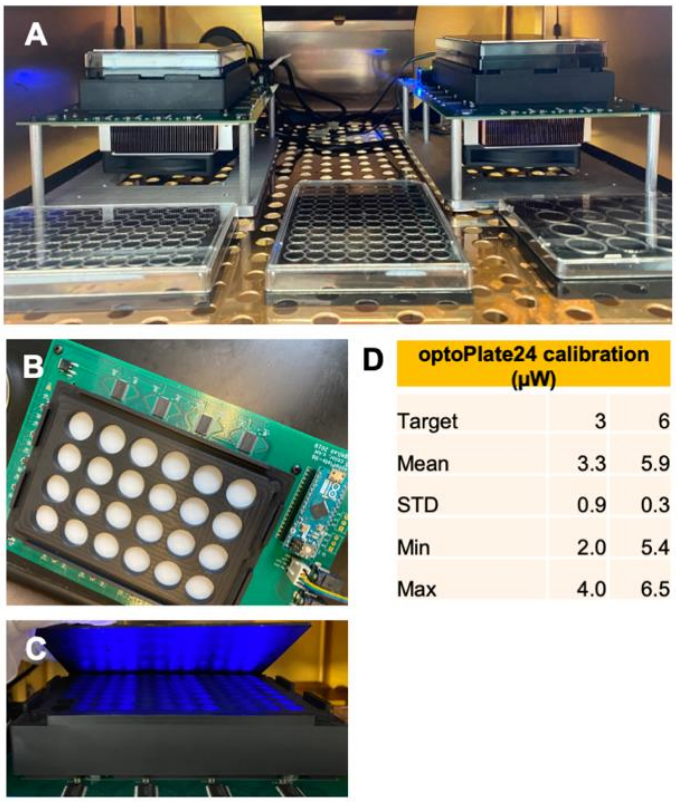

Figure 4.8. Optogenetic stimulation device. (A) Device is compatible for long-term use inside cell culture incubator. **(B)** 24-well plate format with diffusers within an adapter to distribute light evenly across each well. **(C)** 96-well plate format showing individually programmable blue LEDs and black plate lid cover to prevent light spillover between wells. **(D)** Calibration of 24-well plate format to 3 and 6 μW groups.

Contractile proteins such as alpha smooth muscle actin and calponin-1 are commonly used to assess smooth muscle cell phenotype [152]. Expression of these smooth muscle differentiation markers was evaluated by qRT-PCR and immunostaining at day 14. Gene expression of alpha smooth muscle actin (ASMA) normalized to GAPDH was significantly upregulated in groups that had received either soluble TGF-β (48-fold, $P<0.0001$) or optogenetic stimulation of TGF-β at 3 μW/well (35-fold, $P<0.01$), compared to the group that received no stimulation **(Figure 4.6B).** ASMA expression was also elevated in the group which received optogenetic stimulation at 6 μW/well (21-fold). In all TGF-β stimulated groups, calponin-1 (CNN1) mRNA expression was significantly upregulated (+T 36-fold, +L3 43-fold, +L6 35-fold; all $P<0.0001$) as compared to the negative control **(Figure 4.6B).** These results were corroborated by immunostaining for the same markers **(Figure 4.6C).** Additional immunostaining for apoptosis marker cleaved caspase-3 showed minimal phototoxicity after 2 weeks of optogenetic stimulation **(Figure 4.6D)**.

4.2.5 Derivation of the Tenogenic Lineage from optohiMSCs

TGF-β is also a critical factor in the tenogenic differentiation of MSCs, with high potency of TGF-β alone and enhanced effects when applied in combination with other growth factors [137,154]. We sought to recapitulate the tenogenic differentiation of MSCs using light stimulation, following stepwise supplementation with other tenogenic factors and TGF-β. We used the same basal medium consisting of hgDMEM, FBS (5%), and P/S (1%) but supplemented with ascorbic acid (50 μg/mL), growth/differentiation factor-7 (GDF-7/BMP-12; 100 ng/mL), and after 3 days, connective tissue growth factor (CTGF; 100 ng/mL) [137]. Monolayers of optohiMSCs were plated on 24-well plates and groups received

either no soluble TGF-β or optogenetic stimulation, or soluble TGF-β3 alone (10 ng/mL), or optogenetic stimulation alone (3 or 6 μW/1.9 cm^2, 5-minute pulses every 2 hours) over 2 weeks total **(Figure 4.9A).**

Similarly, we evaluated gene and protein expression of tenogenic markers after 14 days of differentiation. Scleraxis, a transcription factor known to be activated by TGF-β in MSCs in tenogenesis can serve as an early marker of tendon progenitors throughout tendon development [155]. Compared to the group which had neither endogenous nor optogenetic TGF-β signaling activated, gene expression of scleraxis (SCX) normalized to GAPDH was upregulated in all groups (+T 18-fold, +L3 8-fold, +L6 6-fold) and most significantly in soluble TGF-β and 3 μW/well conditions (+T $P<0.0001$, +L3 $P<0.05$) **(Figure 4.9B).** Gene expression levels of collagen I (COL1A1) normalized to GAPDH were significantly increased in all groups which had TGF-β signaling activated by soluble factor (+T 5-fold, +L3 4-fold, +L6 3-fold; all $P<0.0001$) over the negative control **(Figure 4.9B)**, suggesting maturation of tendon matrix [155]. Immunostaining for scleraxis and collagen I showed similar trends consistent with the qRT-PCR data **(Figure 4.9C).**

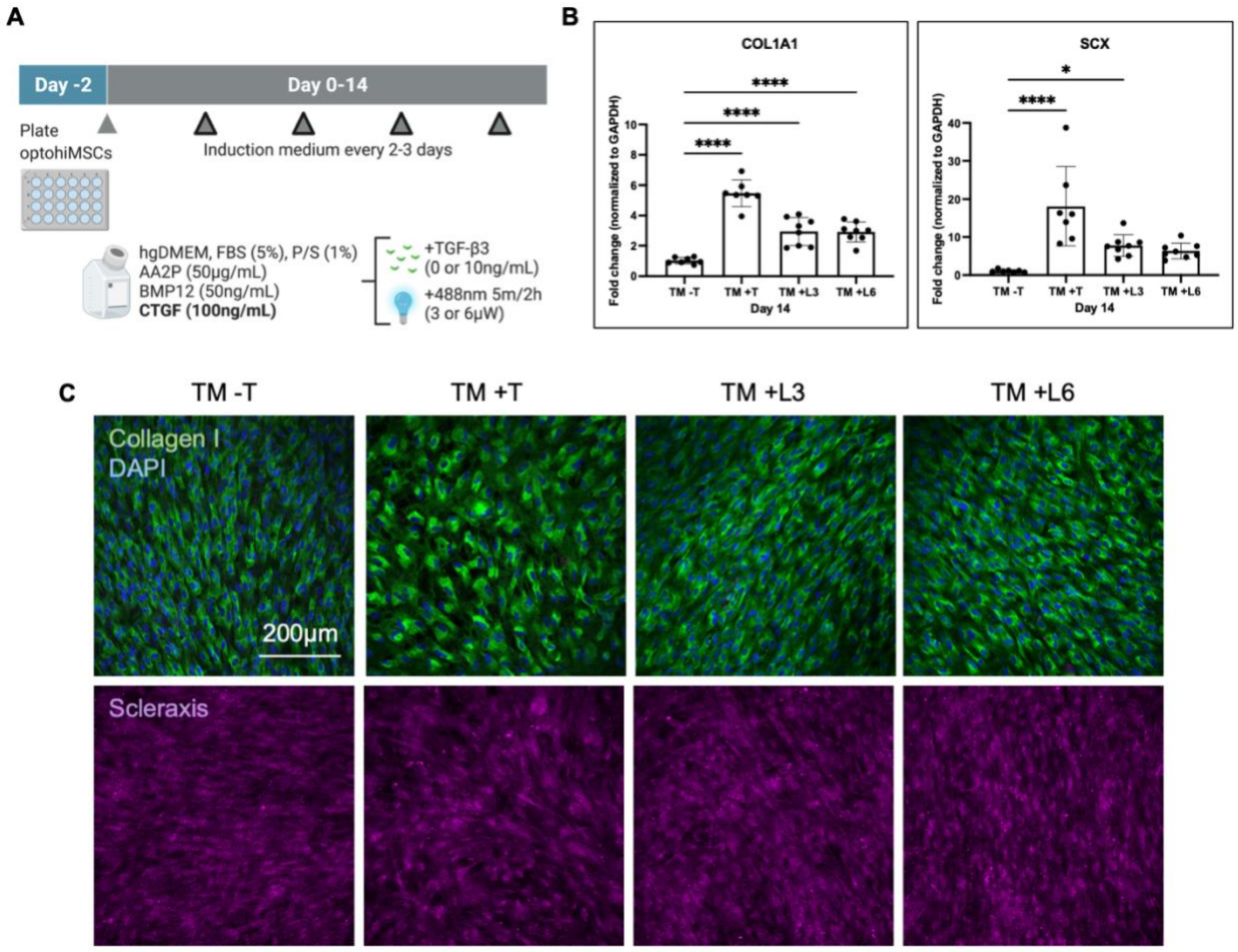

Figure 4.9. TGF-β mediated tenogenic differentiation. (A) optohiMSCs were plated in monolayers on black-walled 24-well plates and allowed to reach 70-80% confluency over 2 days. They were then switched to basal tenogenic medium (TM) with either no TGF-β (-T), 10ng/mL TGF-β3 (+T), 3 or 6 µW 488 nm light with 5 min pulses every 2 hours (+L3, +L6) for 14 days total. **(B)** qRT-PCR for collagen I (COL1A1) and scleraxis (SCX). Data are means ± SD ($n \geq 7$). *$P < 0.05$, ****$P < 0.0001$. **(C)** Immunofluorescent staining for collagen I (green), DAPI (blue), and scleraxis (purple).

4.2.6 Derivation of the Chondrogenic Lineage from optohiMSCs

In MSC-based cartilage tissue engineering, TGF-β is one of the most widely used mediators to drive chondrogenesis and promote tissue growth, acting through SRY-box transcription factor 9 (SOX9) [8]. It is also known that chondrogenic potential is greatly enhanced under 3D culture settings [50]. Thus, for chondrogenic studies of optogenetically activated TGF-β signaling, optohiMSCs were encapsulated in hydrogel (20×10^6 cells/mL in 2% agarose hydrogel, **Figure 4.10A)**. The hydrogel discs were 6-mm in diameter and 1.5-mm thick, to fit into the 96-well plate format of the optogenetic stimulation device.

Two days following encapsulation, the hydrogels were switched to chondrogenic medium consisting of hgDMEM, P/S (1%), insulin-transferrin-selenium mix (1%), HEPES (10 mM), sodium pyruvate (0.9 mM), dexamethasone (100 nM), L-proline (50 μg/mL), and ascorbic acid (50 μg/mL) [54]. Groups received no soluble TGF-β or optogenetic stimulation, soluble TGF-β3 alone (10 ng/mL), or optogenetic stimulation alone (3 or 6 μW/0.32 cm^2, 5-minute pulses every 2 hours) over 3 weeks total **(Figure 4.10B)**.

After 21 days of differentiation, we performed global quantitative proteomics on samples from two independent experiments, with n=3 replicates per group. A heat map with hierarchical clustering of samples based on relative protein expression was generated. At the highest level, samples from the same experiment were more related to each other than to samples from another experiment **(Figure 4.10C).** Within both experiments, groups that received optogenetic stimulation (+L3, +L6) had protein expression profiles more similar to those in the soluble TGF-β3 treated positive control group (+T) than to the untreated negative control group which received neither soluble nor optogenetic TGF-β stimulation (-

T), though the light stimulated groups had expression profiles more similar to each other than the soluble TGF-β3 treated group.

Comparing the positive and negative control groups (+T/-T), we identified significantly changed proteins with the absolute $\log_2$ fold change (FC) > 0.58 and false discovery rate Q < 0.05 **(Figure 4.10D).** As expected, significantly increased protein expression of TGF-β3 was detected in the soluble factor treated group (+T), with $\log_2$FC > 2 compared to all other groups (-T, +L3, +L6).

Compared to the untreated group (-T), all soluble TGF-β and light stimulated groups (+T, +L3, +L6) had significantly upregulated expression of calcium/calmodulin-dependent protein kinase kinase 1 (CAMKK1). CAMKK1 has been linked to pathways including sulfation of chondroitin, cartilage formation, and TGF-β signaling, and it is thought to be upregulated when the highly anti-chondrogenic hsa-miR-221 is inhibited [156].

Compared to the untreated group (-T), soluble TGF-β and 3μW light treated groups (+T, +L3) had significantly upregulated expression of protein mago nashi homolog (MAGOH), one of three core components in the exon junction complex interacting with SOX9, a critical transcription factor for cartilage development and homeostasis [157]. Studies have also shown that knockdown of MAGOH had similar effects on gene splicing as depletion of SOX9 itself [158]. Matrix metalloproteinase 23 (MMP23B), another significantly upregulated protein in 10 ng/mL TGF-β3 and 3μW light treated samples (+T, +L3), has been linked to cartilage or bone formation and metabolism. In a murine model, *Mmp23* gene expression in chondrocytes and osteoblasts exhibited time-dependent changes similar to collagen II expression profiles, with a suggested role in endochondral ossification [159].

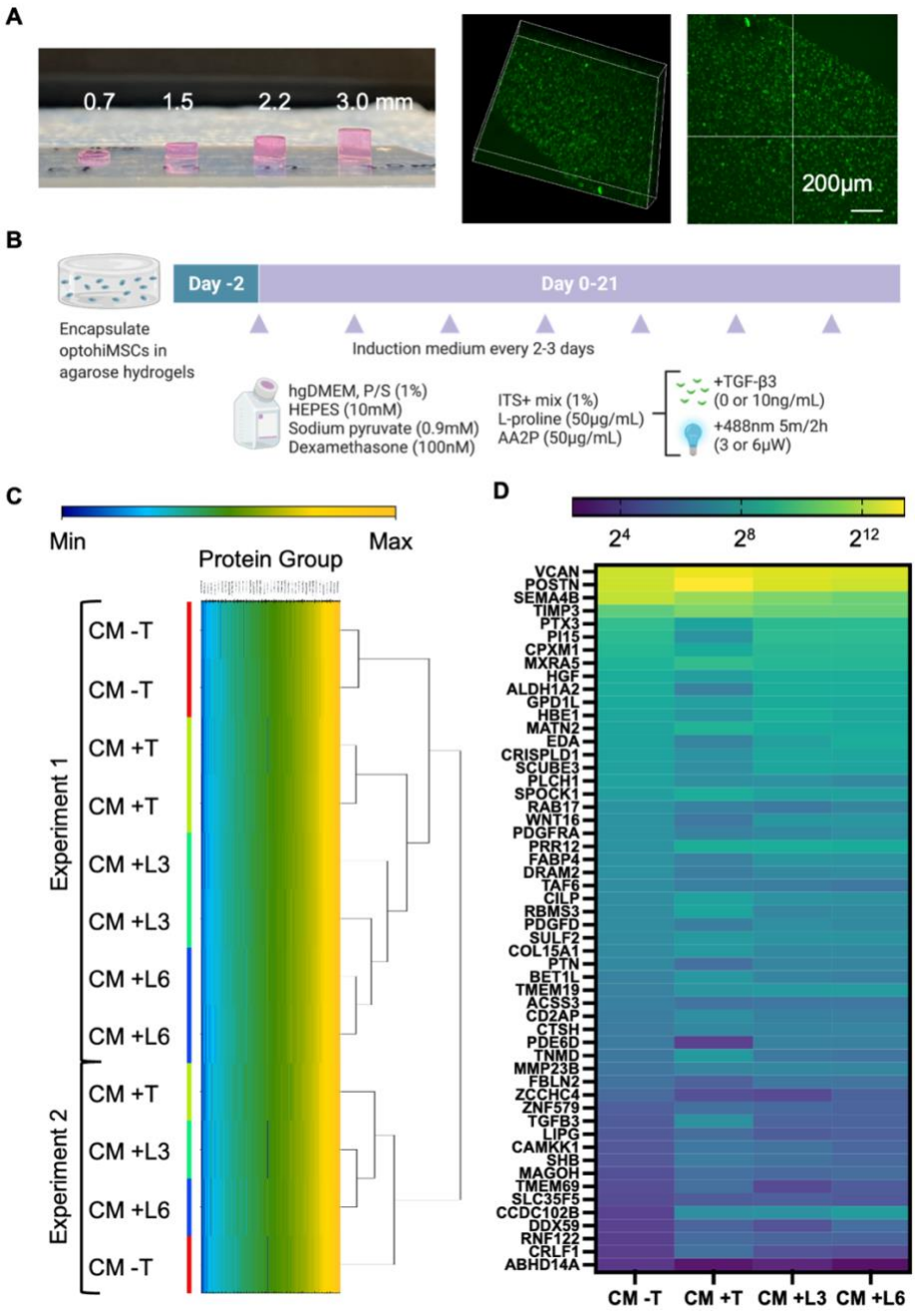

Figure 4.10. TGF-β mediated chondrogenic differentiation. (A) optohiMSCs were encapsulated in 2% agarose at 20 × 10^6 cells/mL. Hydrogels can be made to varying thicknesses and cut by biopsy punches to fit a 96-well plate format. **(B)** 2 days after encapsulation, 1.5mm-thick hydrogels were switched to basal chondrogenic medium (CM) with either no TGF-β (-T), 10ng/mL TGF-β3 (+T), 3 or 6 µW 488 nm light with 5 min pulses every 2 hours (+L3, +L6) for 21 days total. **(C)** Clustered heatmap showing total protein expression levels. **(D)** Candidates with $\log_2$FC 0.58 with FDR 0.05 between +T/-T groups, displayed as $\log_2$(mean) of n = 3.

4.3 Discussion

We report the development of an optogenetic hiPSC system with demonstrated utility to control and study TGF-β signaling during differentiation into MSCs and subsequently into the smooth muscle cells, tenocytes, and chondrocytes. Optogenetic stimulation of TGF-β expression in the absence of its soluble form upregulated gene and protein expression of known markers for directed differentiation of hiPSCs into mesenchymal lineages (smooth muscle cells, tenocytes, and chondrocytes), with minimal phototoxicity over multiple weeks of culture. Chondrogenic differentiation necessitated cell encapsulation into thin hydrogel instead of monolayer culture. We believe that this is the first instance of optogenetic-mediated cell differentiation carried out in 3D.

Since its initial applications in neuroscience for precise activation of neural circuits, optogenetics has been recognized for its potential to interrogate cell signaling pathways with fine spatiotemporal control. Such systems, including those developed for Ras/Erk, FGF, Wnt, and BMP signaling [91,147,148,160], commonly rely on light-activated interactions between optogenetic proteins coupled to signaling receptors. Their characterization has largely been focused on upstream responses such as receptor localization and protein phosphorylation in immortalized cell lines. Only recently have these systems been studied in human adult neural stem cells [161] and human embryonic stem cells (hESCs) [162].

The field has also begun to successfully exploit the temporal control advantages of optogenetic tools, for example, to deliver a transient pulse of Wnt-activating light for initial hESC mesoderm induction towards differentiation into cardiomyocytes [162]. Another key advantage of an optogenetic system is its potential for precise spatial patterning of stem cell

fate, recapitulating the patterning during tissue development and regeneration. The feasibility of applying photomasks or guiding lasers to achieve illumination patterns in optogenetic systems has been demonstrated for cell monolayers [11,162]. Small light-sensitive neural spheroids have been used to pace neuromuscular junctions and cardiac cells [163–165].

We opted to develop an hiPSC-based optogenetic TGF-β system, as it offers several advantages over other cell types. hiPSCs can be derived from a small sample of blood and expanded nearly indefinitely, allowing for multiple cell types with or without optogenetic capabilities to be generated from the same source, thus enabling patient-specific studies. However, the introduction of optogenetic systems into hiPSCs may present concerns such as undefined integration with oncogenes or key genes, unstable transient expression, and suppression of endogenous receptors. To mitigate these effects, we opted for a lentiviral delivery approach using the EF-1α promoter, which has shown comparatively high transduction efficiency with low gene silencing and low oncogenic potential [151]. In multiple clones, we confirmed that the transduction protocol we used did not affect the pluripotency of hiPSCs **(Figure 4.1E, 4.2)** or their functional ability to differentiate into hiMSCs **(Figure 4.3B, 4.4).** The remaining assays and experiments were therefore conducted using one clone. We verified a normal karyotype **(Figure 4.1F)** and similar expression of endogenous TGFBRs between optogenetic cells and their wild type counterparts **(Figure 4.5).**

Previous studies of similar optogenetic systems have observed a dose-dependent response to light intensity at the level of protein phosphorylation, and a threshold effect of

light duration [11,147,148]. Compared to the long-term optogenetic FGF signaling for maintaining stem cell pluripotency (delivering blue light at 1 $\mu W/mm^2$ in 1-10 minute pulses every 2 hours, over several weeks to months) [147], we used 32- and 63-fold lower light intensities with similar timing for our studies, and observed no light-induced apoptotic effects over 2 weeks of stimulation of cells in monolayer **(Figure 4.6D).**

TGF-β modulates key functions of MSCs, ranging from proliferation to multilineage differentiations [134]. Beyond upstream effects in canonical TGF-β signaling such as nuclear localization of the phosphorylated Smad complex, we demonstrate that light-activated TGF-β signaling could drive differentiations into mesenchymal lineages. In our study, expression of the optogenetic system was retained after differentiation of hiPSCs **(Figure 4.3A)**, and optogenetic editing did not affect the ability of hiPSCs to differentiate into MSCs and downstream progeny **(Figure 4.3C).** In smooth muscle differentiation of MSCs, stiff substrate and TGF-β have been identified as critical factors [136,152], while in tenogenic protocols, stepwise supplementation with additional growth factors is necessary [137]. In medium containing low serum and no TGF-β, we used light-activated TGF-β signaling to recapitulate the role of soluble TGF-β in differentiations of optohiMSCs into smooth muscle and tenogenic lineages **(Figure 4.6A, 4.9A, 4.7)**. Immunostaining for smooth muscle and tenogenic differentiation markers **(Figure 4.6C, 4.9C)** showed morphological changes comparable to published effects of soluble TGF-β on differentiation into smooth muscle and tenogenic cells [136,137]. We also drove chondrogenic differentiation of optohiMSCs encapsulated in biologically inert 3D agarose hydrogels using chemically-defined medium with blue light in lieu of soluble TGF-β3 **(Figure 4.10A, 4.10B).**

Our hydrogel-encapsulated optohiMSC model for chondrogenic differentiation demonstrates that optogenetic stimulation can be used in millimeter-sized 3D settings. The 1.5mm-thick hydrogel discs had the thickness of native human cartilage, serving as a proof-of-concept for a step towards extending the potential of optogenetic tools into tissue engineering with spatially precise control of cell fate. For optical stimulation through thicker and less translucent tissues, blue light-activated optogenetic tools may be used in conjunction with two-photon excitation or photon upconversion biomaterials [166–169], or with recently reported red or far-red optogenetic proteins [160,170–174].

Across the three mesenchymal lineages studied, groups which received light-activated TGF-β signaling (+L3, +L6) had expression levels of differentiation markers closer to the soluble factor treated conditions (+T) than to the untreated controls (-T), though at slightly lower expression levels than the soluble TGF-β3 positive control **(Figure 4.6B, 4.6C, 4.9B, 4.9C, 4.10C, 4.10D).** We observed this pattern across multiple assays including qRT-PCR, immunostaining, and global quantitative proteomics. Interestingly, effects of 5-minute pulses of blue light every 2 hours in the 3 μW light-treated groups (+L3) were more similar to conventional soluble TGF-β3 treated groups (+T) than the same regime in the 6 μW light-treated groups (+L6). An increase in the intensity of optogenetic stimulation did not result in upregulation of differentiation markers, suggesting the need for further optimization of illumination conditions with additional parameters such as pulse length or frequency.

One limitation of this study is that hiPSC-derived cells do not fully recapitulate the function or phenotype of primary cells from adult tissues, which is well known in the field [63,175,176]. We observed differences in MSC surface marker expression between bone

marrow and iPSC derived MSCs **(Figure 4.4),** consistent with previous reports that hiMSCs have gene expression profiles reminiscent of vascular progenitor cells [63]. However, with the increasing success in maturing hiPSC derivatives, these cells continue to serve as an attractive cell source in areas ranging from patient-specific *in vitro* models for drug screening and disease modeling, to personalized cell therapies for regenerative medicine.

The precise spatiotemporal control of TGF-β signaling by optogenetic tools provide opportunities for a more comprehensive understanding of hiPSC behavior and the development of hiPSC-specific differentiation protocols. Others and ourselves have opted for lentiviral delivery of optogenetic systems [91,148,160,161], but with the recent rise of CRISPR-Cas9 technologies, highly specific knock-ins to prescribed safe harbor loci are increasingly used [147,162]. Improvements in genetic modification techniques will increase the ease with which complex optogenetic systems can be delivered, though adeno-associated viral (AAV) vectors have successfully been used to transduce cells *in vivo* for clinical optogenetic applications, notably for the partial restoration of visual function in a human patient [177,178].

The hiPSC-based optogenetic tool described here could also be applied to study the versatile roles of the TGF-β family in the regulation of a number of conditions, ranging from fibrosis to inflammation and cancer stemness. For example, there is an opportunity to study the crosstalk between TGF-β signaling and other pathways, such as BMP in a developing joint [47] or Ras/Erk in cancer progression [179]. With recent advances in the ease and efficiency of genome editing, it may soon become possible to concurrently express and orthogonally control multiple optogenetic signaling pathways in a single hiPSC line. The necessary

optogenetic tools, including multicolor light-responsive proteins and illumination devices, are also under development [153,160,170–174].

We have shown the feasibility of optogenetics-driven differentiations of hiPSCs, and future studies could capitalize on the spatiotemporal advantages of optogenetic tools and the versatility of a patient-specific cell sources to enable precise understanding of cellular decision making and fate.

4.4 Conclusion

In summary, we demonstrate the capability of a novel hiPSC-based optogenetic system to direct TGF-β mediated mesenchymal differentiation into smooth muscle, tenogenic, and chondrogenic lineages. The resulting optogenetically edited cells can serve as a versatile tool for regulating TGF-β signaling in MSCs. The collected data suggest that optogenetic regulation of TGF-β signaling can enable precise control of hiPSC differentiation into mesenchymal lineages, towards more comprehensive understanding of the role of TGF-β in regulating MSC function. Future work can harness the advantages of optogenetics to study and manipulate TGF-β signaling with unprecedented spatiotemporal control.

4.5 Materials and Methods

4.5.1 Plasmid Preparation

Retroviral plasmids containing tdTomato-tagged blue light-responsive TGF-β receptors (Addgene #118942) and iRFP682-tagged Smad2 (Addgene # 118943) were provided as a gift by Dr. Won Do Heo [11]. Transformed colonies of competent *E. coli* (C3019H; New England BioLabs) were selected, amplified, and purified (E.Z.N.A. Endo-Free

Plasmid DNA Kit; Omega Bio-Tek). Omitting the retroviral backbone, new lentiviral plasmids were designed using Benchling and SnapGene software and constructed using custom cloning service of Epoch Life Science. The sequences for the light-responsive TGF-β receptors and iRFP682-Smad2 were inserted separately into lentiviral backbones (pLV-EF1a-IRES-Neo; Addgene #85139). The lentiviral plasmids were similarly amplified and purified.

4.5.2 Lentiviral Transduction and Stable hiPSC Line Generation

Human embryonic kidney (HEK) 293T cells (ATCC) were cultured in high-glucose Dulbecco's modified Eagle's medium (hgDMEM; Gibco), 10% (v/v) Tet System Approved fetal bovine serum (FBS; Takara), 1 mM sodium pyruvate (Corning), and 1X GlutaMAX (Gibco) with media changes twice per week until reaching approximately 70% confluency. All human cells were maintained in a 37°C and 5% CO_2 incubator. Packaged lentiviral vector plasmid DNA (Lenti-X Packaging Single Shots; Takara) was added to the culture per manufacturer's protocol and virus supernatant was harvested after 48 and 72 hours. Stocks were pooled, filtered to remove cellular debris (0.45 μm pore size PVDF membrane vacuum filter; Millipore Sigma) and concentrated (Lenti-X Concentrator; Takara).

hiPSCs (GM25256; Coriell) were cultured on plates coated with Matrigel (Corning) diluted 1:175 in Roswell Park Memorial Institute (RPMI) 1640 Medium (Gibco), for 30 minutes at 37°C. hiPSCs were maintained in mTeSR Plus (STEMCELL Technologies) with media changes every other day. Upon reaching approximately 70% confluency, hiPSCs were dissociated using 500 μM ethylenediaminetetraacetic acid (EDTA; Thermo Fisher) and passaged in the presence of 5 mM ROCK inhibitor (Y-27632 2HCl; Tocris Bioscience).

Fresh viral titers were used to transduce hiPSC cultures (Lenti-X Accelerator; Takara) 1 day after passaging, then ROCK inhibitor was removed. Expression of vector plasmid DNA in target cells was verified by fluorescent microscopy (Olympus IX81) after 3 days. Colonies expressing tdTomato were manually picked, dissociated, resuspended in fluorescence-activated cell sorting (FACS) buffer comprised of phosphate-buffered saline (PBS; Corning) with 2% (v/v) FBS and 1 mM EDTA, and filtered through a 70 μm cell strainer. After single-cell sorting (BD FACSAria), cells were clonally expanded (CloneR; STEMCELL Technologies) to establish stable optogenetic hiPSC lines.

For G-banded karyotyping, hiPSCs were treated with KaryoMAX colcemid solution (Gibco) for 2 hours before dissociation and single cell resuspension in mTeSR Plus. For whole exome sequencing, hiPSCs were dissociated and submitted as cell pellets on dry ice to GENEWIZ for genomic DNA extraction, sequencing, and data analysis with human reference b37/Hg37.

4.5.3 hiPSC to MSC Differentiation

hiPSCs were differentiated into MSCs following manufacturer's protocol in the STEMdiff Mesenchymal Progenitor Kit (STEMCELL Technologies). Briefly, hiPSCs were passaged under standard conditions 2 days prior to starting a 4-day induction into early mesodermal progenitors. To derive mesenchymal progenitors, cells were then switched to the supplied MesenCult medium and passaged without using animal components to reach an approximately 70% confluency each time.

After the 21-day differentiation period, hiPSC-derived MSCs (hiMSCs) were cultured in MSC medium comprised of hgDMEM, 10% (v/v) fetal bovine serum (Corning), 1% (v/v)

penicillin/streptomycin (P/S; Gibco), and 0.1 ng/mL fibroblast growth factor (Peprotech) with media changes twice per week on uncoated tissue culture plastic. hiMSCs were dissociated using TrypLE (Gibco) and cryopreserved with NutriFreez D10 (Biological Industries).

4.5.4 Flow Cytometry for MSC Cell Surface Markers

To analyze MSC cell surface markers by flow cytometry, hiMSCs were dissociated and resuspended at 5×10^6 cells/mL in FACS buffer, and filtered through a 70 μm cell strainer. Using a human MSC analysis kit (BD Biosciences), cells were labeled with an antibody cocktail for positive markers containing APC anti-CD73, FITC anti-CD90, and PerCP-Cy5.5 anti-CD105 for 30 minutes, then washed and resuspended in buffer. Due to interference between the fluorescent tdTomato tag on optogenetic cells and the PE conjugated antibody cocktail for negative markers, another human MSC phenotyping kit (Miltenyi Biotec) was used to analyze lineage markers with PerCP anti-CD34, CD45, CD14, CD19, and HLA-DR. Unstained cells, single-color stained compensation beads (CompBead Plus Anti-Mouse Ig, κ; BD Biosciences), and isotype antibody cocktails controls were also included. Live cells were immediately run on the flow cytometer (Bio-Rad ZE5) using 5×10^5 cells per sample. Subsequent analyses were carried out using the FlowJo software. Samples were gated for tdTomato-positive single cells against the corresponding isotype control, such that <5% isotype was positive.

4.5.5 Tri-differentiation of MSCs

Optogenetic and non-optogenetic hiMSCs were compared for their tri-differentiation potential into adipogenic, osteogenic, and chondrogenic lineages using an hMSC functional identification kit per manufacturer's protocol (R&D Systems).

For adipogenic differentiation, cells were dissociated and replated at 2.1×10^4 cells/cm^2 in the supplied adipogenic basal medium on cover glass bottom 24-well cell imaging plates (Eppendorf), cultured to 100% confluency, then switched to the supplied adipogenic differentiation medium. After 21 days of culture with medium changes every 3-4 days, adipocytes were fixed for immunostaining.

For osteogenic differentiation, cells were dissociated and replated at 4.2×10^3 cells/cm^2 in the supplied osteogenic basal medium on cover glass bottom 24-well cell imaging plates (Eppendorf) which had been coated with 1 μg/mL fibronectin (R&D Systems) for 3 hours at 37°C. Cells were cultured to 50% confluency, then switched to the supplied osteogenic differentiation medium. After 21 days of culture with medium changes every 3-4 days, cells were fixed for immunostaining.

For chondrogenic differentiation, cells were dissociated and resuspended at 2.5×10^5 cells/mL in the supplied chondrogenic differentiation medium. Cell suspension was aliquoted at 1 mL per well into a deep-well U-bottom 96-well plate (Thermo Fisher), centrifuged at 200g for 5 minutes, and placed directly into the incubator to allow for self-assembly into condensed mesenchymal bodies over 2 days. After 21 days of culture with medium changes every 2-3 days, chondrogenic pellets were fixed for immunostaining.

4.5.6 Western Blot for TGFBR

Cell lysates were prepared in Pierce RIPA Lysis and Extraction Buffer with Halt Protease Inhibitor Cocktail, and protein concentrations were quantified using the Pierce BCA Protein Assay Kit (Thermo Fisher). 25 μg of protein in Laemmli Buffer was loaded in each lane of a 4-20% precast polyacrylamide gel, along with a Precision Plus Protein Dual Color ladder (Bio-Rad). The gel was transferred to a 0.45 μM polyvinylidene difluoride membrane, then the membrane was stained using Revert 700 (LI-COR) total protein stain, blocked in 5% bovine serum albumin (BSA) in Tris-Buffered Saline, 0.1% Tween 20 Detergent (TBST; Sigma), and incubated with an anti-TGFBR1 antibody (Abcam ab235178, 1:1000) recognizing the extracellular region of TGFBR1.

4.5.7 Blue Light Optogenetic Stimulation

Confocal laser stimulation and imaging were carried out on a multiphoton confocal microscope (Nikon A1RMP) with a live cell chamber, where cells were imaged first at baseline for 3 minutes without stimulation, then exposed to a 1-15 second pulses of 488 nm laser with 30 second imaging cycles, for up to 40 minutes total.

Longer-term light stimulation was carried out on an optogenetic stimulation device built according to the design reported by Bugaj and Lim [153] and manufactured by PCB Unlimited which is compatible with incubator culture, readily adaptable for any well plate format, consisting of 192 individually programmable blue LEDs (OSRAM LB T64G-V1CA-59-Z), diffusers to distribute light evenly across the well (Grafix K07MM1824-10, 40W CO_2 laser cutter), a black plate adapter (McMaster-Carr 8545K1, CNC machined) and black lid to limit spillover between wells. The 96-well plate format was constructed and used for hydrogel

experiments (chondrogenic differentiations) to reduce cell requirements. In addition, the corresponding adapter for a 24-well plate format was designed and used for monolayer experiments (smooth muscle and tenogenic differentiations) to allow for sufficient RNA quantity for qRT-PCR.

The 488 nm light output at each position of the optogenetic stimulation device was measured with a handheld optical power and energy meter (THORLABS PM100D) with a photodiode power sensor (THORLABS S130VC) at the 0.5 mW setting. The photometer was fit with adapters for the well-plate format to measure actual light intensity per well. Parameters for each position of the light stimulation device (illumination time, light intensity) were programmed in Arduino with the optoConfig graphical user interface [180].

4.5.8 Smooth Muscle and Tenogenic Differentiations

optohiMSCs were dissociated and replated in MSC medium on cover glass bottom 24-well cell imaging plates (Eppendorf) to reach approximately 70% confluency after 2 days, then switched to induction medium for smooth muscle or tenogenic differentiation. Basal smooth muscle medium consisted of hgDMEM with 5% (v/v) FBS and 1% (v/v) P/S [136]. Basal tenogenic medium was supplemented with additional factors: 50 μg/mL ascorbic acid 2-phosphate (Sigma), 100 ng/mL human recombinant growth/differentiation factor-7 (GDF-7; Peprotech), and after 3 days, 100 ng/mL human recombinant connective tissue growth factor (CTGF; Peprotech) [137]. A HEK293 secreted embryonic alkaline phosphatase (SEAP)-based reporter assay (Invivogen) was used to verify that the FBS used did not contain detectable levels of TGF-β **(Figure 4.7)**. Individual wells were subjected to one of the following conditions:

(1) no soluble TGF-β or optogenetic stimulation,

(2) soluble human recombinant TGF-β3 (Cell Signaling) alone at 10 ng/mL,

(3) optogenetic stimulation alone with 5-minute pulses every 2 hours at 3 μW/1.9 cm^2, or

(4) optogenetic stimulation alone with 5-minute pulses every 2 hours at 6 μW/1.9 cm^2.

The respective basal smooth muscle or tenogenic medium was changed every 3 days over 14 days of culture. Samples were freshly isolated for RNA or fixed for immunostaining.

4.5.9 Chondrogenic Differentiation

Sterile 4% (w/v) agarose solution was prepared by dissolving low gelling temperature agarose (Sigma) in PBS and autoclaving the solution. The agarose solution was maintained at 41°C in a water bath. hiMSCs were passaged, counted, and resuspended in MSC medium at a concentration of 40 × 10^6 cells/mL. Agarose solution and cell suspension were mixed at a 1:1 ratio and pipetted into an autoclave-sterilized casting mold comprised of a 1.5 mm-thick U-shaped rubber gasket clamped between two plain glass microscope slides. The 2% (w/v) agarose solution containing 20 × 10^6 cells/mL was allowed to gel for 10 minutes at room temperature before being removed from the casting mold. Individual 6 mm-diameter × 1.5 mm thick gel discs were biopsy punched, deposited into separate wells of an ultra-low attachment plate, and maintained in MSC medium for at least 2 days.

Hydrogels were transferred to individual wells of a cover glass bottom 96-well cell imaging plates (Cellvis) and switched to basal chondrogenic medium consisting of hgDMEM, 1% (v/v) P/S, 1% (v/v) insulin-transferrin-selenium mix (Corning), 10 mM 4-(2-

hydroxyethyl)-1-piperazineethanesulfonic acid (HEPES; Gibco), 0.9 mM sodium pyruvate (Gibco), 100 nM dexamethasone (Sigma), 50 μg/mL L-proline (Sigma), and 50 μg/mL ascorbic acid 2-phosphate (Sigma). Hydrogels were then subjected to one of the following conditions:

(1) no soluble TGF-β or optogenetic stimulation,

(2) soluble human recombinant TGF-β3 (Cell Signaling) alone at 10 ng/mL,

(3) optogenetic stimulation alone with 5-minute pulses every 2 hours at 3 μW/0.32 cm^2, or

(4) optogenetic stimulation alone with 5-minute pulses every 2 hours at 6 μW/0.32 cm^2.

For all groups, chondrogenic medium was changed every 3 days over 21 days of culture. Samples were snap frozen in liquid nitrogen for proteomics.

4.5.10 RNA Isolation and qPCR Analysis

RNA from cell monolayers was isolated using the RNeasy Micro Kit (QIAGEN) following manufacturer's protocol with on-column DNase treatment. RNA was quantified on a spectrophotometer (NanoDrop 1000; Thermo Fisher). cDNA was synthesized using the High-Capacity cDNA Reverse Transcription Kit (Applied Biosystems). Quantitative RT-PCR analysis was performed using 10 ng cDNA per reaction, Fast SYBR Green PCR Master Mix (Applied Biosystems), and primers synthesized by Life Technologies **(Table 4.1).** Target gene expression was normalized to the housekeeping gene GAPDH, and calculated from the mean Ct values of technical replicates for each sample.

Table 4.1. Primer sequences

Gene	Forward (5' to 3')	Reverse (5' to 3')
GAPDH	GCTCTCTGCTCCTCCTGTTC	ACCAAATCCGTTGACTCCGA
ASMA	ACGTGGGTGACGAAGCACAG	GGGCAACACGAAGCTCATTGTA
CNN1	GCTGTCAGCCGAGGTTAAGAA	TGAGGCCGTCCATGAAGTTG
SCX	CAGCGGCACACGGCGAAC	CGTTGCCCAGGTGCGAGATG
COL1A1	TAAAGGGTCACCGTGGCT	CGAACCACATTGGCATCA

4.5.11 Statistical analysis

Statistical analysis of qPCR data was conducted using GraphPad Prism software. Data were checked for whether they fit Gaussian distributions using the Shapiro-Wilk normality test. When normality was confirmed, statistical analysis was carried out by one-way analysis of variance (ANOVA) test and post hoc Tukey-Kramer's multiple comparisons test to compare groups (CNN1, COL1A1, SCX). When normality was not confirmed, statistical analysis was carried out by nonparametric Kruskal-Wallis test and post hoc Dunn's multiple comparisons test to compare groups (ASMA). Data were calculated as the mean ± SD using data from $n \geq 6$ replicates. $P < 0.05$ was considered statistically significant.

4.5.12 Immunostaining

Samples were fixed in 4% (v/v) paraformaldehyde for 15 minutes at room temperature. Chondrogenic pellets were embedded in paraffin and sectioned at 5 μm-thick. Monolayers were permeabilized in 0.25% (v/v) Triton-X (Sigma) and 5% (v/v) FBS for 20 minutes at room temperature. Paraffin-embedded sections were baked for 30 minutes at 60°C, then deparaffinized and rehydrated in Citrisolv (Fisher Scientific) followed by a graded ethanol series. Antigen retrieval was performed in citrate buffer (10 mM sodium citrate, pH 6.0) heated to boiling for 20 minutes and cooled for another 20 minutes. For all samples,

blocking was done using 10% (v/v) secondary antibody-matched serum for 2 hours at room temperature. Primary antibodies in blocking solution were incubated on samples overnight at 4°C (please see **Table 4.2** for antibodies and their dilutions). To show the specificity of the antibody binding, negative controls were stained without primary antibodies. Secondary antibodies were all prepared at 1:1000 dilution in 5% (v/v) serum and incubated for 2 hours at room temperature. After nuclear staining with Hoechst 33342 (Abcam), monolayer wells were maintained in PBS, while paraffin sections were dehydrated and cleared in a graded ethanol series followed by Citrisolv (Fisher Scientific) and mounted under cover glass with Permount (Fisher Scientific). Fluorescent images were acquired on a multiphoton confocal microscope (Nikon A1RMP).

Table 4.2. Immunohistochemistry primary antibodies, human

anti-	Company	Catalog No.	Dilution
SOX2	Abcam	ab97959	1:500
OCT4	Abcam	ab181557	1:250
NANOG	Cell Signaling	4903	1:200
Aggrecan	R&D Systems	967800	10 µg/mL
FABP4	R&D Systems	967799	10 µg/mL
Osteocalcin	R&D Systems	967801	10 µg/mL
ALP	Abcam	ab75699	1:25
Cleaved caspase-3	Cell Signaling	9661	1:400
Calponin 1	Cell Signaling	17819	1:100
aSMA	Invitrogen	14-9760-82	1:500
SCXA	Abcam	ab58655	1:200
Collagen I	Cell Signaling	66948	1:200

4.5.13 Global Quantitative Proteomic Analysis

For global quantitative proteomics, diaPASEF (data independent acquisition based proteomics) was used [181]. In brief, hydrogel encapsulated cells were lysed in buffer (1% SDC, 100 mM TrisHCl pH 8.5, and protease inhibitors) and boiled for 10 min at 95°C, 1500

rpm [182]. Protein reduction and alkylation of cysteines was performed with 10 mM TCEP and 40 mM CAA at 45°C for 10 min followed by sonication in a water bath, cooled down to room temperature. Protein digestion was processed overnight by adding LysC and trypsin in a 1:50 ratio (µg of enzyme to µg of protein) at 37° C and 1400 rpm. Peptides were acidified by adding 1% TFA, vortexed, and subjected to StageTip clean-up via SDB-RPS [183]. Peptides were loaded on 14-gauge StageTip plugs. Peptides were washed two times with 200 µL 1% TFA 99% ethyl acetate followed 200 µL 0.2% TFA/5%ACN in centrifuge at 3000 rpm, followed by elution with 60 µL of 1% ammonia, 50% ACN into Eppendorf tubes and dried at 45°C in a SpeedVac centrifuge. Samples were resuspended in 10 µL of LC buffer (3% ACN/0.1% FA). Peptide concentrations were determined using NanoDrop and 200 ng of each sample was used for diaPASEF analysis on timsTOFPro.

Peptides were separated within 120 min at a flow rate of 400 nL/min on a reversed-phase C18 column with an integrated CaptiveSpray Emitter (25 cm × 75 µm, 1.6 µm, IonOpticks). Mobile phases A and B were with 0.1% formic acid in water and 0.1% formic acid in ACN. The fraction of B was linearly increased from 2 to 23% within 90 min, followed by an increase to 35% within 10 min and a further increase to 80% before re-equilibration. The timsTOF Pro was operated in diaPASEF mode [181] and data was acquired at defined 32 × 25 Th isolation windows from m/z 400 to 1,200. To adapt the MS1 cycle time in diaPASEF, the repetitions were set to 2 in the 16-scan diaPASEF scheme. The collision energy was ramped linearly as a function of the mobility from 59 eV at 1/K0=1.6 Vs cm-2 to 20 eV at 1/K0=0.6 Vs cm-2.

The acquired diaPASEF raw files were searched at default settings for targeted analysis of DIA data against the human UniProt fasta database in Spectronaut [184]. The false discovery rate (FDR) was estimated using the mProphet approach and set to 1% at peptide precursor level and at 1% at protein level. Results obtained from Spectronaut were further analyzed using the Spectronaut statistical package. Significantly changed protein abundance was determined by un-paired t-test with a threshold for significance of $p < 0.05$ (permutation-based FDR correction) and 0.58 $\log_2$FC.

Chapter 5: Aim 3

Engineer native-like human articular cartilage by optogenetic control of TGF-β signaling and interfacing with bone substrate

Osteoarthritis (OA) is the most common joint disease worldwide, due at least in part to our limited understanding of disease etiology and pathology leading to the lack of effective treatment options. Animal models which are currently used for drug discovery continue to fall short of recapitulating human physiology, as evidenced by the continued failures of disease-modifying OA drugs in clinical trials. It is thought that bioengineered cartilage-bone tissue models could recapitulate physiological interactions with patient-specific cells and disease-initiating factors more closely than current animal models. Essential to tissue homeostasis, disease pathogenesis, and therapeutic responses are the establishment of stratified cartilage and cartilage-bone crosstalk at the osteochondral junction. The formation of stratified cartilage with osteochondral interactions would in turn require spatiotemporal gradients of growth factors and interfacing bone matrix. Thus far, it was not possible to simultaneously incorporate these features into a single engineered system, due to the low precision of manipulating soluble factors. Motivated by these challenges, we developed a cartilage-bone model using human induced pluripotent stem cell (hiPSC)-derived chondrogenic spheroids in which transforming growth factor (TGF)-β signaling, a pathway central to chondrogenesis, could be optogenetically controlled. The use of light to pattern spatiotemporal TGF-β gradients allowed for the maintenance of hyaline-like conditions at

the articular surface and supported superficial zone formation. We anticipate that these light-based TGF-β gradients can be maintained in parallel with hypertrophic or osteo-inductive factors to promote middle and deep zone formation, and can be readily applied in complex settings such as microphysiological systems or bioreactors with mechanical loading. This platform for optogenetic TGF-β signaling in an engineered cartilage-bone model enables the formation of stratified tissues, towards the development of more physiological, patient-specific models of joint disease.

5.1 Introduction

OA is the most common joint disease affecting over 500 million people worldwide, further increasing with an aging population, with OA of the knee alone already contributing more than $27 billion in annual health care expenditures [2]. Patients suffer from a lack of effective disease management strategies beyond analgesia or surgical intervention, with continued failures in repurposing disease-modifying anti-rheumatic drugs (DMARDs) for OA or bringing disease-modifying OA drugs (DMOADs) through successful completion of clinical trials [5].

OA remains a chronic degenerative condition with limited treatment options, due – at least in part – to the lack of high-fidelity models that would help better understand disease progression and test novel therapeutics [38]. The stratified organization of cartilage and crosstalk at the osteochondral junction are essential to both cartilage homeostasis and disease. OA typically starts with small lesions in the superficial layers and compensatory matrix production from the deeper layers, until the calcified layers wear away to expose bone. In addition, OA pathogenesis is mediated by disruptions in tissue crosstalk at the

osteochondral junction [45,46]. Rodent models, the gold standard, may capture some of these features, but there remains an unmet need for high-fidelity models that meet all the above requirements in a patient-specific manner. Human *in vitro* bioengineered cartilage-bone tissue models currently lack the complexity offered by *in vivo* systems, including the effects of tissue architecture and interactions with other tissues [6]. These limitations motivate the need for advanced human tissue models which can capture the complexity of joint disease, ultimately leading to improvements in the therapeutic discovery process.

Strategies for engineering stratified cartilage can broadly be grouped into those introducing stratification by manipulating the cells, scaffold, or environment. Earlier studies isolated subpopulations of bovine chondrocytes from zonally sectioned cartilage and encapsulated them in hydrogels for layered repatterning, but these cell-based approaches typically suffer from low cell numbers and a fundamental lack of patient specificity [59,185,186]. Self-assembling chondrogenic spheroids have been used for some time, but only recently have true osteochondral organoids been formed from murine iPSCs by mimicking endochondral ossification to recapitulate some organ-specific features and cartilage-bone crosstalk [76].

For larger and more architecturally complex tissues, the scaffold can be useful for introducing a number of depth-dependent heterogeneities, for example gradients of stiffness, porosity, or growth factors. To engineer the spatially localized physical and biochemical cues, biofabrication methods have included tuning hydrogel composition, electrospinning, 3D bioprinting, melt electrowriting, porogen leaching, and directional freezing [78–82,187]. Cartilage-bone interactions are also commonly introduced to the

model via the scaffold. We have demonstrated the technical feasibility and biological utility of interfacing decellularized bone extracellular matrix (ECM) with engineered cartilage towards forming better stratified tissues [12,13]. However, scaffold-based approaches cannot provide temporal control, especially once seeded cells begin to produce their own ECM and remodel their surroundings.

Thus, manipulation of the environment external to engineered tissues has recently become of great interest. In simple transwell cultures, cartilage tissue constructs formed from human bone marrow-derived MSCs under physiological spatiotemporal regulation of TGF-β signaling demonstrated improved *in vivo* stability compared to their isotropic control counterparts, resisting endochondral ossification and retaining physiologic stratified organization [54]. Magnetic field alignment of growth factor conjugated superparamagnetic nanoparticles has also been used to similar effect, and others have applied buoyancy, acoustic, and other external force fields to establish signaling gradients [85,84,188,88]. However, these strategies are difficult to translate to more complex settings, such as diffusion-limited cultures which require perfusion, or microphysiological organ-on-a-chip platforms to study interactions between cartilage, bone, synovium, and other connective tissues [14,83,189].

In the present study, we sought to overcome the limitations of prior work to engineer an advanced *in vitro* tissue model with essential features for studying joint disease – patient specificity, cartilage organization, and cartilage-bone crosstalk. It has been established that both spatiotemporal gradients of TGF-β signaling and bone matrix interfaced with cartilage support the development of stratified cartilage [12,13,54]. However, it was not possible to

simultaneously leverage these findings in a single engineered system, and past studies were carried out using bone marrow-derived MSCs whereas disease modeling for personalized therapies will necessitate the use of human autologous cells which can be derived in a minimally invasive and patient-specific manner. We developed an optogenetic human iPSC (hiPSC)-based system for controlling TGF-β signaling in space and time, in a way leading to the formation of stratified cartilage. In addition to the precise control of TGF-β, this approach enabled incorporation of bone substrate into the model, to introduce additional developmentally important signaling factors. We anticipate that the engineered *in vitro* model with patient specificity, native-like cartilage architecture, and osteochondral interactions will ultimately support more robust mechanistic and drug discovery for joint disease.

5.2 Results

5.2.1 Development of a Light-Accessible Cartilage-Bone Tissue Model

Our objective was to develop an hiPSC-based cartilage-bone tissue model in which we can introduce gradients of TGF-β signaling using light, to promote the formation of cartilage with more native-like architectures. We hypothesized that optogenetically edited hiPSCs can form chondrogenic spheroids and fuse into a cohesive and cell-dense layer of cartilage integrated with a subchondral bone scaffold. We further posited that after an initial period of isotropic chondrogenic induction with soluble TGF-β, optogenetically activated TGF-β signaling could maintain hyaline induction conditions at the superficial surface, but attenuate with depth to enable hypertrophic induction at the osteochondral interface. To this end, we used decellularized bone matrix scaffolds, optogenetic hiPSC-derived MSCs

(hiMSCs), and two cartilage-bone reactors supporting the tissue forming and light stimulation culture phases, respectively **(Figure 5.1A).**

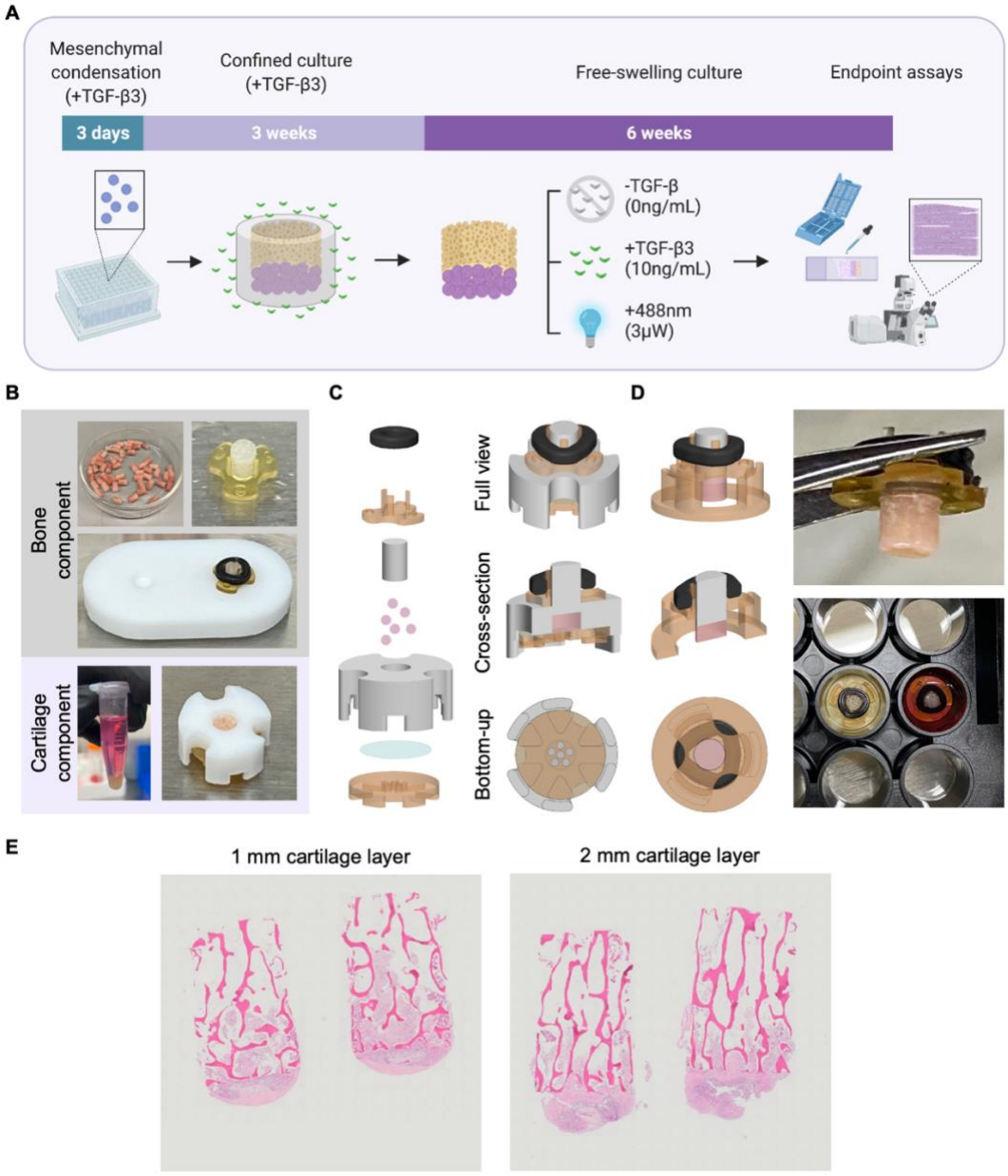

Figure 5.1. Cartilage-bone tissue model for optogenetic stimulation. (A) Study design. **(B)** Decellularized bone scaffold and optogenetic chondrogenic spheroids, prepared for tissue seeding. **(C)** Tissue formation setup for confined culture over 3 weeks. **(D)** Tissues detached and transferred to light-accessible culture platforms for optogenetic stimulation in black cover glass bottom 24-well plates, with the superficial cartilage surface closest to the light source. **(E)** Hematoxylin and eosin staining of 1 and 2 mm-thick cartilage layers, with cylindrical tissues bisected longitudinally and sections from both halves embedded in the flat orientation.

For the bone component, scaffolds were derived from the trabecular bone of bovine distal femurs, completely decellularized, and cut into cylinders measuring 3.5 mm in diameter by 5.5 mm in height, ranging from 30-35 mg in dry weight. The bone could be set at various positions within its holder to dictate the thickness of the cartilage layer. For the cartilage component, condensed mesenchymal bodies (CMBs) were formed from optogenetic hiMSCs and then seeded into an ultra-low attachment Teflon chamber **(Figure 5.1B).**

After the chondrogenic spheroids were pressed into a bone scaffold, they were allowed to fuse and form a cartilage layer over 3 weeks. The tissue forming setup kept the developing cartilage under the compressed culture conditions previously deemed necessary for cohesive tissue formation [13]. To allow for nutrient exchange, the chondrogenic spheroids were contained by a 1 μm porous polycarbonate membrane on top of an Ultem polyetherimide support piece with through channels occupying approximately half of its surface area (6 × 1 mm-diameter channels over a 3.5 mm-diameter area) **(Figure 5.1C).**

Soluble TGF-β3 was maintained in culture medium at 10 ng/mL for the initial mesenchymal condensation and confined culture phases of tissue formation. Based on preliminary studies, the tissues were sufficiently mechanically stable to remove from the confined culture setups after 3 weeks, at which point they were transferred to a free-swelling, light-accessible culture platform **(Figure 5.1D).** The tissues were randomly distributed amongst experimental groups which (1) had TGF-β3 withdrawn for the remainder of culture, (2) continued to be supplemented with soluble TGF-β3, or (3) had TGF-β3 withdrawn but received optogenetic stimulation instead **(Figure 5.1A).** The optogenetic

stimulation regimen of 3 μW over the 1.9 cm^2 area of a 24-well with 5-minute pulses every 2 hours was established based on prior studies, with the superficial surface of the cartilage most proximal to the 488 nm light source **(Chapter 4).**

The volume of a CMB sphere was used to approximate the number of pellets needed to form a cartilage layer of a specified thickness. We opted to develop a 1 mm-thick cartilage layer with 1 mm penetration into the bone scaffold, based on pilot studies in which thicker cartilage layers showed limited ability to form cohesive tissues **(Figure 5.1E).** To measure the attenuation of blue light through cartilage of this thickness, we fabricated an extra set of tissues using the same methodologies, with an additional porous membrane separating the CMBs from the bone such that auxiliary components of the tissue forming setup could be detached as needed **(Figure 5.2A, 5.2B).** The 488 nm power output was measured in 3 configurations each **(Figure 5.2C)** for n = 7 tissues:

(1) Immediately over the light machine,

(2) In a black cover glass bottom 24-well plate with the empty cartilage reactor and chondrogenic medium, and

(3) With the full setup containing the cartilage tissue.

In the latter two configurations, a pinhole adapter matched the photometer to the cartilage reactor in the 24-well footprint **(Figure 5.2D).** Each position on the light machine was initially calibrated to 3 μW, with blue light attenuated by approximately 100-fold to 30 nW with the empty cartilage reactor and chondrogenic medium in place, and further attenuated by approximately 10-fold further to 3 nW through the depth of the tissue **(Figure 5.2E).** These measurements remained consistent between samples.

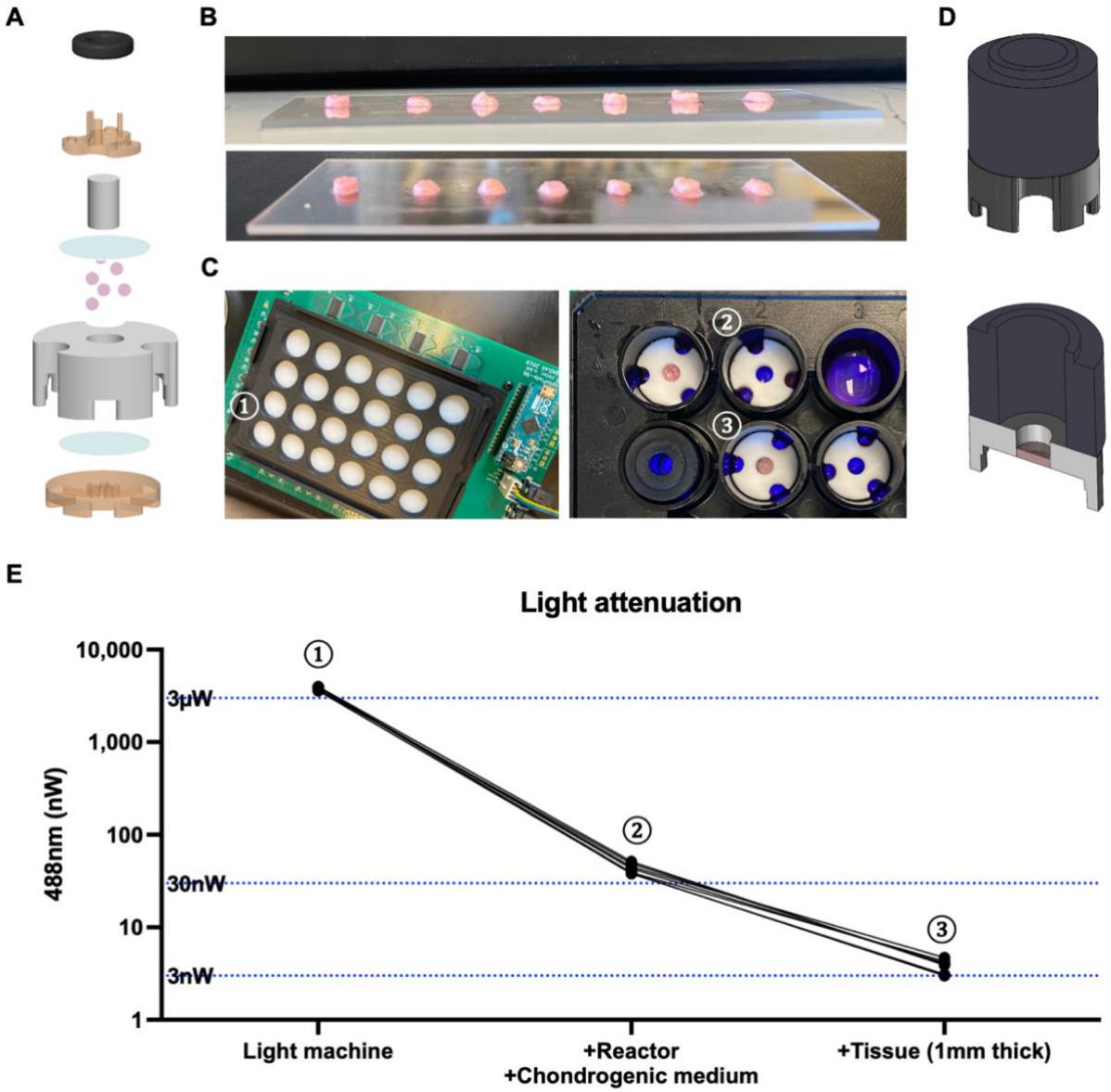

Figure 5.2. Attenuation of blue light through tissues. (A) Tissue formation setup for light attenuation measurements, with an additional polytetrafluoroethylene membrane separating the chondrogenic spheroids from the bone scaffold. **(B)** Photographs of the resulting 1 mm-thick cartilage discs after 3 weeks of confined culture on a 1 mm-thick glass slide for scale. **(C)** *Left:* 24-well light machine for optogenetic stimulation. *Right:* cartilage discs in their tissue forming chambers in chondrogenic media on a black cover glass bottom 24-well plate. Photometer readings were taken in the labeled configurations. **(D)** A pinhole adapter was used for measurements taken in configurations 2 and 3, added to fit the footprint of the photometer to the 24-well containing the cartilage tissues in their tissue forming chambers. **(E)** Measurements of blue light attenuation at the labeled configurations (n = 7 tissues).

5.2.2 Structural Features of Engineered Cartilage

After the entire duration of *in vitro* culture – 3 weeks of tissue formation where all groups received soluble TGF-β3 under confined culture conditions, followed by 6 weeks of free swelling culture with varied regimens of TGF-β – we assessed the ECM features of the resulting cartilage by Alcian Blue staining for glycosaminoglycans (GAGs) and second harmonic generation (SHG) imaging for collagen fibril alignment. GAG production, as indicated by binding of Alcian Blue dye, was seen in all experimental conditions, with sparser cell distributions observed in regions of greater GAG production **(Figure 5.3A).** In the optogenetically treated group, tissues had a largely uniform region with higher GAG content at the articular surface, tapering off after approximately 500 μm of depth. In comparison, soluble TGF-β3 or untreated tissues had pockets of higher cell density and GAG production scattered throughout the superficial region, creating a less uniform layer.

Closer examination by SHG imaging revealed the extent of collagen fibrillar organization **(Figure 5.3B)**. SHG signal is approximately scaled with fibril thickness squared [190]. Collagen I, a dominant component in bone matrix, typically forms thicker fibrils than collagen II, the primary form in cartilage, and thus the bone scaffold was readily identified in all tissues. In the tissues which had TGF-β signaling activated by soluble factor or light stimulation, fibrils running parallel to the articular surface were found in the superficial region. Tissues which received no TGF-β stimulation after 3 weeks had some of these parallel fibrils, though with faint SHG signal or lacking continuity across the superficial surface.

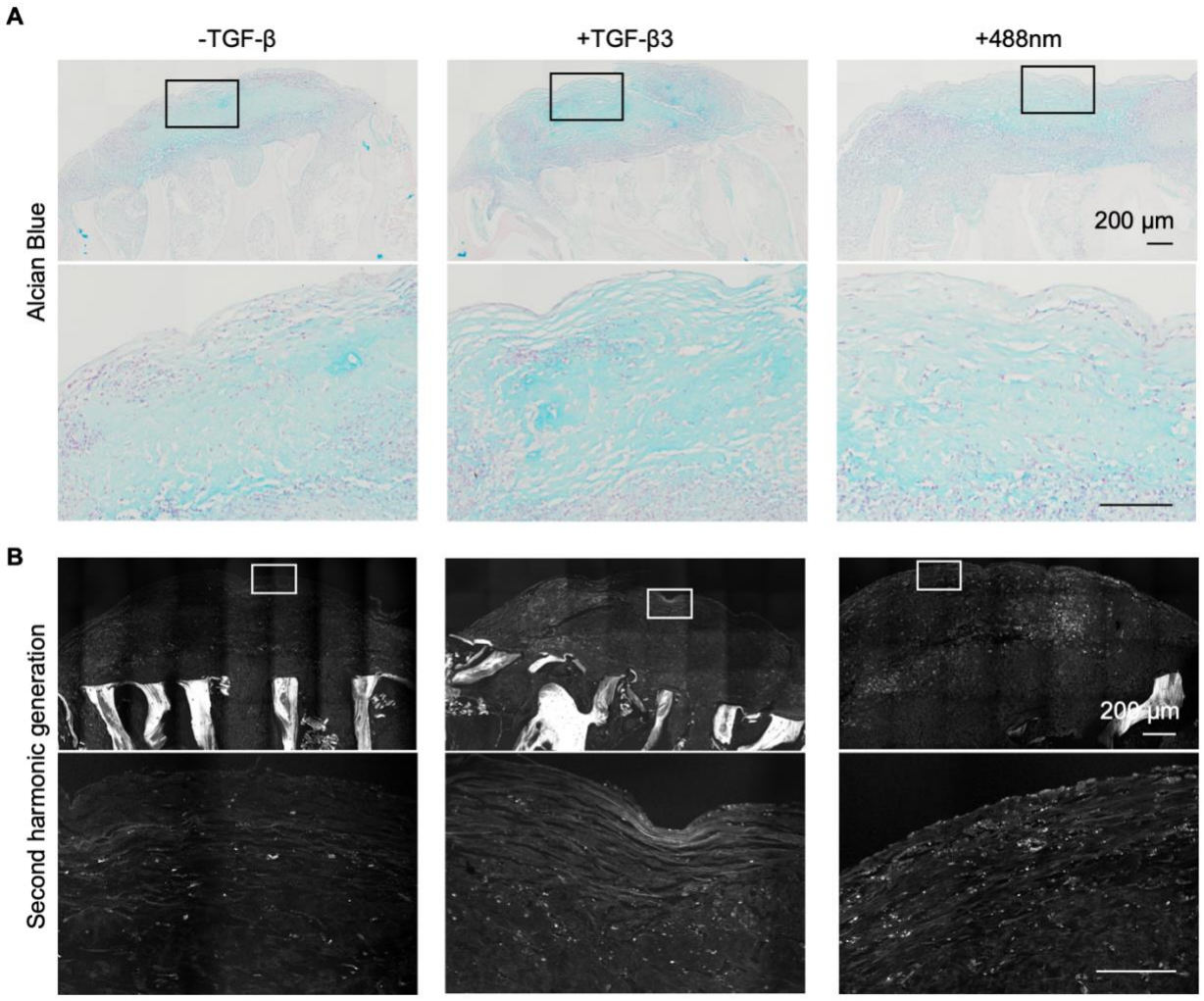

Figure 5.3. Matrix properties of engineered cartilage. (A) Alcian Blue (pH 2.5) staining for glycosaminoglycan content. **(B)** Second harmonic generation imaging for collagen fibril alignment.

5.2.3 Expression of Zonal Cartilage Markers

Staining for zonal cartilage markers was performed on depth-wise cross sections, using clusterin and lubricin for the superficial zone, cartilage intermediate layer protein (CILP) for the middle/deep zone, and collagen X for the deep zone. In tissues which continued to receive TGF-β stimulation by either soluble factor or light, clusterin stained more strongly than in tissues which had TGF-β withdrawn after the initial 3 weeks **(Figure 5.4).** In the optogenetically treated group, clusterin expression appeared more concentrated at the superficial surface of the cartilage compared to the soluble TGF-β3 treated group, in which there was no depth dependent pattern of expression. With lubricin, another superficial zone marker, we saw a similar expression pattern in the group which received light stimulation. Lubricin staining was stronger and localized to the superficial zone, though overall not as prominent as clusterin for any of the experimental conditions. In groups which received no TGF-β or continued TGF-β3, there was no observable lubricin staining compared to the control stained without the primary antibody. In both the soluble TGF-β3 treated and untreated groups, there were low expression levels of middle/deep zone marker CILP **(Figure 5.5A).** In the optogenetic group, we did not find noticeable CILP expression. Across all groups, there was minimal to no expression of deep zone marker collagen X **(Figure 5.5B).**

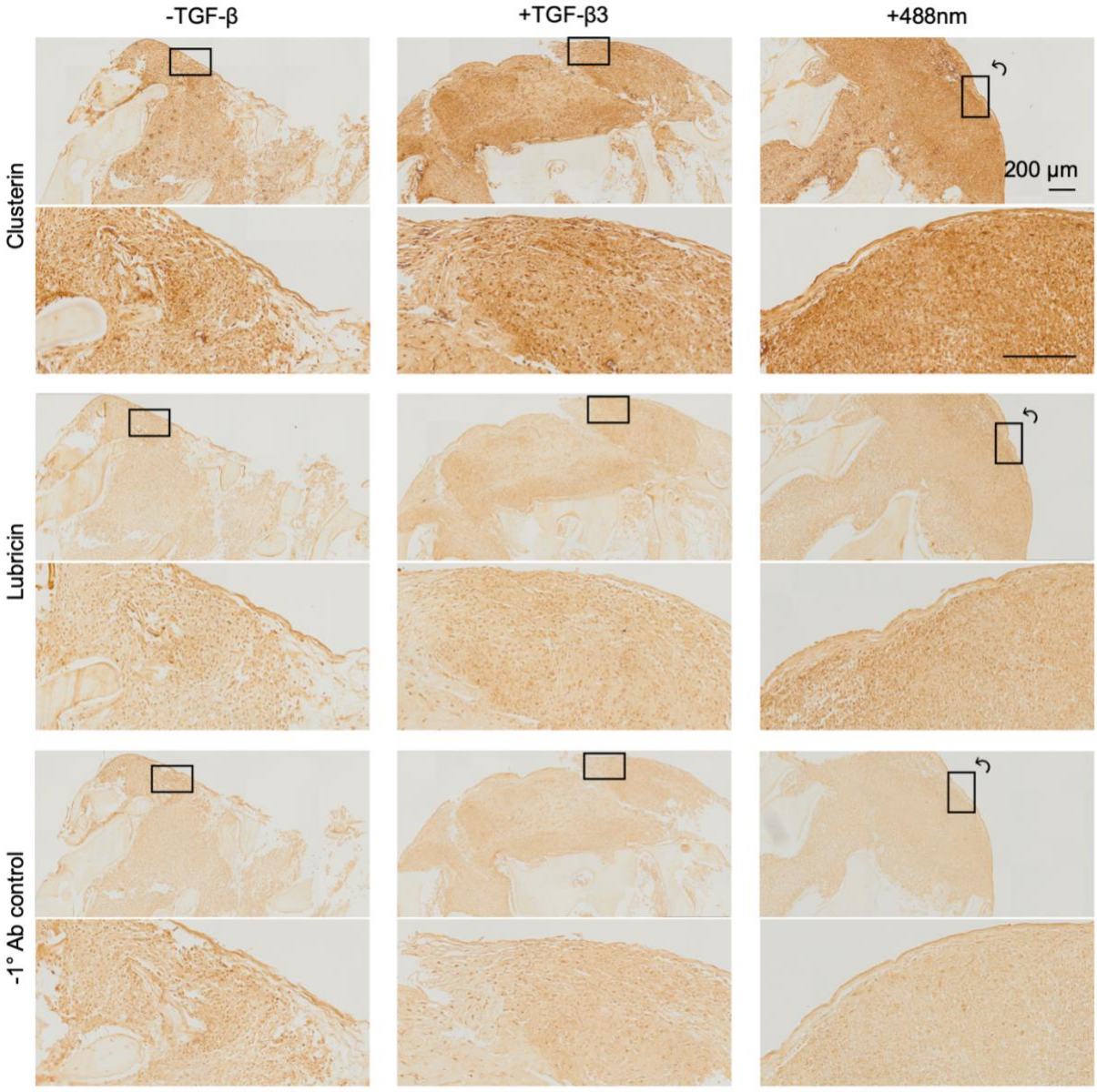

Figure 5.4. Immunohistochemistry for superficial zone markers, clusterin and lubricin.

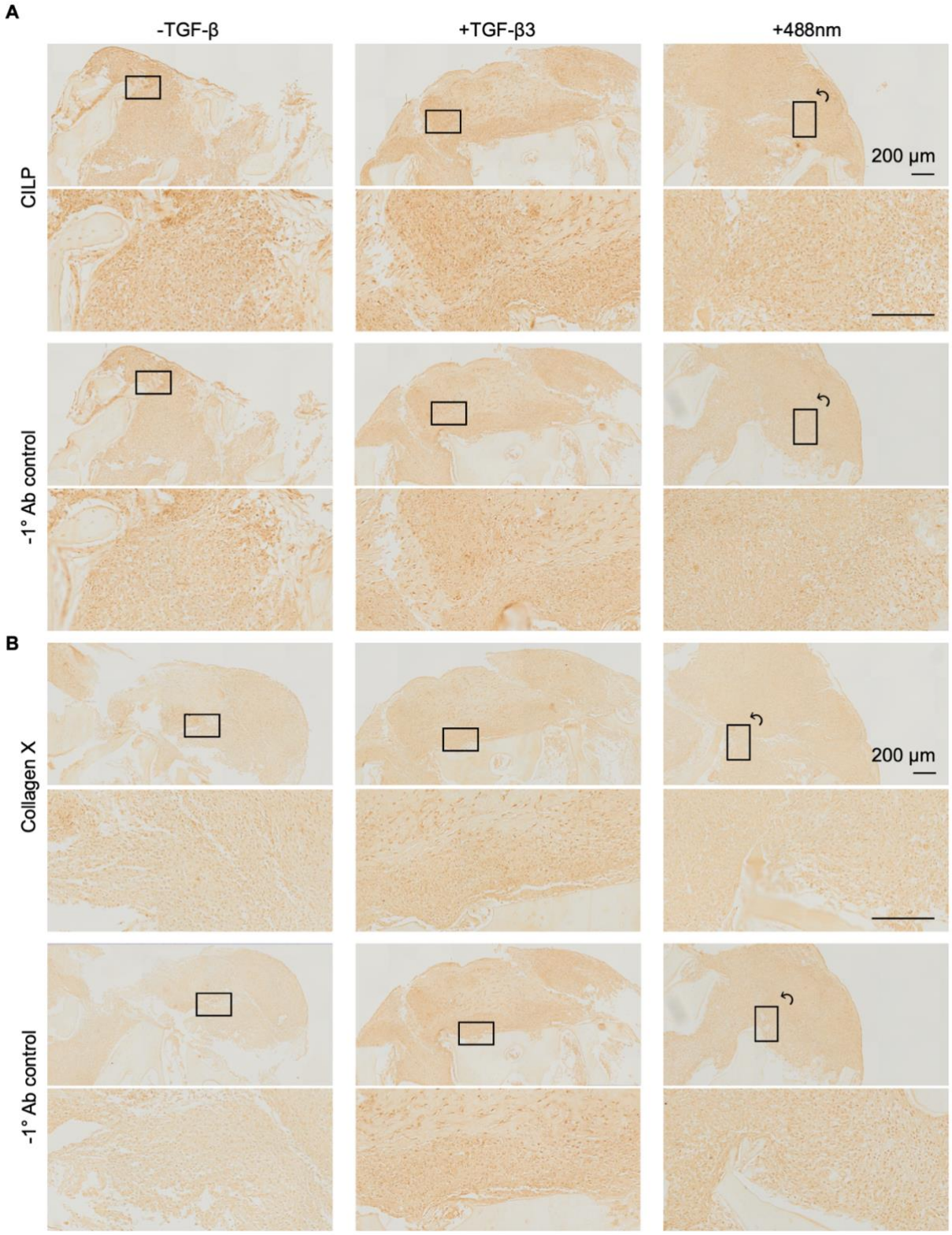

Figure 5.5. Immunohistochemistry for middle and deep zone markers. (A) CILP, a middle/deep zone marker, and **(B)** collagen X, a deep zone marker.

5.3 Discussion

In this study, we developed a light-accessible platform for engineering cartilage-bone tissues from hiPSC-derived spheroids (CMBs), enabling the optogenetic delivery of TGF-β signaling gradients to maintain hyaline-like conditions at the articular surface. After isotropic chondrogenic induction with soluble TGF-β3 for CMB formation and fusion over 3 weeks, tissues were switched to a light-based regimen to continue activating TGF-β signaling in the superficial region of 1 mm-thick cartilage. The Alcian Blue, clusterin, and lubricin stainings revealed that superficial zones with more uniform properties developed in optogenetically stimulated tissues compared to their soluble TGF-β3 treated or untreated counterparts **(Figure 5.3A, 5.4).**

Continued TGF-β stimulation throughout the culture period, via soluble factor or light, was necessary to establish collagen fibrils running parallel to the articular surface, as evidenced by the comparatively less prominent or organized collagen fibrils in tissues which had TGF-β withdrawn after the initial 3 weeks **(Figure 5.3B).** Based on minimal staining of markers CILP and collagen X, we found that the attenuation of TGF-β alone was not sufficient to drive hypertrophic conditions in the middle to deep zone **(Figure 5.5).** Nonetheless, the first instance of using optogenetics in engineered cartilage-bone tissues can be used to promote superficial zone formation or pattern spatial organization.

Though cartilage in its mature form has a uniquely sparse cell distribution compared to other tissues, its native development begins with the condensation of mesenchymal cells [47]. We opted to use CMBs as the basis for our scaffold-free engineered cartilage rather than traditional methods of encapsulating individual cells in hydrogels or other scaffolding

materials at cell densities one to two orders of magnitude below physiological levels [191]. As the tissues developed and cells began to secrete matrix components, we observed regions of lower cell density in areas of more prominent Alcian Blue staining for sulfated GAGs and glycoproteins **(Figure 5.3A).** The spheroid methodology also facilitated integration with an underlying bone scaffold, as previously demonstrated [12,13,189].

Early studies of chondrogenic CMBs as self-assembling building blocks for fabricating larger cartilage tissues *in vitro* predominantly used bone marrow or adipose-derived MSCs as their cell sources [12,57]. In comparison, hiPSCs can be derived from a small blood sample, and have advantages as easily obtainable patient-specific cells that can expand near indefinitely to achieve sufficient numbers, generate multiple cell types from the same source, and allow genetic modifications if needed. Few attempts have been made to assemble hiPSC-derived chondrogenic building blocks into zonally organized cartilage, and relied on pre-specification of cartilaginous or hypertrophic spheroid fate over several weeks prior to assembly into larger tissues [73]. Critically, the boundary proteins of chondrogenic spheroids are known to set after a few days and inhibit fusion with neighboring bodies, greatly limiting the ability of spheroids differentiated in isolation over several weeks to ultimately form larger, cohesive tissue [13]. Thus, we used a starting population of homogenous and early stage CMBs (Day 3) to form cohesively fused neocartilage, then harnessed the advantages of optogenetic stimulation to specify signaling gradients to the developing tissues *in situ*.

For hiPSC-derived chondrogenic spheroid formation, we opted to take an intermediate mesenchymal fate specification step and first generate hiMSCs, then follow

standard induction conditions typical for forming CMBs from bone marrow MSCs. Recent studies have elucidated key functional, phenotypic, and genetic differences between bone marrow MSCs and hiMSCs, and shown that hiMSCs resemble vascular progenitor cells, which can also undergo musculoskeletal differentiation, though under different inductive conditions [63]. Our hiMSC-derived tissues had less GAG deposition than similarly engineered spheroid-based tissues from bone marrow MSCs [12,13,54,192] **(Figure 5.3A)**, but we anticipate that applying hiMSC-specific inductive conditions or more developmentally guided protocols will improve outcomes [76]. The advantages of hiPSCs as the starting cell source still outweigh this hurdle, and just as the hiPSCs used in this study were readily edited to introduce the optogenetic TGF-β signaling system, the use of hiPSCs can enable further genetic modification to induce pro-regenerative properties or manipulate disease susceptibility [68,193].

Though optogenetically delivered TGF-β signaling gradients served to establish a more uniform superficial zone, the primary limitation of this study was the lack of prominent middle or deep zone features **(Figure 5.3B, 5.5)**. We initially hypothesized the depth-dependent attenuation of light-activated TGF-β signaling paired with subchondral bone matrix would provide sufficient hypertrophic conditions. Based on the findings of this study, we would propose the inclusion of stronger hypertrophic or osteo-inductive factors such as thyroxine or BMP-2, which could be conjugated to the subchondral scaffold [194]. Though there is utility in including even decellularized bone matrix, future work may incorporate osteoblasts and other cell types to establish a living bone component of the model [12,13].

Beyond features of the osteochondral unit, it may also be useful to include systemic contributors of joint homeostasis and disease such as circulating factors (proinflammatory cytokines, adipokines, hormones), and study interactions with other tissues such as the synovium or fat pad [195–197]. For an *in vitro* model, this would likely require the use of microphysiological systems [14,83,198,199]. The main methods for inducing OA-like catabolic changes *in vitro* broadly fall into the categories of cytokine stimulation and physical loading. While cytokine-induced OA has been studied with ease, loading-induced OA has only been applied to tissue explants and hydrogel-encapsulated human articular chondrocytes, but not to engineered osteochondral tissues [200]. Though the existing *in vitro* model approach may be incomplete, optogenetically engineered tissues will facilitate the application of other spatial patterning tools, and incorporation of the osteochondral grafts into platforms with fluidic flow or physical loading. Overall, the development of a light-based method for patterning TGF-β signaling offers a promising approach to directing the formation of organized cartilage, towards engineered tissue models for studying joint disease.

5.4 Conclusion

This study demonstrated the utility of using optogenetic TGF-β signaling to maintain hyaline-like conditions at the articular surface in engineered cartilage-bone tissues. In a cell-dense and cohesive cartilage layer assembled from hiPSC-derived chondrogenic CMBs, depth-dependent light gradients directed the formation of a more uniform superficial zone in terms of GAG deposition and expression of clusterin and lubricin, enabling the inclusion of a subchondral bone component. The precise maintenance of signaling gradients using light

rather than soluble factors could be combined with other methods to promote middle and deep zone formation. We anticipate that optogenetically driven spatial patterning for organized cartilage formation can be translated to complex settings such as microphysiological systems or bioreactors with mechanical loading, ultimately towards more physiological modeling of joint disease.

5.5 Materials and Methods

5.5.1 Scaffold Fabrication

Bovine calf metacarpus bones were purchased from Lampire Biological Laboratories (19D24003) and stored at -40°C. Using a vertical band saw, bone pieces were milled into smaller slices approximately 1 cm thick from the distal end of the metatarsal, as this region contains an enriched concentration of trabecular bone. From the 1 cm thick slices of bone, a drill press with a core drill bit was used to create cylindrical bone cores 3.5 mm in diameter. The cores were then fed into an IsoMet low speed wafering saw to trim each individual piece into 5.5 mm tall bone scaffolds with flat ends.

The scaffolds were stripped of all cellular material to leave behind the extracellular matrix with largely preserved composition, architecture, and mechanical properties using previously described methodology **(Chapter 3).** Bones were washed with high-velocity streams of water to remove the marrow from the pore spaces, and treated on an orbital shaker in four steps to remove any remaining cellular material: (i) phosphate-buffered saline (PBS; Corning) with 0.1% EDTA (w/v) for 1 hour at room temperature; (ii) hypotonic buffer of 10 mM Tris (Sigma), 0.1% EDTA (w/v) in DI water) overnight at 4°C; (iii) detergent (10 mM Tris, 0.5% SDS (w/v; Sigma) in DI water) for 24 hours at room temperature; (iv)

enzymatic solution (100 U/mL DNase, 1 U/mL RNase, 10 mM Tris in DI water; Sigma) for 6 hours at 37°C. Sonication was used to remove any remaining debris from the scaffolds.

After freeze-drying, decellularized bone scaffolds were weighed. Scaffolds of similar density were chosen for cell seeding (30-35 mg) and stored in 70% ethanol (v/v) for sterilization. Prior to cell seeding, ethanol was aspirated from the scaffolds and replaced with high-glucose Dulbecco's modified Eagle's medium (DMEM; Gibco) for at least 2 hours.

5.5.2 Derivation of Optogenetic Chondrogenic Spheroids

As previously described **(Chapter 4),** hiPSCs (GM25256; Coriell) were lentivirally transduced with light-responsive TGF-β receptors, clonally expanded, validated for pluripotency and normal karyotype, differentiated into hiMSCs (STEMdiff Mesenchymal Progenitor Kit; STEMCELL Technologies), and validated for MSC phenotype.

The hiMSCs were expanded in high-glucose DMEM (Gibco), 10% fetal bovine serum (FBS; Corning), 1% penicillin/streptomycin (P/S; Gibco), and fibroblast growth factor (0.1 ng/ml; Peprotech) with media changes twice per week and passaged using TrypLE (Gibco) up to P8.

The cartilaginous layer was generated from CMBs using our previously established protocol **(Chapter 2).** Briefly, hiMSCs were suspended at 2.5×10^5 cells/mL in chondrogenic medium comprised of high-glucose DMEM supplemented with 1% (v/v) P/S, 1% (v/v) insulin-transferrin-selenium mix (Corning), 10 mM 4-(2-hydroxyethyl)-1-piperazineethanesulfonic acid (HEPES; Gibco), 0.9 mM sodium pyruvate (Gibco), 100 nM dexamethasone (Sigma), 50 μg/mL L-proline (Sigma), 50 μg/mL ascorbic acid 2-phosphate (Sigma), and 10 ng/mL TGF-β3 (Cell Signaling). Cell suspension was aliquoted at 1 mL per

well into a deep-well U-bottom 96-well plate (Thermo Fisher), centrifuged at 200g for 5 minutes, and placed directly into the incubator to allow for self-assembly into CMBs over 3 days with daily media changes.

5.5.3 Tissue Formation and Cultivation

To form the tissues, the bone component of the setup consisted of a decellularized bone scaffold in an Ultem polyetherimide three-pronged winged bone holder (McMaster-Carr 7612K51) clamped in place with an O-ring. In this assembly, the height of the bone scaffold relative to its holder could be set to specify the thickness of the cartilage layer.

The cartilage region was sized to 2 mm thick (1 mm external to the scaffold with 1 mm penetrance into the bone) with a circular surface area 3.5 mm in diameter. For each scaffold, this corresponded to approximately 37 spherical CMBs 1 mm in diameter or 21 spherical CMBs 1.2 mm in diameter. The specific CMB diameter was measured prior to tissue seeding to account for some variability between batches.

The cartilage component of the tissue forming setup consisted of a white Teflon chamber to hold CMBs (McMaster-Carr 8545K1), an Ultem polyetherimide support piece (McMaster-Carr 7612K51) at the base of the chamber with 6 × 1 mm-diameter channels to allow nutrient exchange, and a porous hydrophobic polycarbonate track-etched membrane (1 μm pore size, Sterlitech) clamped between the body of the chamber and the supporting base. Once the appropriate number of CMBs were deposited into the chamber, the decellularized bone scaffold with predetermined height setting was pressed onto the cartilage layer.

The footprint of the cartilage-bone reactor was matched to a 24-well plate, with leftover working volume allowing the addition of sufficient media volume. From preliminary studies, it was determined that the CMBs needed 3 weeks in the confined culture setup to fuse and establish sufficient mechanical stability. During this time, complete chondrogenic medium containing TGF-β3 was changed twice weekly.

Subsequently, tissues were removed from confined culture within the cartilage chamber of the tissue forming setup. Within their bone holders, tissues were placed on top of Ultem polyetherimide suspension platforms (McMaster-Carr 7612K51) which allowed for free-swelling and light-accessible culture in black cover glass bottom 24-well cell imaging plates (Eppendorf). The superficial surface of the cartilage was oriented facing the bottom of the well such that it would receive the greatest light intensity when the well-plate was placed on top of the optogenetic stimulation device. Chondrogenic medium containing TGF-β3 was changed twice weekly.

5.5.4 Blue Light Optogenetic Stimulation

Blue light was delivered to the tissues long-term via an optogenetic stimulation device in a 24-well plate format, as previously designed **(Chapter 4).** The 488 nm light output at each position of the optogenetic stimulation device was measured with a handheld optical power and energy meter (THORLABS PM100D) with a photodiode power sensor (THORLABS S130VC) at the 0.5 mW setting. Parameters for the light stimulation device (3 μW/1.9 cm^2, 5-minute pulses every 2 hours) were determined based on prior studies **(Chapter 4)** and programmed in Arduino with the optoConfig graphical user interface [180].

5.5.5 Light Attenuation Measurements

For light attenuation measurements, tissues were fabricated in the same way except for an additional porous hydrophobic polytetrafluoroethylene laminated membrane (1 μm pore size, Sterlitech) separating the CMBs from the bone scaffold. Without direct bone ECM contact, CMBs were allowed to fuse to the best of their ability within the confined culture setup. After 3 weeks, the resulting cartilage disc was kept in the tissue forming chamber. To make the cartilage light-accessible from both ends, the supporting base and polycarbonate membrane were removed from the bottom of the assembly, and the bone in its holder and the polytetrafluoroethylene membrane were removed from the top of the assembly. The standalone cartilage disc within its chamber was transferred to a black 24-well cell imaging plate (Eppendorf) containing chondrogenic medium and a black Teflon photometer adapter (McMaster-Carr 8545K1) with a pinhole matched to the opening of the cartilage forming chamber. Light intensity was measured on the same optogenetic stimulation device and handheld optical power and energy meter (THORLABS PM100D) with a photodiode power sensor (THORLABS S130VC) at the 0.5 mW setting.

LEDs calibration values were measured directly over the optogenetic stimulation device. With everything but the cartilage, background readings were taken in the same configuration as the real measurements, with the 24-well plate, empty cartilage chamber, photometer pinhole adapter, and chondrogenic medium.

Table 5.1. Immunohistochemistry primary antibodies, human

anti-	Company	Catalog No.	Dilution
CILP	ThermoFisher	PA5-51856	1:500
Clusterin	Abcam	ab69644	1:100

Collagen X	Abcam	ab49945	1:1000
Lubricin	Abcam	ab28484	1:250

5.5.6 Histology and Immunohistochemistry

Tissues were fixed in 4% (v/v) paraformaldehyde overnight at 4°C, decalcified in OSTEOSOFT (Millipore Sigma) for 48 hours at room temperature on an orbital shaker, embedded in paraffin, and sectioned at 8 μm-thick. Some sections were stained with Alcian Blue (pH 2.5). For immunohistochemistry, paraffin-embedded sections were deparaffinized and rehydrated in Citrisolv (Fisher Scientific) followed by a graded ethanol series. Antigen retrieval was performed in citrate buffer (10 mM sodium citrate, pH 6.0) heated to boiling for 20 minutes and cooled for another 20 minutes, followed by incubation in ~700 U/mL hyaluronidase in PBS (Sigma) for 15 minutes at 37°C. Sections were permeabilized for 20 minutes at room temperature in 0.25% (v/v) Triton and 5% (v/v) serum. Blocking was done using 10% (v/v) serum for 2 hours at room temperature. Primary antibodies in blocking solution were incubated on samples overnight at 4°C (see **Table 5.1** for antibodies and their dilutions). To show the specificity of the antibody binding, negative controls were stained without primary antibodies. Subsequent steps with BLOXALL endogenous peroxidase quenching solution, biotinylated secondary antibody, ABC Reagent, and DAB Reagent were carried out per manufacturer's protocol (VECTASTAIN PK-8200; Vector Laboratories). Sections were dehydrated and cleared prior to mounting under cover glass with Permount (Fisher Scientific). High magnification images (20x) were taken of entire slides using the Olympus BX61VS.

5.5.7. Second Harmonic Generation Imaging

Unstained 8 μm-thick histological sections were deparaffinized and mounted under cover glass with Permount (Fisher Scientific). Second harmonic generation imaging was carried out on a multiphoton confocal microscope (Nikon A1RMP) with a fundamental laser excitation wavelength of 820 nm at laser power of 2978 mW. Acquired XY frames with 15% overlap were stitched together using the Nikon NIS-Elements ND Processing Stitch Multipoint to Large Image function.

Chapter 6: Summary and Future Directions

The overall goal of this dissertation was to introduce biologically inspired spatiotemporal cues to guide engineered cartilage formation. In **Aim 1,** we created patient-specific cartilage-bone constructs with native-like features at a clinical scale. We used decellularized bone matrix, autologous adipose-derived stem/stromal cells, and dual-chamber perfusion bioreactors to recapitulate the anatomy and zonal organization of the temporomandibular ramnus-condyle unit with its fibrocartilage. We established physiologically stiff, low friction cartilage as well as mature subchondral bone matrix after 6 months of orthotopic implantation in a human-sized swine model. Comparing the histological and functional properties at 5 weeks of *in vitro* culture versus 6 months post-implantation, we found that these cartilage-bone grafts served as templates for remodeling and regeneration, rather than immediate replicates and replacements of the native tissue. These studies validated key tissue engineering strategies for achieving *in vivo* cartilage regeneration.

To enable the precise *in vitro* study and manipulation of TGF-β signaling, a key pathway in cartilage development, in **Aim 2** we developed an optogenetic system for TGF-β signaling in human induced pluripotent stem cells that were subsequently differentiated into mesenchymal lineages. Using light-activated TGF-β signaling, we directed further differentiation into smooth muscle, tenogenic, and chondrogenic lineages without phototoxicity. This optogenetic platform served as a versatile tool for selectively activating TGF-β signaling with precise spatiotemporal control. Using these optogenetically edited cells in **Aim 3,** we sought to recapitulate physiological gradients of TGF-β signaling in a cartilage

layer interfaced with a bone substrate, towards engineering native-like cartilage tissues *in vitro*. To this end, we also created a light-accessible cartilage-bone reactor for optogenetic stimulation of the cells in three-dimensional settings. Optogenetic recapitulation of physiological spatiotemporal gradients of TGF-β signaling enabled the formation of stratified human cartilage integrated with the subchondral bone substrate, towards *in vitro* engineering of native-like, zonally organized articular cartilage.

United by the central theme of cartilage, this dissertation spanned three complementary and interacting areas of tissue engineering: regenerative medicine in **Aim 1,** tools and technological development in **Aim 2,** and organs on a chip in **Aim 3.** Alongside the original pillars of cells, scaffold, and environment, we propose this as another framework by which we can approach tissue engineering. We learned from **Aim 1** that *in vitro* engineered tissue serves as a template for tissue remodeling, rather than as a direct tissue replacement, leading to the regeneration of anatomically complex and large cartilage-bone grafts. The engineered tissue that was formed from young and healthy donor cells integrated and functioned in the *in vivo* environment of the highly loaded temporomandibular joint. Future implantation studies with more organized tissues developed from the work of **Aims 2 and 3** could help investigate the potential of stratified cartilage-bone tissues engineered *in vitro* for enhancing and accelerating regeneration *in vivo,* particularly in the challenging environments associated with disease.

Though the goal of engineering fully functional cartilage has been decades in the making, perhaps an early target of tissue engineering due to its deceptive simplicity, we still are unable to produce cartilage with fully biomimetic architectures, mechanical properties,

and physiological function. With implanted grafts, we rely on physiological signals and regenerative processes *in vivo* to bring engineered tissues towards a native-like state. These same fundamental problems underlie the engineering of all tissues, and effective new approaches are required for the field to advance.

This dissertation was centered around cartilage tissue engineering strategies, but the findings and suite of tools developed are not limited to cartilage alone. For example, the tools developed in **Aim 2** and **Aim 3** can inform the development of optogenetic platforms for modeling the neuromuscular junction or cardiac muscle, delineate the contributions of various cell types or matrix properties to tissue fibrosis, or be used to study the maintenance versus activation of stromal/stem cell-like niches in biological scenarios such as arteriogenesis or bone injury.

Ultimately, we return to the paradigm that cells are the true tissue engineers. Valuable insights on how to mobilize their regenerative potential will come with the rapid progress of recent years in related fields such as stem cell biology, imaging, and high throughput -omics sequencing. These ongoing research efforts will help to advance cartilage tissue engineering and offer novel solutions for joint disease.

References

[1] D.J. Hunter, L. March, M. Chew, Osteoarthritis in 2020 and beyond: a Lancet Commission, The Lancet. 396 (2020) 1711–1712. https://doi.org/10.1016/S0140-6736(20)32230-3.

[2] E. Losina, A.D. Paltiel, A.M. Weinstein, E. Yelin, D.J. Hunter, S.P. Chen, K. Klara, L.G. Suter, D.H. Solomon, S.A. Burbine, R.P. Walensky, J.N. Katz, Lifetime medical costs of knee osteoarthritis management in the United States: impact of extending indications for total knee arthroplasty, Arthritis Care Res. 67 (2015) 203–215. https://doi.org/10.1002/acr.22412.

[3] R.J. Williams, ed., Cartilage Repair Strategies, Humana Press, 2007. https://doi.org/10.1007/978-1-59745-343-1.

[4] S.R. Tew, A.P.L. Kwan, A. Hann, B.M. Thomson, C.W. Archer, The reactions of articular cartilage to experimental wounding: Role of apoptosis, Arthritis & Rheumatism. 43 (2000) 215–225. https://doi.org/10.1002/1529-0131(200001)43:1<215::AID-ANR26>3.0.CO;2-X.

[5] A. Ghouri, P.G. Conaghan, Update on novel pharmacological therapies for osteoarthritis, Ther Adv Musculoskelet Dis. 11 (2019) 1759720X19864492. https://doi.org/10.1177/1759720X19864492.

[6] C.I. Johnson, D.J. Argyle, D.N. Clements, In vitro models for the study of osteoarthritis, The Veterinary Journal. 209 (2016) 40–49. https://doi.org/10.1016/j.tvjl.2015.07.011.

[7] D.B.F. Saris, J. Vanlauwe, J. Victor, K.F. Almqvist, R. Verdonk, J. Bellemans, F.P. Luyten, Treatment of Symptomatic Cartilage Defects of the Knee: Characterized Chondrocyte Implantation Results in Better Clinical Outcome at 36 Months in a Randomized Trial Compared to Microfracture, Am J Sports Med. 37 (2009) 10–19. https://doi.org/10.1177/0363546509350694.

[8] B.A. Byers, R.L. Mauck, I.E. Chiang, R.S. Tuan, Transient Exposure to Transforming Growth Factor Beta 3 Under Serum-Free Conditions Enhances the Biomechanical and Biochemical Maturation of Tissue-Engineered Cartilage, Tissue Eng Part A. 14 (2008) 1821–1834. https://doi.org/10.1089/ten.tea.2007.0222.

[9] C. Scotti, B. Tonnarelli, A. Papadimitropoulos, A. Scherberich, S. Schaeren, A. Schauerte, J. Lopez-Rios, R. Zeller, A. Barbero, I. Martin, Recapitulation of endochondral bone formation using human adult mesenchymal stem cells as a paradigm for developmental engineering, Proceedings of the National Academy of Sciences of the United States of America. 107 (2010) 7251. https://doi.org/10.1073/pnas.1000302107.

[10] K. Pelttari, A. Winter, E. Steck, K. Goetzke, T. Hennig, B.G. Ochs, T. Aigner, W. Richter, Premature induction of hypertrophy during in vitro chondrogenesis of human mesenchymal stem cells correlates with calcification and vascular invasion after ectopic transplantation in SCID mice, Arthritis & Rheumatism. 54 (2006) 3254–3266. https://doi.org/10.1002/art.22136.

[11] Y. Li, M. Lee, N. Kim, G. Wu, D. Deng, J.M. Kim, X. Liu, W.D. Heo, Z. Zi, Spatiotemporal Control of TGF-β Signaling with Light, ACS Synth. Biol. 7 (2018) 443–451. https://doi.org/10.1021/acssynbio.7b00225.

[12] S. Bhumiratana, R.E. Eton, S.R. Oungoulian, L.Q. Wan, G.A. Ateshian, G. Vunjak-Novakovic, Large, stratified, and mechanically functional human cartilage grown in vitro by mesenchymal condensation, Proc Natl Acad Sci U S A. 111 (2014) 6940–6945. https://doi.org/10.1073/pnas.1324050111.
[13] S. Bhumiratana, G. Vunjak-Novakovic, Engineering physiologically stiff and stratified human cartilage by fusing condensed mesenchymal stem cells, Methods. 84 (2015) 109–114. https://doi.org/10.1016/j.ymeth.2015.03.016.
[14] Z. Lin, Z. Li, E.N. Li, X. Li, C.J. Del Duke, H. Shen, T. Hao, B. O'Donnell, B.A. Bunnell, S.B. Goodman, P.G. Alexander, R.S. Tuan, H. Lin, Osteochondral Tissue Chip Derived From iPSCs: Modeling OA Pathologies and Testing Drugs, Front. Bioeng. Biotechnol. 7 (2019) 411. https://doi.org/10.3389/fbioe.2019.00411.
[15] K.E. Barbour, Vital Signs: Prevalence of Doctor-Diagnosed Arthritis and Arthritis-Attributable Activity Limitation — United States, 2013–2015, MMWR Morb Mortal Wkly Rep. 66 (2017). https://doi.org/10.15585/mmwr.mm6609e1.
[16] J.M. Hootman, C.G. Helmick, K.E. Barbour, K.A. Theis, M.A. Boring, Updated Projected Prevalence of Self-Reported Doctor-Diagnosed Arthritis and Arthritis-Attributable Activity Limitation Among US Adults, 2015-2040, Arthritis & Rheumatology (Hoboken, N.J.). 68 (2016) 1582–1587. https://doi.org/10.1002/art.39692.
[17] TMJ (Temporomandibular Joint and Muscle Disorders) Causes, Symptoms, Diagnosis, Treatment | National Institute of Dental and Craniofacial Research, (n.d.). https://www.nidcr.nih.gov/health-info/tmj/more-info (accessed February 18, 2020).
[18] M.J. Troulis, F.T. Tayebaty, M. Papadaki, W.B. Williams, L.B. Kaban, Condylectomy and costochondral graft reconstruction for treatment of active idiopathic condylar resorption, J. Oral Maxillofac. Surg. 66 (2008) 65–72. https://doi.org/10.1016/j.joms.2007.08.030.
[19] C. Di Blasio, A. Di Blasio, G. Pedrazzi, M. Anghinoni, E. Sesenna, How Does the Mandible Grow After Early High Condylectomy?, Journal of Craniofacial Surgery. 26 (2015) 764–771. https://doi.org/10.1097/SCS.0000000000001515.
[20] R. Fariña, S. Olate, A. Raposo, I. Araya, J.P. Alister, F. Uribe, High condylectomy versus proportional condylectomy: is secondary orthognathic surgery necessary?, International Journal of Oral and Maxillofacial Surgery. 45 (2016) 72–77. https://doi.org/10.1016/j.ijom.2015.07.016.
[21] S. Ghawsi, E. Aagaard, T.H. Thygesen, High condylectomy for the treatment of mandibular condylar hyperplasia: a systematic review of the literature, International Journal of Oral and Maxillofacial Surgery. 45 (2016) 60–71. https://doi.org/10.1016/j.ijom.2015.09.002.
[22] C.P. Saridin, M. Gilijamse, D.J. Kuik, E.C. te Veldhuis, D.B. Tuinzing, F. Lobbezoo, A.G. Becking, Evaluation of Temporomandibular Function After High Partial Condylectomy Because of Unilateral Condylar Hyperactivity, Journal of Oral and Maxillofacial Surgery. 68 (2010) 1094–1099. https://doi.org/10.1016/j.joms.2009.09.105.
[23] M. Bak, A.S. Jacobson, D. Buchbinder, M.L. Urken, Contemporary reconstruction of the mandible, Oral Oncology. 46 (2010) 71–76. https://doi.org/10.1016/j.oraloncology.2009.11.006.

[24] C. Schrag, Y.-M. Chang, C.-Y. Tsai, F.-C. Wei, Complete rehabilitation of the mandible following segmental resection, Journal of Surgical Oncology. 94 (2006) 538–545. https://doi.org/10.1002/jso.20491.
[25] R.M. Smith, M.S. Goldwasser, S.R. Sabol, Erosion of a Teflon-Proplast implant into the middle cranial fossa, Journal of Oral and Maxillofacial Surgery. 51 (1993) 1268–1271. https://doi.org/10.1016/S0278-2391(10)80300-3.
[26] S. Abramowicz, M.F. Dolwick, S.B. Lewis, C. Dolce, Temporomandibular joint reconstruction after failed teflon-proplast implant: case report and literature review, International Journal of Oral and Maxillofacial Surgery. 37 (2008) 763–767. https://doi.org/10.1016/j.ijom.2008.02.006.
[27] A. Boyo, J. McKay, G. Lebovic, D.J. Psutka, Temporomandibular joint total replacement using the Zimmer Biomet Microfixation patient-matched prosthesis results in reduced pain and improved function, Oral Surgery, Oral Medicine, Oral Pathology and Oral Radiology. 128 (2019) 572–580. https://doi.org/10.1016/j.oooo.2019.04.012.
[28] L. Zou, L. Zhang, D. He, C. Yang, J. Zhao, E. Ellis, Clinical and Radiologic Follow-Up of Zimmer Biomet Stock Total Temporomandibular Joint Replacement After Surgical Modifications, Journal of Oral and Maxillofacial Surgery. 76 (2018) 2518–2524. https://doi.org/10.1016/j.joms.2018.06.013.
[29] J. Thyssen, T. Menné, Metal Allergy-A Review on Exposures, Penetration, Genetics, Prevalence, and Clinical Implications, Chemical Research in Toxicology. 23 (2009) 309–18. https://doi.org/10.1021/tx9002726.
[30] S. Hassan, L.G. Mercuri, M. Miloro, Does Metal Hypersensitivity Have Relevance in Patients Undergoing TMJ Prosthetic Replacement?, Journal of Oral and Maxillofacial Surgery. 78 (2020) 908–915. https://doi.org/10.1016/j.joms.2020.01.020.
[31] B.J. Bielajew, R.P. Donahue, M.G. Espinosa, B. Arzi, D. Wang, D.C. Hatcher, N.K. Paschos, M.E.K. Wong, J.C. Hu, K.A. Athanasiou, Knee orthopedics as a template for the temporomandibular joint, Cell Reports Medicine. 2 (2021) 100241. https://doi.org/10.1016/j.xcrm.2021.100241.
[32] E.A. Makris, A.H. Gomoll, K.N. Malizos, J.C. Hu, K.A. Athanasiou, Repair and tissue engineering techniques for articular cartilage, Nat Rev Rheumatol. 11 (2015) 21–34. https://doi.org/10.1038/nrrheum.2014.157.
[33] D.K. Bae, K.H. Yoon, S.J. Song, Cartilage Healing After Microfracture in Osteoarthritic Knees, Arthroscopy: The Journal of Arthroscopic & Related Surgery. 22 (2006) 367–374. https://doi.org/10.1016/j.arthro.2006.01.015.
[34] K. Mithoefer, T. McAdams, R.J. Williams, P.C. Kreuz, B.R. Mandelbaum, Clinical Efficacy of the Microfracture Technique for Articular Cartilage Repair in the Knee: An Evidence-Based Systematic Analysis, Am J Sports Med. 37 (2009) 2053–2063. https://doi.org/10.1177/0363546508328414.
[35] D. Goyal, S. Keyhani, E.H. Lee, J.H.P. Hui, Evidence-Based Status of Microfracture Technique: A Systematic Review of Level I and II Studies, Arthroscopy: The Journal of Arthroscopic & Related Surgery. 29 (2013) 1579–1588. https://doi.org/10.1016/j.arthro.2013.05.027.

[36] A. Ng, K. Bernhard, Osteochondral Autograft and Allograft Transplantation in the Talus, Clin Podiatr Med Surg. 34 (2017) 461–469. https://doi.org/10.1016/j.cpm.2017.05.004.
[37] J.R. Salash, R.H. Hossameldin, A.J. Almarza, J.C. Chou, J.P. McCain, L.G. Mercuri, L.M. Wolford, M.S. Detamore, Potential Indications for Tissue Engineering in Temporomandibular Joint Surgery, Journal of Oral and Maxillofacial Surgery. 74 (2016) 705–711. https://doi.org/10.1016/j.joms.2015.11.008.
[38] T.L. Vincent, R.O. Williams, R. Maciewicz, A. Silman, P. Garside, Mapping pathogenesis of arthritis through small animal models, Rheumatology (Oxford). 51 (2012) 1931–1941. https://doi.org/10.1093/rheumatology/kes035.
[39] S.S. Glasson, M.G. Chambers, W.B. Van Den Berg, C.B. Little, The OARSI histopathology initiative – recommendations for histological assessments of osteoarthritis in the mouse, Osteoarthritis and Cartilage. 18 (2010) S17–S23. https://doi.org/10.1016/j.joca.2010.05.025.
[40] S. Thysen, F.P. Luyten, R.J.U. Lories, Targets, models and challenges in osteoarthritis research, Dis Model Mech. 8 (2015) 17–30. https://doi.org/10.1242/dmm.016881.
[41] R. Krishnan, S. Park, F. Eckstein, G.A. Ateshian, Inhomogeneous Cartilage Properties Enhance Superficial Interstitial Fluid Support and Frictional Properties, But Do Not Provide a Homogeneous State of Stress, J Biomech Eng. 125 (2003) 569–577. https://doi.org/10.1115/1.1610018.
[42] S.R. Goldring, Role of Bone in Osteoarthritis Pathogenesis, Medical Clinics of North America. 93 (2009) 25–35. https://doi.org/10.1016/j.mcna.2008.09.006.
[43] S.M. Goldman, G.A. Barabino, Spatial Engineering of Osteochondral Tissue Constructs Through Microfluidically Directed Differentiation of Mesenchymal Stem Cells, BioResearch Open Access. 5 (2016) 109–117. https://doi.org/10.1089/biores.2016.0005.
[44] M. Singh, M.S. Detamore, Biomechanical properties of the mandibular condylar cartilage and their relevance to the TMJ disc, Journal of Biomechanics. 42 (2009) 405–417. https://doi.org/10.1016/j.jbiomech.2008.12.012.
[45] G. Man, G. Mologhianu, Osteoarthritis pathogenesis – a complex process that involves the entire joint, J Med Life. 7 (2014) 37–41.
[46] R.F. Loeser, S.R. Goldring, C.R. Scanzello, M.B. Goldring, Osteoarthritis: A disease of the joint as an organ, Arthritis & Rheumatism. 64 (2012) 1697–1707. https://doi.org/10.1002/art.34453.
[47] J. Smeeton, A. Askary, J.G. Crump, Building and maintaining joints by exquisite local control of cell fate, WIREs Developmental Biology. 6 (2017) e245. https://doi.org/10.1002/wdev.245.
[48] D. Giovannone, S. Paul, S. Schindler, C. Arata, D.T. Farmer, P. Patel, J. Smeeton, J.G. Crump, Programmed conversion of hypertrophic chondrocytes into osteoblasts and marrow adipocytes within zebrafish bones, ELife. 8 (2019) e42736. https://doi.org/10.7554/eLife.42736.
[49] A.J. Engler, S. Sen, H.L. Sweeney, D.E. Discher, Matrix elasticity directs stem cell lineage specification, Cell. 126 (2006) 677–689. https://doi.org/10.1016/j.cell.2006.06.044.

[50] P.D. Benya, J.D. Shaffer, Dedifferentiated chondrocytes reexpress the differentiated collagen phenotype when cultured in agarose gels, Cell. 30 (1982) 215–224. https://doi.org/10.1016/0092-8674(82)90027-7.
[51] N. Zhou, Q. Li, X. Lin, N. Hu, J.-Y. Liao, L.-B. Lin, C. Zhao, Z.-M. Hu, X. Liang, W. Xu, H. Chen, W. Huang, BMP2 induces chondrogenic differentiation, osteogenic differentiation and endochondral ossification in stem cells, Cell Tissue Res. 366 (2016) 101–111. https://doi.org/10.1007/s00441-016-2403-0.
[52] M.B. Albro, R.J. Nims, K.M. Durney, A.D. Cigan, J.J. Shim, G. Vunjak-Novakovic, C.T. Hung, G.A. Ateshian, Heterogeneous engineered cartilage growth results from gradients of media-supplemented active TGF-β and is ameliorated by the alternative supplementation of latent TGF-β, Biomaterials. 77 (2016) 173–185. https://doi.org/10.1016/j.biomaterials.2015.10.018.
[53] A.D. Cigan, R.J. Nims, G. Vunjak-Novakovic, C.T. Hung, G.A. Ateshian, Optimizing nutrient channel spacing and revisiting TGF-beta in large engineered cartilage constructs, Journal of Biomechanics. 49 (2016) 2089–2094. https://doi.org/10.1016/j.jbiomech.2016.05.020.
[54] J.J. Ng, Y. Wei, B. Zhou, J. Bernhard, S. Robinson, A. Burapachaisri, X.E. Guo, G. Vunjak-Novakovic, Recapitulation of physiological spatiotemporal signals promotes in vitro formation of phenotypically stable human articular cartilage, Proc Natl Acad Sci U S A. 114 (2017) 2556–2561. https://doi.org/10.1073/pnas.1611771114.
[55] J.J. Wood, M.A. Malek, F.J. Frassica, J.A. Polder, A.K. Mohan, E.T. Bloom, M.M. Braun, T.R. Coté, Autologous Cultured Chondrocytes: Adverse Events Reported to the United States Food and Drug Administration, JBJS. 88 (2006) 503–507. https://doi.org/10.2106/JBJS.E.00103.
[56] L. Acevedo Rua, M. Mumme, C. Manferdini, S. Darwiche, A. Khalil, M. Hilpert, D.A. Buchner, G. Lisignoli, P. Occhetta, B. von Rechenberg, M. Haug, D.J. Schaefer, M. Jakob, A. Caplan, I. Martin, A. Barbero, K. Pelttari, Engineered nasal cartilage for the repair of osteoarthritic knee cartilage defects, Science Translational Medicine. 13 (2021) eaaz4499. https://doi.org/10.1126/scitranslmed.aaz4499.
[57] D. Chen, J.Y. Wu, K.M. Kennedy, K. Yeager, J.C. Bernhard, J.J. Ng, B.K. Zimmerman, S. Robinson, K.M. Durney, C. Shaeffer, O.F. Vila, C. Takawira, J.M. Gimble, X.E. Guo, G.A. Ateshian, M.J. Lopez, S.B. Eisig, G. Vunjak-Novakovic, Tissue engineered autologous cartilage-bone grafts for temporomandibular joint regeneration, Science Translational Medicine. 12 (2020) eabb6683. https://doi.org/10.1126/scitranslmed.abb6683.
[58] V.V. Meretoja, R.L. Dahlin, F.K. Kasper, A.G. Mikos, Enhanced chondrogenesis in co-cultures with articular chondrocytes and mesenchymal stem cells, Biomaterials. 33 (2012) 6362–6369. https://doi.org/10.1016/j.biomaterials.2012.05.042.
[59] M. Kim, M.J. Farrell, D.R. Steinberg, J.A. Burdick, R.L. Mauck, Enhanced Nutrient Transport Improves the Depth-Dependent Properties of Tri-Layered Engineered Cartilage Constructs with Zonal Co-Culture of Chondrocytes and MSCs, Acta Biomater. 58 (2017) 1–11. https://doi.org/10.1016/j.actbio.2017.06.025.
[60] V. Zhukareva, M. Obrocka, J.D. Houle, I. Fischer, B. Neuhuber, Secretion profile of human bone marrow stromal cells: Donor variability and response to inflammatory stimuli, Cytokine. 50 (2010) 317–321. https://doi.org/10.1016/j.cyto.2010.01.004.

[61] H. Mizuno, M. Tobita, A.C. Uysal, Concise Review: Adipose-Derived Stem Cells as a Novel Tool for Future Regenerative Medicine, Stem Cells. 30 (2012) 804–810. https://doi.org/10.1002/stem.1076.
[62] M. Dominici, K. Le Blanc, I. Mueller, I. Slaper-Cortenbach, F.C. Marini, D.S. Krause, R.J. Deans, A. Keating, D.J. Prockop, E.M. Horwitz, Minimal criteria for defining multipotent mesenchymal stromal cells. The International Society for Cellular Therapy position statement, Cytotherapy. 8 (2006) 315–317. https://doi.org/10.1080/14653240600855905.
[63] M. Xu, G. Shaw, M. Murphy, F. Barry, Induced Pluripotent Stem Cell-Derived Mesenchymal Stromal Cells Are Functionally and Genetically Different From Bone Marrow-Derived Mesenchymal Stromal Cells, Stem Cells. 37 (2019) 754–765. https://doi.org/10.1002/stem.2993.
[64] A.M. Craft, J.S. Rockel, Y. Nartiss, R.A. Kandel, B.A. Alman, G.M. Keller, Generation of articular chondrocytes from human pluripotent stem cells, Nat Biotechnol. 33 (2015) 638–645. https://doi.org/10.1038/nbt.3210.
[65] C.-L. Wu, A. Dicks, N. Steward, R. Tang, D.B. Katz, Y.-R. Choi, F. Guilak, Single cell transcriptomic analysis of human pluripotent stem cell chondrogenesis, Nat Commun. 12 (2021) 362. https://doi.org/10.1038/s41467-020-20598-y.
[66] A. Rodríguez Ruiz, A. Dicks, M. Tuerlings, K. Schepers, M. van Pel, R.G.H.H. Nelissen, C. Freund, C.L. Mummery, V. Orlova, F. Guilak, I. Meulenbelt, Y.F.M. Ramos, Cartilage from human-induced pluripotent stem cells: comparison with neo-cartilage from chondrocytes and bone marrow mesenchymal stromal cells, Cell Tissue Res. 386 (2021) 309–320. https://doi.org/10.1007/s00441-021-03498-5.
[67] S.S. Adkar, C.-L. Wu, V.P. Willard, A. Dicks, A. Ettyreddy, N. Steward, N. Bhutani, C.A. Gersbach, F. Guilak, Step-Wise Chondrogenesis of Human Induced Pluripotent Stem Cells and Purification Via a Reporter Allele Generated by CRISPR-Cas9 Genome Editing, STEM CELLS. 37 (2019) 65–76. https://doi.org/10.1002/stem.2931.
[68] S. Pigeot, T. Klein, F. Gullotta, S.J. Dupard, A. Garcia Garcia, A. García-García, S. Prithiviraj, P. Lorenzo, M. Filippi, C. Jaquiery, L. Kouba, M.A. Asnaghi, D.B. Raina, B. Dasen, H. Isaksson, P. Önnerfjord, M. Tägil, A. Bondanza, I. Martin, P.E. Bourgine, Manufacturing of Human Tissues as off-the-Shelf Grafts Programmed to Induce Regeneration, Advanced Materials. 33 (2021) 2103737. https://doi.org/10.1002/adma.202103737.
[69] C.I. Seidl, T.A. Fulga, C.L. Murphy, CRISPR-Cas9 targeting of MMP13 in human chondrocytes leads to significantly reduced levels of the metalloproteinase and enhanced type II collagen accumulation, Osteoarthritis and Cartilage. 27 (2019) 140–147. https://doi.org/10.1016/j.joca.2018.09.001.
[70] J.M. Brunger, A. Zutshi, V.P. Willard, C.A. Gersbach, F. Guilak, CRISPR/Cas9 Editing of Murine Induced Pluripotent Stem Cells for Engineering Inflammation-Resistant Tissues, Arthritis & Rheumatology. 69 (2017) 1111–1121. https://doi.org/10.1002/art.39982.
[71] T.-K. Kim, B. Sharma, C.G. Williams, M.A. Ruffner, A. Malik, E.G. McFarland, J.H. Elisseeff, Experimental Model for Cartilage Tissue Engineering to Regenerate the Zonal Organization of Articular Cartilage, Osteoarthritis and Cartilage. 11 (2003) 653–664. https://doi.org/10.1016/S1063-4584(03)00120-1.

[72] T.J. Klein, B.L. Schumacher, T.A. Schmidt, K.W. Li, M.S. Voegtline, K. Masuda, E.J.-M.A. Thonar, R.L. Sah, Tissue engineering of stratified articular cartilage from chondrocyte subpopulations, Osteoarthritis and Cartilage. 11 (2003) 595–602. https://doi.org/10.1016/S1063-4584(03)00090-6.
[73] G.N. Hall, W.L. Tam, K.S. Andrikopoulos, L. Casas-Fraile, G.A. Voyiatzis, L. Geris, F.P. Luyten, I. Papantoniou, Patterned, organoid-based cartilaginous implants exhibit zone specific functionality forming osteochondral-like tissues in vivo, Biomaterials. 273 (2021) 120820. https://doi.org/10.1016/j.biomaterials.2021.120820.
[74] S.-S. Seo, C.-W. Kim, D.-W. Jung, Management of Focal Chondral Lesion in the Knee Joint, Knee Surg Relat Res. 23 (2011) 185–196. https://doi.org/10.5792/ksrr.2011.23.4.185.
[75] H. Clevers, Modeling Development and Disease with Organoids, Cell. 165 (2016) 1586–1597. https://doi.org/10.1016/j.cell.2016.05.082.
[76] S.K. O'Connor, D.B. Katz, S.J. Oswald, L. Groneck, F. Guilak, Formation of Osteochondral Organoids from Murine Induced Pluripotent Stem Cells, Tissue Engineering Part A. 27 (2021) 1099–1109. https://doi.org/10.1089/ten.tea.2020.0273.
[77] K.W. Ng, C.C.-B. Wang, R.L. Mauck, T.-A.N. Kelly, N.O. Chahine, K.D. Costa, G.A. Ateshian, C.T. Hung, A layered agarose approach to fabricate depth-dependent inhomogeneity in chondrocyte-seeded constructs, Journal of Orthopaedic Research. 23 (2005) 134–141. https://doi.org/10.1016/j.orthres.2004.05.015.
[78] S.D. McCullen, H. Autefage, A. Callanan, E. Gentleman, M.M. Stevens, Anisotropic Fibrous Scaffolds for Articular Cartilage Regeneration, Tissue Engineering Part A. 18 (2012) 2073–2083. https://doi.org/10.1089/ten.tea.2011.0606.
[79] G.M. Cunniffe, P.J. Díaz-Payno, E.J. Sheehy, S.E. Critchley, H.V. Almeida, P. Pitacco, S.F. Carroll, O.R. Mahon, A. Dunne, T.J. Levingstone, C.J. Moran, R.T. Brady, F.J. O'Brien, P.A.J. Brama, D.J. Kelly, Tissue-specific extracellular matrix scaffolds for the regeneration of spatially complex musculoskeletal tissues, Biomaterials. 188 (2019) 63–73. https://doi.org/10.1016/j.biomaterials.2018.09.044.
[80] J.A.M. Steele, A.C. Moore, J.-P. St-Pierre, S.D. McCullen, A.J. Gormley, C.C. Horgan, C.RM. Black, C. Meinert, T. Klein, S. Saifzadeh, R. Steck, J. Ren, M.A. Woodruff, M.M. Stevens, In vitro and in vivo investigation of a zonal microstructured scaffold for osteochondral defect repair, Biomaterials. (2022) 121548. https://doi.org/10.1016/j.biomaterials.2022.121548.
[81] P. Camacho, A. Behre, M. Fainor, K.B. Seims, L.W. Chow, Spatial organization of biochemical cues in 3D-printed scaffolds to guide osteochondral tissue engineering, Biomater. Sci. 9 (2021) 6813–6829. https://doi.org/10.1039/D1BM00859E.
[82] F.E. Freeman, P. Pitacco, L.H.A. van Dommelen, J. Nulty, D.C. Browe, J.-Y. Shin, E. Alsberg, D.J. Kelly, 3D bioprinting spatiotemporally defined patterns of growth factors to tightly control tissue regeneration, Science Advances. 6 (n.d.) eabb5093. https://doi.org/10.1126/sciadv.abb5093.
[83] H. Lin, T.P. Lozito, P.G. Alexander, R. Gottardi, R.S. Tuan, Stem Cell-Based Microphysiological Osteochondral System to Model Tissue Response to Interleukin-1β, Mol. Pharmaceutics. 11 (2014) 2203–2212. https://doi.org/10.1021/mp500136b.

[84] C. Li, L. Ouyang, I.J. Pence, A.C. Moore, Y. Lin, C.W. Winter, J.P.K. Armstrong, M.M. Stevens, Buoyancy-Driven Gradients for Biomaterial Fabrication and Tissue Engineering, Advanced Materials. 31 (2019) 1900291. https://doi.org/10.1002/adma.201900291.
[85] C. Li, J.PK. Armstrong, I.J. Pence, W. Kit-Anan, J.L. Puetzer, S. Correia Carreira, A.C. Moore, M.M. Stevens, Glycosylated superparamagnetic nanoparticle gradients for osteochondral tissue engineering, Biomaterials. 176 (2018) 24–33. https://doi.org/10.1016/j.biomaterials.2018.05.029.
[86] H.M. Zlotnick, A.T. Clark, S.E. Gullbrand, J.L. Carey, X.M. Cheng, R.L. Mauck, Magneto-Driven Gradients of Diamagnetic Objects for Engineering Complex Tissues, Advanced Materials. n/a (n.d.) 2005030. https://doi.org/10.1002/adma.202005030.
[87] W. Wang, D. Huang, J. Ren, R. Li, Z. Feng, C. Guan, B. Bao, B. Cai, J. Ling, C. Zhou, Optogenetic control of mesenchymal cell fate towards precise bone regeneration, Theranostics. 9 (2019) 8196–8205. https://doi.org/10.7150/thno.36455.
[88] J.P.K. Armstrong, M.M. Stevens, Using Remote Fields for Complex Tissue Engineering, Trends in Biotechnology. 38 (2020) 254–263. https://doi.org/10.1016/j.tibtech.2019.07.005.
[89] B.R. Stockwell, S.L. Schreiber, Probing the role of homomeric and heteromeric receptor interactions in TGF-β signaling using small molecule dimerizers, Current Biology. 8 (1998) 761–773. https://doi.org/10.1016/S0960-9822(98)70299-4.
[90] D. Qu, J.P. Zhu, H.R. Childs, H.H. Lu, Nanofiber-based transforming growth factor-β3 release induces fibrochondrogenic differentiation of stem cells, Acta Biomaterialia. 93 (2019) 111–122. https://doi.org/10.1016/j.actbio.2019.03.019.
[91] L.J. Bugaj, A.T. Choksi, C.K. Mesuda, R.S. Kane, D.V. Schaffer, Optogenetic protein clustering and signaling activation in mammalian cells, Nat Methods. 10 (2013) 249–252. https://doi.org/10.1038/nmeth.2360.
[92] A.M. Tatara, G.L. Koons, E. Watson, T.C. Piepergerdes, S.R. Shah, B.T. Smith, J. Shum, J.C. Melville, I.A. Hanna, N. Demian, T. Ho, A. Ratcliffe, J.J.J.P. van den Beucken, J.A. Jansen, M.E. Wong, A.G. Mikos, Biomaterials-aided mandibular reconstruction using in vivo bioreactors, PNAS. 116 (2019) 6954–6963. https://doi.org/10.1073/pnas.1819246116.
[93] O. Guillaume, M.A. Geven, V. Varjas, P. Varga, D. Gehweiler, V.A. Stadelmann, T. Smidt, S. Zeiter, C. Sprecher, R.R.M. Bos, D.W. Grijpma, M. Alini, H. Yuan, G.R. Richards, T. Tang, L. Qin, L. Yuxiao, P. Jiang, D. Eglin, Orbital floor repair using patient specific osteoinductive implant made by stereolithography, Biomaterials. 233 (2020) 119721. https://doi.org/10.1016/j.biomaterials.2019.119721.
[94] S. Bhumiratana, J.C. Bernhard, D.M. Alfi, K. Yeager, R.E. Eton, J. Bova, F. Shah, J.M. Gimble, M.J. Lopez, S.B. Eisig, G. Vunjak-Novakovic, Tissue-engineered autologous grafts for facial bone reconstruction, Science Translational Medicine. 8 (2016) 343ra83-343ra83. https://doi.org/10.1126/scitranslmed.aad5904.
[95] M.E. Elsalanty, D.G. Genecov, Bone Grafts in Craniofacial Surgery, Craniomaxillofac Trauma Reconstr. 2 (2009) 125–134. https://doi.org/10.1055/s-0029-1215875.
[96] S. Bhumiratana, R.E. Eton, S.R. Oungoulian, L.Q. Wan, G.A. Ateshian, G. Vunjak-Novakovic, Large, stratified, and mechanically functional human cartilage grown in

vitro by mesenchymal condensation, PNAS. 111 (2014) 6940–6945. https://doi.org/10.1073/pnas.1324050111.
[97] S. Bhumiratana, G. Vunjak-Novakovic, Engineering physiologically stiff and stratified human cartilage by fusing condensed mesenchymal stem cells, Methods. 84 (2015) 109–114. https://doi.org/10.1016/j.ymeth.2015.03.016.
[98] X. Nie, Y.J. Chuah, W. Zhu, P. He, Y. Peck, D.-A. Wang, Decellularized tissue engineered hyaline cartilage graft for articular cartilage repair, Biomaterials. 235 (2020) 119821. https://doi.org/10.1016/j.biomaterials.2020.119821.
[99] M.J. Troulis, J. Glowacki, D.H. Perrott, L.B. Kaban, Effects of latency and rate on bone formation in a porcine mandibular distraction model, Journal of Oral and Maxillofacial Surgery. 58 (2000) 507–513. https://doi.org/10.1016/S0278-2391(00)90012-0.
[100] H. Abukawa, H. Terai, D. Hannouche, J.P. Vacanti, L.B. Kaban, M.J. Troulis, Formation of a mandibular condyle in vitro by tissue engineering, Journal of Oral and Maxillofacial Surgery. 61 (2003) 94–100. https://doi.org/10.1053/joms.2003.50015.
[101] A.J. Almarza, B.N. Brown, B. Arzi, D.F. Ângelo, W. Chung, S.F. Badylak, M. Detamore, Preclinical Animal Models for Temporomandibular Joint Tissue Engineering, Tissue Engineering Part B: Reviews. 24 (2017) 171–178. https://doi.org/10.1089/ten.teb.2017.0341.
[102] W.L. Grayson, D. Marolt, S. Bhumiratana, M. Fröhlich, E. Guo, G. Vunjak-Novakovic, Optimizing the medium perfusion rate in bone tissue engineering bioreactors, Biotechnol Bioeng. 108 (2011). https://doi.org/10.1002/bit.23024.
[103] S. Bhumiratana, J.C. Bernhard, D.M. Alfi, K. Yeager, R.E. Eton, J. Bova, F. Shah, J.M. Gimble, M.J. Lopez, S.B. Eisig, G. Vunjak-Novakovic, Tissue-engineered autologous grafts for facial bone reconstruction, Sci. Transl. Med. 8 (2016) 343ra83-343ra83. https://doi.org/10.1126/scitranslmed.aad5904.
[104] S.D. Waldman, C.G. Spiteri, M.D. Grynpas, R.M. Pilliar, R.A. Kandel, Long-term intermittent shear deformation improves the quality of cartilaginous tissue formed in vitro, Journal of Orthopaedic Research. 21 (2003) 590–596. https://doi.org/10.1016/S0736-0266(03)00009-3.
[105] W.L. Grayson, D. Marolt, S. Bhumiratana, M. Fröhlich, X.E. Guo, G. Vunjak-Novakovic, Optimizing the medium perfusion rate in bone tissue engineering bioreactors, Biotechnology and Bioengineering. 108 (2011) 1159–1170. https://doi.org/10.1002/bit.23024.
[106] L. Ruggiero, B.K. Zimmerman, M. Park, L. Han, L. Wang, D.L. Burris, X.L. Lu, Roles of the Fibrous Superficial Zone in the Mechanical Behavior of TMJ Condylar Cartilage, Ann Biomed Eng. 43 (2015) 2652–2662. https://doi.org/10.1007/s10439-015-1320-9.
[107] M.M. Stevens, R.P. Marini, D. Schaefer, J. Aronson, R. Langer, V.P. Shastri, In vivo engineering of organs: The bone bioreactor, PNAS. 102 (2005) 11450–11455. https://doi.org/10.1073/pnas.0504705102.
[108] G. Vunjak-Novakovic, I. Martin, B. Obradovic, S. Treppo, A.J. Grodzinsky, R. Langer, L.E. Freed, Bioreactor cultivation conditions modulate the composition and mechanical properties of tissue-engineered cartilage, Journal of Orthopaedic Research. 17 (1999) 130–138. https://doi.org/10.1002/jor.1100170119.

[109] M. Fröhlich, W.L. Grayson, D. Marolt, J.M. Gimble, N. Kregar-Velikonja, G. Vunjak-Novakovic, Bone Grafts Engineered from Human Adipose-Derived Stem Cells in Perfusion Bioreactor Culture, Tissue Eng Part A. 16 (2010) 179–189. https://doi.org/10.1089/ten.tea.2009.0164.
[110] S.J. Hollister, C.Y. Lin, E. Saito, C.Y. Lin, R.D. Schek, J.M. Taboas, J.M. Williams, B. Partee, C.L. Flanagan, A. Diggs, E.N. Wilke, G.V. Lenthe, R. Müller, T. Wirtz, S. Das, S.E. Feinberg, P.H. Krebsbach, Engineering craniofacial scaffolds, Orthodontics & Craniofacial Research. 8 (2005) 162–173. https://doi.org/10.1111/j.1601-6343.2005.00329.x.
[111] N.S. Karp, J.G. McCarthy, J.S. Schreiber, H.A. Sissons, C.H. Thorne, Membranous bone lengthening: a serial histological study, Ann Plast Surg. 29 (1992) 2–7. https://doi.org/10.1097/00000637-199207000-00002.
[112] L. Meinel, R. Fajardo, S. Hofmann, R. Langer, J. Chen, B. Snyder, G. Vunjak-Novakovic, D. Kaplan, Silk implants for the healing of critical size bone defects, Bone. 37 (2005) 688–698. https://doi.org/10.1016/j.bone.2005.06.010.
[113] J.C. Reichert, A. Cipitria, D.R. Epari, S. Saifzadeh, P. Krishnakanth, A. Berner, M.A. Woodruff, H. Schell, M. Mehta, M.A. Schuetz, G.N. Duda, D.W. Hutmacher, A Tissue Engineering Solution for Segmental Defect Regeneration in Load-Bearing Long Bones, Science Translational Medicine. 4 (2012) 141ra93-141ra93. https://doi.org/10.1126/scitranslmed.3003720.
[114] G. Li, J. Yin, J. Gao, T.S. Cheng, N.J. Pavlos, C. Zhang, M.H. Zheng, Subchondral bone in osteoarthritis: insight into risk factors and microstructural changes, Arthritis Res Ther. 15 (2013) 223. https://doi.org/10.1186/ar4405.
[115] D. Chen, J. Shen, W. Zhao, T. Wang, L. Han, J.L. Hamilton, H.-J. Im, Osteoarthritis: toward a comprehensive understanding of pathological mechanism, Bone Research. 5 (2017) 1–13. https://doi.org/10.1038/boneres.2016.44.
[116] R. El, R. Rm, Role of subchondral bone in the initiation and progression of cartilage damage., Clin Orthop Relat Res. (1986) 34–40.
[117] C. Loebel, R.L. Mauck, J.A. Burdick, Local nascent protein deposition and remodelling guide mesenchymal stromal cell mechanosensing and fate in three-dimensional hydrogels, Nature Materials. 18 (2019) 883–891. https://doi.org/10.1038/s41563-019-0307-6.
[118] J. Garvin, J. Qi, M. Maloney, A.J. Banes, Novel System for Engineering Bioartificial Tendons and Application of Mechanical Load, Tissue Engineering. 9 (2003) 967–979. https://doi.org/10.1089/107632703322495619.
[119] K. Ronaldson-Bouchard, S.P. Ma, K. Yeager, T. Chen, L. Song, D. Sirabella, K. Morikawa, D. Teles, M. Yazawa, G. Vunjak-Novakovic, Advanced maturation of human cardiac tissue grown from pluripotent stem cells, Nature. 556 (2018) 239–243. https://doi.org/10.1038/s41586-018-0016-3.
[120] D. Seliktar, R.A. Black, R.P. Vito, R.M. Nerem, Dynamic Mechanical Conditioning of Collagen-Gel Blood Vessel Constructs Induces Remodeling In Vitro, Annals of Biomedical Engineering. 28 (2000) 351–362. https://doi.org/10.1114/1.275.
[121] D.R. Carter, Mechanical loading histories and cortical bone remodeling, Calcif Tissue Int. 36 (1984) S19–S24. https://doi.org/10.1007/BF02406129.

[122] A. Ruscitto, M.M. Morel, C.J. Shawber, G. Reeve, M.K. Lecholop, D. Bonthius, H. Yao, M.C. Embree, Evidence of vasculature and chondrocyte to osteoblast transdifferentiation in craniofacial synovial joints: Implications for osteoarthritis diagnosis and therapy, FASEB J. (2020). https://doi.org/10.1096/fj.201902287R.
[123] K. Legemate, S. Tarafder, Y. Jun, C.H. Lee, Engineering Human TMJ Discs with Protein-Releasing 3D-Printed Scaffolds, J. Dent. Res. 95 (2016) 800–807. https://doi.org/10.1177/0022034516642404.
[124] N. Vapniarsky, L.W. Huwe, B. Arzi, M.K. Houghton, M.E. Wong, J.W. Wilson, D.C. Hatcher, J.C. Hu, K.A. Athanasiou, Tissue engineering toward temporomandibular joint disc regeneration, Science Translational Medicine. 10 (2018). https://doi.org/10.1126/scitranslmed.aaq1802.
[125] C. Kermer, F. Ziya-Ghazvini, P.W. Poeschl, C. Klug, Two stage reconstruction with revascularized grafts after resection of retromolar and oropharyngeal carcinoma, International Journal of Oral and Maxillofacial Surgery. 33 (2004) 554–557. https://doi.org/10.1016/j.ijom.2003.10.022.
[126] D. Rohner, C. Jaquiéry, C. Kunz, P. Bucher, H. Maas, B. Hammer, Maxillofacial Reconstruction with Prefabricated Osseous Free Flaps: A 3-Year Experience with 24 Patients, Plastic and Reconstructive Surgery. 112 (2003) 748–757. https://doi.org/10.1097/01.PRS.0000069709.89719.79.
[127] K. Le Blanc, C. Tammik, K. Rosendahl, E. Zetterberg, O. Ringdén, HLA expression and immunologic propertiesof differentiated and undifferentiated mesenchymal stem cells, Experimental Hematology. 31 (2003) 890–896. https://doi.org/10.1016/S0301-472X(03)00110-3.
[128] W.L. Grayson, S. Bhumiratana, C. Cannizzaro, P.-H.G. Chao, D.P. Lennon, A.I. Caplan, G. Vunjak-Novakovic, Effects of Initial Seeding Density and Fluid Perfusion Rate on Formation of Tissue-Engineered Bone, Tissue Eng Part A. 14 (2008) 1809–1820. https://doi.org/10.1089/ten.tea.2007.0255.
[129] W.L. Grayson, M. Fröhlich, K. Yeager, S. Bhumiratana, M.E. Chan, C. Cannizzaro, L.Q. Wan, X.S. Liu, X.E. Guo, G. Vunjak-Novakovic, Engineering anatomically shaped human bone grafts, PNAS. 107 (2010) 3299–3304. https://doi.org/10.1073/pnas.0905439106.
[130] K.J. Williams, A.A. Picou, S.L. Kish, A.M. Giraldo, R.A. Godke, K.R. Bondioli, Isolation and Characterization of Porcine Adipose Tissue-Derived Adult Stem Cells, CTO. 188 (2008) 251–258. https://doi.org/10.1159/000121431.
[131] S.R. Oungoulian, K.M. Durney, B.K. Jones, C.S. Ahmad, C.T. Hung, G.A. Ateshian, Wear and Damage of Articular Cartilage with Friction Against Orthopaedic Implant Materials, J Biomech. 48 (2015) 1957–1964. https://doi.org/10.1016/j.jbiomech.2015.04.008.
[132] H.J. Motulsky, R.E. Brown, Detecting outliers when fitting data with nonlinear regression – a new method based on robust nonlinear regression and the false discovery rate, BMC Bioinformatics. 7 (2006) 123. https://doi.org/10.1186/1471-2105-7-123.
[133] T. Mizuguchi, N. Matsumoto, Recent progress in genetics of Marfan syndrome and Marfan-associated disorders, J Hum Genet. 52 (2007) 1–12. https://doi.org/10.1007/s10038-006-0078-1.

[134] V. de Araújo Farias, A.B. Carrillo-Gálvez, F. Martín, P. Anderson, TGF-β and mesenchymal stromal cells in regenerative medicine, autoimmunity and cancer, Cytokine & Growth Factor Reviews. 43 (2018) 25–37. https://doi.org/10.1016/j.cytogfr.2018.06.002.
[135] Z. Zi, Z. Feng, D.A. Chapnick, M. Dahl, D. Deng, E. Klipp, A. Moustakas, X. Liu, Quantitative analysis of transient and sustained transforming growth factor-β signaling dynamics, Mol Syst Biol. 7 (2011) 492. https://doi.org/10.1038/msb.2011.22.
[136] J.S. Park, J.S. Chu, A.D. Tsou, R. Diop, Z. Tang, A. Wang, S. Li, The effect of matrix stiffness on the differentiation of mesenchymal stem cells in response to TGF-β, Biomaterials. 32 (2011) 3921–3930. https://doi.org/10.1016/j.biomaterials.2011.02.019.
[137] Z. Yin, J. Guo, T. Wu, X. Chen, L. Xu, S. Lin, Y. Sun, K.-M. Chan, H. Ouyang, G. Li, Stepwise Differentiation of Mesenchymal Stem Cells Augments Tendon-Like Tissue Formation and Defect Repair In Vivo, STEM CELLS Translational Medicine. 5 (2016) 1106–1116. https://doi.org/10.5966/sctm.2015-0215.
[138] S. Lotz, S. Goderie, N. Tokas, S.E. Hirsch, F. Ahmad, B. Corneo, S. Le, A. Banerjee, R.S. Kane, J.H. Stern, S. Temple, C.A. Fasano, Sustained Levels of FGF2 Maintain Undifferentiated Stem Cell Cultures with Biweekly Feeding, PLoS ONE. 8 (2013) e56289. https://doi.org/10.1371/journal.pone.0056289.
[139] Y. Onuma, K. Higuchi, Y. Aiki, Y. Shu, M. Asada, M. Asashima, M. Suzuki, T. Imamura, Y. Ito, A Stable Chimeric Fibroblast Growth Factor (FGF) Can Successfully Replace Basic FGF in Human Pluripotent Stem Cell Culture, PLOS ONE. 10 (2015) e0118931. https://doi.org/10.1371/journal.pone.0118931.
[140] B. Ahmadian Baghbaderani, X. Tian, J. Scotty Cadet, K. Shah, A. Walde, H. Tran, D.P. Kovarcik, D. Clarke, T. Fellner, A Newly Defined and Xeno-Free Culture Medium Supports Every-Other-Day Medium Replacement in the Generation and Long-Term Cultivation of Human Pluripotent Stem Cells, PLoS One. 11 (2016) e0161229. https://doi.org/10.1371/journal.pone.0161229.
[141] L. Li, J.R. Klim, R. Derda, A.H. Courtney, L.L. Kiessling, Spatial control of cell fate using synthetic surfaces to potentiate TGF-β signaling, Proc. Natl. Acad. Sci. U.S.A. 108 (2011) 11745–11750. https://doi.org/10.1073/pnas.1101454108.
[142] L. Lin, L. Liu, B. Zhao, R. Xie, W. Lin, H. Li, Y. Li, M. Shi, Y.-G. Chen, T.A. Springer, X. Chen, Carbon nanotube-assisted optical activation of TGF-β signalling by near-infrared light, Nature Nanotech. 10 (2015) 465–471. https://doi.org/10.1038/nnano.2015.28.
[143] J. Singh, C.E. Chuaqui, P.A. Boriack-Sjodin, W.-C. Lee, T. Pontz, M.J. Corbley, H.-K. Cheung, R.M. Arduini, J.N. Mead, M.N. Newman, J.L. Papadatos, S. Bowes, S. Josiah, L.E. Ling, Successful shape-Based virtual screening: The discovery of a potent inhibitor of the type I TGFβ receptor kinase (TβRI), Bioorganic & Medicinal Chemistry Letters. 13 (2003) 4355–4359. https://doi.org/10.1016/j.bmcl.2003.09.028.
[144] W. Kwiatkowski, P.C. Gray, S. Choe, Engineering TGF-β superfamily ligands for clinical applications, Trends in Pharmacological Sciences. 35 (2014) 648–657. https://doi.org/10.1016/j.tips.2014.10.006.
[145] N.A. Repina, A. Rosenbloom, A. Mukherjee, D.V. Schaffer, R.S. Kane, At Light Speed: Advances in Optogenetic Systems for Regulating Cell Signaling and Behavior, Annual

Review of Chemical and Biomolecular Engineering. 8 (2017) 13–39. https://doi.org/10.1146/annurev-chembioeng-060816-101254.
[146] N.A. Repina, T. McClave, H.J. Johnson, X. Bao, R.S. Kane, D.V. Schaffer, Engineered Illumination Devices for Optogenetic Control of Cellular Signaling Dynamics, Cell Reports. 31 (2020) 107737. https://doi.org/10.1016/j.celrep.2020.107737.
[147] I.Y. Choi, H. Lim, A. Huynh, J. Schofield, H.J. Cho, H. Lee, P. Andersen, J.H. Shin, W.D. Heo, S.-H. Hyun, Y.J. Kim, Y. Oh, H. Kim, G. Lee, Novel culture system via wirelessly controllable optical stimulation of the FGF signaling pathway for human and pig pluripotency, Biomaterials. 269 (2021) 120222. https://doi.org/10.1016/j.biomaterials.2020.120222.
[148] P.A. Humphreys, S. Woods, C.A. Smith, N. Bates, S.A. Cain, R. Lucas, S.J. Kimber, Optogenetic Control of the BMP Signaling Pathway, ACS Synth. Biol. (2020). https://doi.org/10.1021/acssynbio.0c00315.
[149] N.A. Repina, X. Bao, J.A. Zimmermann, D.A. Joy, R.S. Kane, D.V. Schaffer, Optogenetic control of Wnt signaling for modeling early embryogenic patterning with human pluripotent stem cells, Bioengineering, 2019. https://doi.org/10.1101/665695.
[150] K.A. Harradine, R.J. Akhurst, Mutations of TGFß signaling molecules in human disease, Annals of Medicine. 38 (2006) 403–414. https://doi.org/10.1080/07853890600919911.
[151] X. Xia, Y. Zhang, C.R. Zieth, S.-C. Zhang, Transgenes Delivered by Lentiviral Vector Are Suppressed in Human Embryonic Stem Cells in a Promoter-Dependent Manner, (2010) 16.
[152] E.S. Jeon, H.J. Moon, M.J. Lee, H.Y. Song, Y.M. Kim, Y.C. Bae, J.S. Jung, J.H. Kim, Sphingosylphosphorylcholine induces differentiation of human mesenchymal stem cells into smooth-muscle-like cells through a TGF-β-dependent mechanism, Journal of Cell Science. 119 (2006) 4994–5005. https://doi.org/10.1242/jcs.03281.
[153] L.J. Bugaj, W.A. Lim, High-throughput multicolor optogenetics in microwell plates, Nat Protoc. 14 (2019) 2205–2228. https://doi.org/10.1038/s41596-019-0178-y.
[154] H. Liu, C. Zhang, S. Zhu, P. Lu, T. Zhu, X. Gong, Z. Zhang, J. Hu, Z. Yin, B.C. Heng, X. Chen, H. Wei Ouyang, Mohawk Promotes the Tenogenesis of Mesenchymal Stem Cells Through Activation of the TGFβ Signaling Pathway, Stem Cells. 33 (2015) 443–455. https://doi.org/10.1002/stem.1866.
[155] C.K. Kuo, R.S. Tuan, Mechanoactive Tenogenic Differentiation of Human Mesenchymal Stem Cells, Tissue Engineering Part A. 14 (2008) 1615–1627. https://doi.org/10.1089/ten.tea.2006.0415.
[156] B. Bakhshandeh, M. Soleimani, S.H. Paylakhi, N. Ghaemi, A microRNA signature associated with chondrogenic lineage commitment, J Genet. 91 (2012) 171–182. https://doi.org/10.1007/s12041-012-0168-0.
[157] A. Haseeb, R. Kc, M. Angelozzi, C. de Charleroy, D. Rux, R.J. Tower, L. Yao, R.P. da Silva, M. Pacifici, L. Qin, V. Lefebvre, SOX9 keeps growth plates and articular cartilage healthy by inhibiting chondrocyte dedifferentiation/osteoblastic redifferentiation, PNAS. 118 (2021). https://doi.org/10.1073/pnas.2019152118.

[158] M. Girardot, E. Bayet, J. Maurin, P. Fort, P. Roux, P. Raynaud, SOX9 has distinct regulatory roles in alternative splicing and transcription, Nucleic Acids Res. 46 (2018) 9106–9118. https://doi.org/10.1093/nar/gky553.
[159] B.M. Clancy, J.D. Johnson, A.-J. Lambert, S. Rezvankhah, A. Wong, C. Resmini, J.L. Feldman, S. Leppanen, D.D. Pittman, A gene expression profile for endochondral bone formation: oligonucleotide microarrays establish novel connections between known genes and BMP-2-induced bone formation in mouse quadriceps, Bone. 33 (2003) 46–63. https://doi.org/10.1016/S8756-3282(03)00116-9.
[160] L.J. Bugaj, A.J. Sabnis, A. Mitchell, J.E. Garbarino, J.E. Toettcher, T.G. Bivona, W.A. Lim, Cancer mutations and targeted drugs can disrupt dynamic signal encoding by the Ras-Erk pathway, Science. 361 (2018). https://doi.org/10.1126/science.aao3048.
[161] A.B. Rosenbloom, M. Tarczyński, N. Lam, R.S. Kane, L.J. Bugaj, D.V. Schaffer, β-Catenin signaling dynamics regulate cell fate in differentiating neural stem cells, PNAS. (2020). https://doi.org/10.1073/pnas.2008509117.
[162] P.B. Hellwarth, Y. Chang, A. Das, P.-Y. Liang, X. Lian, N.A. Repina, X. Bao, Optogenetic-mediated cardiovascular differentiation and patterning of human pluripotent stem cells, Advanced Genetics. 2 (2021) e202100011. https://doi.org/10.1002/ggn2.202100011.
[163] O.F. Vila, M. Chavez, S.P. Ma, K. Yeager, L.V. Zholudeva, J.M. Colón-Mercado, Y. Qu, T.R. Nash, C. Lai, C.M. Feliciano, M. Carter, R.D. Kamm, L.M. Judge, B.R. Conklin, M.E. Ward, T.C. McDevitt, G. Vunjak-Novakovic, Bioengineered optogenetic model of human neuromuscular junction, Biomaterials. 276 (2021) 121033. https://doi.org/10.1016/j.biomaterials.2021.121033.
[164] C.J. Chua, J.L. Han, W. Li, W. Liu, E. Entcheva, Integration of Engineered "Spark-Cell" Spheroids for Optical Pacing of Cardiac Tissue, Frontiers in Bioengineering and Biotechnology. 9 (2021). https://www.frontiersin.org/article/10.3389/fbioe.2021.658594 (accessed January 18, 2022).
[165] M. Rieger, C. Dellenbach, J. vom Berg, J. Beil-Wagner, A. Maguy, S. Rohr, Enabling comprehensive optogenetic studies of mouse hearts by simultaneous opto-electrical panoramic mapping and stimulation, Nat Commun. 12 (2021) 5804. https://doi.org/10.1038/s41467-021-26039-8.
[166] P. Rao, P. Rao, P. Rao, P. Rao, L. Wang, L. Wang, L. Wang, L. Wang, Y. Cheng, Y. Cheng, Y. Cheng, X. Wang, X. Wang, X. Wang, X. Wang, X. Wang, H. Li, G. Zheng, G. Zheng, G. Zheng, Z. Li, C. Jiang, C. Jiang, C. Jiang, Q. Zhou, Q. Zhou, Q. Zhou, C. Huang, C. Huang, C. Huang, Near-infrared light driven tissue-penetrating cardiac optogenetics via upconversion nanoparticles in vivo, Biomed. Opt. Express, BOE. 11 (2020) 1401–1416. https://doi.org/10.1364/BOE.381480.
[167] X. Wu, Y. Zhang, K. Takle, O. Bilsel, Z. Li, H. Lee, Z. Zhang, D. Li, W. Fan, C. Duan, E.M. Chan, C. Lois, Y. Xiang, G. Han, Dye-Sensitized Core/Active Shell Upconversion Nanoparticles for Optogenetics and Bioimaging Applications, ACS Nano. 10 (2016) 1060–1066. https://doi.org/10.1021/acsnano.5b06383.
[168] K. Yadav, A.-C. Chou, R.K. Ulaganathan, H.-D. Gao, H.-M. Lee, C.-Y. Pan, Y.-T. Chen, Targeted and efficient activation of channelrhodopsins expressed in living cells via

specifically-bound upconversion nanoparticles, Nanoscale. 9 (2017) 9457–9466. https://doi.org/10.1039/C7NR03246C.
[169] N. Yu, L. Huang, Y. Zhou, T. Xue, Z. Chen, G. Han, Near-Infrared-Light Activatable Nanoparticles for Deep-Tissue-Penetrating Wireless Optogenetics, Advanced Healthcare Materials. 8 (2019) 1801132. https://doi.org/10.1002/adhm.201801132.
[170] M. Hörner, C. Jerez-Longres, A. Hudek, S. Hook, O.S. Yousefi, W.W.A. Schamel, C. Hörner, M.D. Zurbriggen, H. Ye, H.J. Wagner, W. Weber, Spatiotemporally confined red light-controlled gene delivery at single-cell resolution using adeno-associated viral vectors, Science Advances. 7 (n.d.) eabf0797. https://doi.org/10.1126/sciadv.abf0797.
[171] Y. Zhou, D. Kong, X. Wang, G. Yu, X. Wu, N. Guan, W. Weber, H. Ye, A small and highly sensitive red/far-red optogenetic switch for applications in mammals, Nat Biotechnol. 40 (2022) 262–272. https://doi.org/10.1038/s41587-021-01036-w.
[172] T.A. Redchuk, E.S. Omelina, K.G. Chernov, V.V. Verkhusha, Near-infrared optogenetic pair for protein regulation and spectral multiplexing, Nat Chem Biol. 13 (2017) 633–639. https://doi.org/10.1038/nchembio.2343.
[173] T.A. Redchuk, A.A. Kaberniuk, V.V. Verkhusha, Near-infrared light–controlled systems for gene transcription regulation, protein targeting and spectral multiplexing, Nat Protoc. 13 (2018) 1121–1136. https://doi.org/10.1038/nprot.2018.022.
[174] T.A. Redchuk, M.M. Karasev, E.S. Omelina, V.V. Verkhusha, Near-Infrared Light-Controlled Gene Expression and Protein Targeting in Neurons and Non-neuronal Cells, ChemBioChem. 19 (2018) 1334–1340. https://doi.org/10.1002/cbic.201700642.
[175] D.S. Svoboda, M.I. Barrasa, J. Shu, R. Rietjens, S. Zhang, M. Mitalipova, P. Berube, D. Fu, L.D. Shultz, G.W. Bell, R. Jaenisch, Human iPSC-derived microglia assume a primary microglia-like state after transplantation into the neonatal mouse brain, Proceedings of the National Academy of Sciences. 116 (2019) 25293–25303. https://doi.org/10.1073/pnas.1913541116.
[176] B.J. Pavlovic, L.E. Blake, J. Roux, C. Chavarria, Y. Gilad, A Comparative Assessment of Human and Chimpanzee iPSC-derived Cardiomyocytes with Primary Heart Tissues, Sci Rep. 8 (2018) 15312. https://doi.org/10.1038/s41598-018-33478-9.
[177] J.-A. Sahel, E. Boulanger-Scemama, C. Pagot, A. Arleo, F. Galluppi, J.N. Martel, S.D. Esposti, A. Delaux, J.-B. de Saint Aubert, C. de Montleau, E. Gutman, I. Audo, J. Duebel, S. Picaud, D. Dalkara, L. Blouin, M. Taiel, B. Roska, Partial recovery of visual function in a blind patient after optogenetic therapy, Nat Med. 27 (2021) 1223–1229. https://doi.org/10.1038/s41591-021-01351-4.
[178] A. Bansal, S. Shikha, Y. Zhang, Towards translational optogenetics, Nat Biomed Eng. (2022) 1–21. https://doi.org/10.1038/s41551-021-00829-3.
[179] U. Doehn, C. Hauge, S.R. Frank, C.J. Jensen, K. Duda, J.V. Nielsen, M.S. Cohen, J.V. Johansen, B.R. Winther, L.R. Lund, O. Winther, J. Taunton, S.H. Hansen, M. Frödin, RSK Is a Principal Effector of the RAS-ERK Pathway for Eliciting a Coordinate Promotile/Invasive Gene Program and Phenotype in Epithelial Cells, Molecular Cell. 35 (2009) 511–522. https://doi.org/10.1016/j.molcel.2009.08.002.
[180] O.S. Thomas, M. Hörner, W. Weber, A graphical user interface to design high-throughput optogenetic experiments with the optoPlate-96, Nat Protoc. 15 (2020) 2785–2787. https://doi.org/10.1038/s41596-020-0349-x.

[181] F. Meier, A.-D. Brunner, M. Frank, A. Ha, I. Bludau, E. Voytik, S. Kaspar-Schoenefeld, M. Lubeck, O. Raether, N. Bache, R. Aebersold, B.C. Collins, H.L. Röst, M. Mann, diaPASEF: parallel accumulation-serial fragmentation combined with data-independent acquisition, Nat Methods. 17 (2020) 1229–1236. https://doi.org/10.1038/s41592-020-00998-0.
[182] N.A. Kulak, G. Pichler, I. Paron, N. Nagaraj, M. Mann, Minimal, encapsulated proteomic-sample processing applied to copy-number estimation in eukaryotic cells, Nat Methods. 11 (2014) 319–324. https://doi.org/10.1038/nmeth.2834.
[183] J. Adachi, K. Hashiguchi, M. Nagano, M. Sato, A. Sato, K. Fukamizu, Y. Ishihama, T. Tomonaga, Improved Proteome and Phosphoproteome Analysis on a Cation Exchanger by a Combined Acid and Salt Gradient, Anal Chem. 88 (2016) 7899–7903. https://doi.org/10.1021/acs.analchem.6b01232.
[184] R. Bruderer, O.M. Bernhardt, T. Gandhi, S.M. Miladinović, L.-Y. Cheng, S. Messner, T. Ehrenberger, V. Zanotelli, Y. Butscheid, C. Escher, O. Vitek, O. Rinner, L. Reiter, Extending the limits of quantitative proteome profiling with data-independent acquisition and application to acetaminophen-treated three-dimensional liver microtissues, Mol Cell Proteomics. 14 (2015) 1400–1410. https://doi.org/10.1074/mcp.M114.044305.
[185] T.J. Klein, B.L. Schumacher, T.A. Schmidt, K.W. Li, M.S. Voegtline, K. Masuda, E.J.-M.A. Thonar, R.L. Sah, Tissue engineering of stratified articular cartilage from chondrocyte subpopulations, Osteoarthritis and Cartilage. 11 (2003) 595–602. https://doi.org/10.1016/S1063-4584(03)00090-6.
[186] T.-K. Kim, B. Sharma, C.G. Williams, M.A. Ruffner, A. Malik, E.G. McFarland, J.H. Elisseeff, Experimental Model for Cartilage Tissue Engineering to Regenerate the Zonal Organization of Articular Cartilage, Osteoarthritis and Cartilage. 11 (2003) 653–664. https://doi.org/10.1016/S1063-4584(03)00120-1.
[187] K.W. Ng, C.C.-B. Wang, R.L. Mauck, T.-A.N. Kelly, N.O. Chahine, K.D. Costa, G.A. Ateshian, C.T. Hung, A layered agarose approach to fabricate depth-dependent inhomogeneity in chondrocyte-seeded constructs, Journal of Orthopaedic Research. 23 (2005) 134–141. https://doi.org/10.1016/j.orthres.2004.05.015.
[188] H.M. Zlotnick, A.T. Clark, S.E. Gullbrand, J.L. Carey, X.M. Cheng, R.L. Mauck, Magneto-Driven Gradients of Diamagnetic Objects for Engineering Complex Tissues, Advanced Materials. 32 (2020) 2005030. https://doi.org/10.1002/adma.202005030.
[189] D. Chen, J.Y. Wu, K.M. Kennedy, K. Yeager, J.C. Bernhard, J.J. Ng, B.K. Zimmerman, S. Robinson, K.M. Durney, C. Shaeffer, O.F. Vila, C. Takawira, J.M. Gimble, X.E. Guo, G.A. Ateshian, M.J. Lopez, S.B. Eisig, G. Vunjak-Novakovic, Tissue engineered autologous cartilage-bone grafts for temporomandibular joint regeneration, Science Translational Medicine. 12 (2020). https://doi.org/10.1126/scitranslmed.abb6683.
[190] M. Lilledahl, M. Olderøy, A. Finnøy, K. Olstad, J.E. Brinchman, Second harmonic generation imaging in tissue engineering and cartilage pathologies, in: Multiphoton Microscopy in the Biomedical Sciences XV, SPIE, 2015: pp. 145–150. https://doi.org/10.1117/12.2081583.
[191] M.A. Skylar-Scott, S.G.M. Uzel, L.L. Nam, J.H. Ahrens, R.L. Truby, S. Damaraju, J.A. Lewis, Biomanufacturing of organ-specific tissues with high cellular density and embedded

vascular channels, Sci Adv. 5 (2019) eaaw2459. https://doi.org/10.1126/sciadv.aaw2459.
[192] A. Dufour, X.B. Gallostra, C. O'Keeffe, K. Eichholz, S. Von Euw, O. Garcia, D.J. Kelly, Integrating melt electrowriting and inkjet bioprinting for engineering structurally organized articular cartilage, Biomaterials. 283 (2022) 121405. https://doi.org/10.1016/j.biomaterials.2022.121405.
[193] L. Pferdehirt, A.R. Damato, M. Dudek, Q.-J. Meng, E.D. Herzog, F. Guilak, Synthetic gene circuits for preventing disruption of the circadian clock due to interleukin-1–induced inflammation, Science Advances. 8 (2022) eabj8892. https://doi.org/10.1126/sciadv.abj8892.
[194] H. Robson, T. Siebler, D.A. Stevens, S.M. Shalet, G.R. Williams, Thyroid Hormone Acts Directly on Growth Plate Chondrocytes to Promote Hypertrophic Differentiation and Inhibit Clonal Expansion and Cell Proliferation*, Endocrinology. 141 (2000) 3887–3897. https://doi.org/10.1210/endo.141.10.7733.
[195] J.C. Fernandes, J. Martel-Pelletier, J.-P. Pelletier, The role of cytokines in osteoarthritis pathophysiology, Biorheology. 39 (2002) 237–246.
[196] K.H. Collins, K.L. Lenz, E.N. Pollitt, D. Ferguson, I. Hutson, L.E. Springer, A.K. Oestreich, R. Tang, Y.-R. Choi, G.A. Meyer, S.L. Teitelbaum, C.T. Pham, C.A. Harris, F. Guilak, Fat implantation in lipodystrophic mice restores susceptibility to joint injury and osteoarthritis independent of body weight, Osteoarthritis and Cartilage. 29 (2021) S14–S15. https://doi.org/10.1016/j.joca.2021.02.034.
[197] J.H. Jung, C.H. Bang, G.G. Song, C. Kim, J.-H. Kim, S.J. Choi, Knee osteoarthritis and menopausal hormone therapy in postmenopausal women: a nationwide cross-sectional study, Menopause. 26 (2019) 598–602. https://doi.org/10.1097/GME.0000000000001280.
[198] D.A. Nichols, I.S. Sondh, S.R. Litte, P. Zunino, R. Gottardi, Design and validation of an osteochondral bioreactor for the screening of treatments for osteoarthritis, Biomed Microdevices. 20 (2018) 18. https://doi.org/10.1007/s10544-018-0264-x.
[199] Z. Li, Z. Lin, S. Liu, H. Yagi, X. Zhang, L. Yocum, M. Romero-Lopez, C. Rhee, M.J. Makarcyzk, I. Yu, E.N. Li, M.R. Fritch, Q. Gao, K.B. Goh, B. O'Donnell, T. Hao, P.G. Alexander, B. Mahadik, J.P. Fisher, S.B. Goodman, B.A. Bunnell, R.S. Tuan, H. Lin, Human Mesenchymal Stem Cell-Derived Miniature Joint System for Disease Modeling and Drug Testing, Advanced Science. n/a (2022) 2105909. https://doi.org/10.1002/advs.202105909.
[200] P. Occhetta, A. Mainardi, E. Votta, Q. Vallmajo-Martin, M. Ehrbar, I. Martin, A. Barbero, M. Rasponi, Hyperphysiological compression of articular cartilage induces an osteoarthritic phenotype in a cartilage-on-a-chip model, Nat Biomed Eng. 3 (2019) 545–557. https://doi.org/10.1038/s41551-019-0406-3.